Master thesis

A new flexible triangular finite element for geotechnical problems

BM3-1
Aalborg University Esbjerg
2012

Title sheet

Topic:	Master Thesis
Title:	A new flexible triangular finite element for geotechnical problems
Periode:	2012/01/02 - 2012/14/06
Supervisors:	Lars Damkilde
	Ronnie Refstrup Pedersen
Number of pages:	80

Abstract

This work deals with the formulation and testing of a new flexible triangular element. The formulation of the element is based on the quadratic-strain triangular element, which is a 10-node element with 20 d.o.f. The new element is obtained by replacing the 2 nodes and their translational d.o.f. on the sides with 1 midside node with both translational and rotational d.o.f. Furthermore, it is reduced from 20 to 12 global d.o.f. using static condensation. The static condensation allows the element to be incompatible in the rotational d.o.f.

A new flexible element would be useful e.g in analysis of geotechnical problems, in which the bearing capacity of the soil is often overestimated. This is indicated by analysis of two common geotechnical problems performed with meshes of 6-node and 15-node elements. It turns out that the 15-node element, which is more flexible, provides better accuracy compared to the 6-node element. If the advantages of the accuracy of a flexible element can be combined with the low computational costs of the 6-node element, the procedure of geotechnical problems can be improved a great deal.

The element is implemented in a nonlinear elastic-plastic finite element program, computed in Matlab. Both linear and nonlinear tests of the element is performed. The results for the linear tests shows that the element provides reasonable results when the mesh is refined sufficiently. For a coarse mesh, the element does not provide good results due to the incompatibility.

Von Mises yield criteria is implemented in the finite element program in order to perform nonlinear tests of the element. The tests indicates that the element is not working properly in a nonlinear application. This is due to the condensed d.o.f. which effects the global solution.

Finally, several tests of the non-condensed element is done in order to demonstrate how the condensed element is supposed to perform in geotechnical problems. Mohr-Coulomb's yield criteria is implemented for these tests, which are tests of the bearing capacity of a strip footing on a soil layer. The non-condensed element provides better results than a the linear-strain triangle element. Furthermore, it does not overestimate the bearing capacity of the strip footing for most of the cases considered.

Preface

This master thesis 'A new flexible triangular finite element for geotechnical problems' has been carried out in the period 2012/01/02 - 2012/14/06 on Esbjerg Institute of Technology, Aalborg University.

First of all, we wish to thank our supervisors, professor Lars Damkilde and associate professor Refstrup Pedersen, for their support and involvement in the master thesis.

Secondly, we wish to thank Nikolaj Westergaard for his computer expertise and for installations of severs for matlab computations. We are also grateful to Michael Jepsen for encouraging and inspiring us.

Reading guides

The thesis consists of a main report, an appendix report and Matlab programs. The main report is printed together with the appendix report. In addition the main report, appendix report, the annexes and the programs are enclosed on a CD.

Literary references are referred to directly in the main repport, and a list of references can be found in the end of the main report. The references are noted by [nr.]. In the bibliography, some of the references is marked by [Annex]. These pdf's are enclosed as annexes on the CD.

Authors

Annamarie Søllingvraa Larsen

Line Stenstad

Contents

1 Introduction **1**
- 1.1 Geotechnical problems . . . 2
- 1.2 Scope of work . . . 7

2 Formulation of the extended triangular element **8**
- 2.1 Condensation of element vectors and matrices . . . 10
- 2.2 Interpolation functions . . . 12
- 2.3 Nodal loads . . . 14

3 Linear tests of the extended element **18**
- 3.1 Patch and stability tests . . . 18
- 3.2 Cook's membrane test . . . 18
- 3.3 Plate with hole . . . 22
- 3.4 Conclusion . . . 26

4 Nonlinear Finite Element Program **27**
- 4.1 Incremental iteration procedure . . . 27
- 4.2 Determining the plastic contributions . . . 30
- 4.3 Returning to the yield surface . . . 31
- 4.4 Updating the stiffness matrix . . . 32

5 Von Mises yield criteria **34**

6 Tests with von Mises yield criteria **35**
- 6.1 Plane stress . . . 35
- 6.2 Plane strain . . . 41
- 6.3 Strip footing with von Mises yield criteria . . . 46
- 6.4 Conclusion on tests with von Mises yield criteria . . . 50

7 Condensation of non-yielding elements **52**
- 7.1 Patch test . . . 52

8 Mohr-Coulomb yield criteria **56**
- 8.1 Implementation of the Mohr-Coulomb criteria . . . 56
- 8.2 Return mapping for the Morh-Coulomb criteria . . . 58

9 Bearing capacity of a strip footing on a Mohr-Coulomb material **63**
- 9.1 Analytical solution . . . 63

9.2 Finite element analyses 63
9.3 Conclusion on tests of a strip footing with Mohr-Coulomb's criteria 73

10 Discussion **74**

11 Conclusion **77**

Bibliography **79**

A Geotechnical problems **81**
A.1 Slope stability analysis 81
A.2 Bearing capacity of a strip footing 88

B Computation of the stiffness matrix **96**

C Linear tests of the extended element **98**
C.1 Patch test 98
C.2 Stability 100
C.3 Cook's membrane test 102
C.4 Plat with a hole 107
C.5 Convergence of strain energy 112
C.6 Conclusion on linear tests 114

D Introducing a hardening parameter - Figures **116**
D.1 Mesh 116
D.2 Bearing capacity 116

1 Introduction

Over the past decades, the finite element method has been the most common numerical method used within various fields of engineering problems. The finite element method is particularly widespread because it is very general and is capable of describing any material strain-stress relations. Furthermore, it is capable of handling both geometric and material nonlinearities, which are often important in geotechnical problems, such as soil mechanics and soil-structure interaction problems. This is due to the fact that the behaviour of soil materials is highly nonlinear, even at very small strains [24]. However, it turns out that problems with convergence in analysis of even simple geotechnical problems may arise [14].

A large amount of research has been carried out on the improvement of finite elements, and yet more effective elements regarding the number of d.o.f. are still needed for solving the convergence problems mentioned above. The purpose of this paper is to test whether a new triangular finite element is more effective when dealing with nonlinearities, compared to the standard triangular elements used today.

The conventional finite elements used are the triangular elements, due to the topological advantages compared to rectangular elements. However, when the simple 3-node triangular element is used in coarse meshes the convergence may not be optimal, primarily due to the shear locking effect. The locking effect refers to the increased shear stiffness in the mesh in connection with loading. Thus, the locking effect may preclude reasonable accuracy [11]. Therefore, higher-order triangular elements are preferable, e.g. 6-node and 15-node elements.

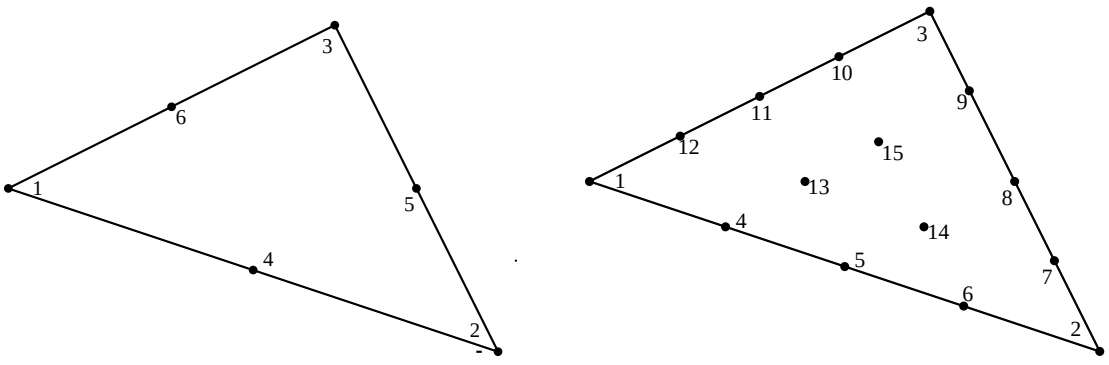

Figure 1.1: The 6-node triangular element and the 15-node triangular element.

The geotechnical software Plaxis contains both 6-node and 15-node elements. In the following some common geotechnical problems are analysed in Plaxis in order to compare the performance of the 6-node and 15-node elements. The comparison between the elements is performed with the purpose of demonstrating the importance of the number of d.o.f. in connection with the formulation of a new effective triangular element.

1.1 Geotechnical problems

One of the geotechnical problems considered is the stability of a simple slope model consisting of one soil layer. Another geotechnical problem considered is the bearing capacity of a strip footing on a soil layer. Common to these problems are that they can be assessed by analytical solutions. Thus, the finite element results from Plaxis can be compared with the results obtained by analytical calculations.

1.1.1 Slope stability analysis

The stability analysis of a slope model is carried out in Appendix A.1. The slope is 20 m wide and 10 m high, and on the top of the slope an external load of 50 kN/m is applied, see Figure 1.2. Furthermore, the slope itself is composed of a clay material.

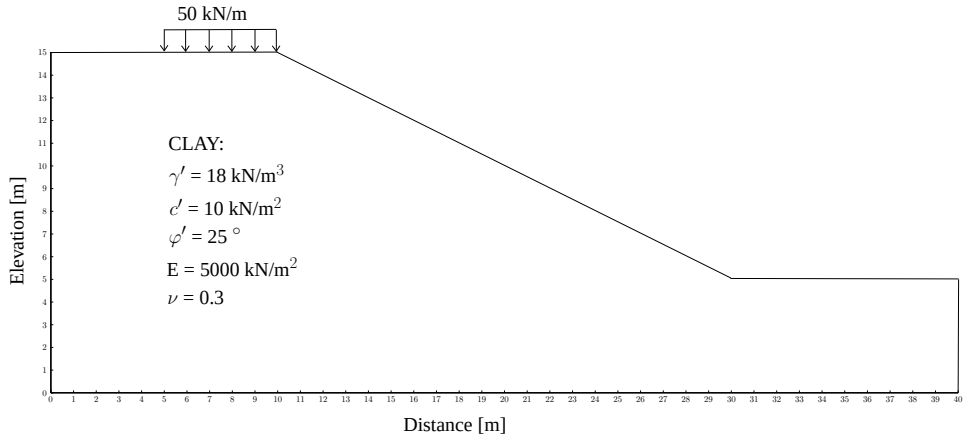

Figure 1.2: Slope model with an external load of 50 kN/m.

The stability analysis of the slope model is first carried out by analytical calculations as shown in Appendix A.1. Subsequently, the finite element analysis of the stability is carried out for the slope model using the program Plaxis. A plane strain model of the slope is defined in Plaxis by a mesh of 6-node elements and 15-node elements, respectively.

The factor of safety and the critical slip surface obtained with a mesh of 15-node elements is given in Figure 1.3, where the critical slip surface is indicated with a contour plot of the total displacements.

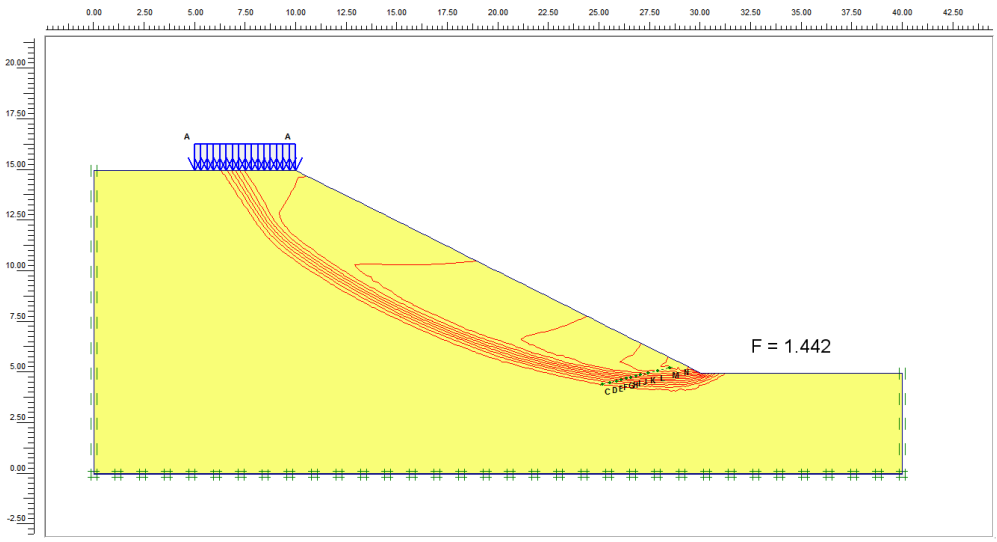

Figure 1.3: Deformed mesh with 6-node elements (deformations are scaled $500*10^{-6}$).

It is shown in Figure 1.4 that the 6-node elements provides a slower convergence rate than the 15-node elements. Convergence is not fully obtained before 29309 elements and 118312 d.o.f., whereas convergence is attained by only 1556 elements and 25378 d.o.f. with the mesh of 15-node elements. Thus, it requires a significantly higher computing costs to achieve convergence with 6-node elements as compared to 15-node elements.

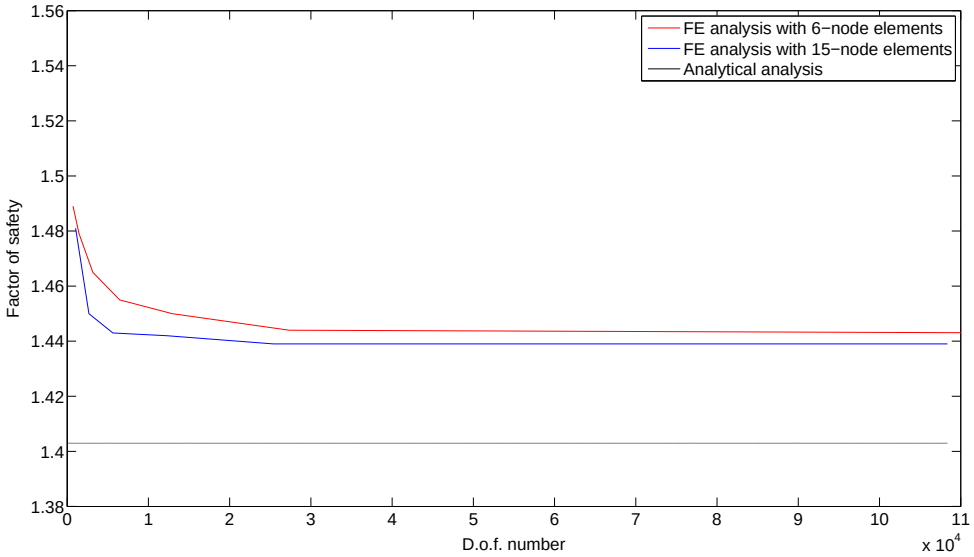

Figure 1.4: Convergence rate for FE and LE analyses.

Compared to the factor of safety obtained from the software Slope/w, as shown in Figure 1.4, the factor is overestimated when using a coarse mesh of 6-node elements, where as the factor is more accurately estimated when using a coarse mesh of 15-node elements. Thus, a mesh of 15-node elements provides reasonable accuracy even for coarse meshes.

Further studies of the convergence and accuracy in analysis with 6-node and 15-node elements is necessary, to validate the benefits of the 15-node elements.

1.1.2 Bearing capacity of a strip footing

The calculations of the bearing capacity for a strip footing is carried out in Appendix A.2. The purpose is to show that the results from a mesh of 15-node elements provides a better convergence toward the exact value of the bearing capacity compared to the result from a mesh of 6-node elements. The considered strip footing placed on the top of a soil layer is shown in Figure 1.5.

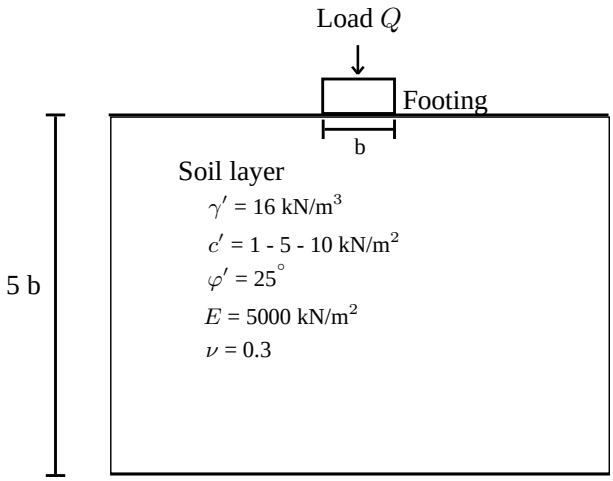

Figure 1.5: Geometry and material property of the strip footing.

In Appendix A.2, the exact value of the bearing capacity for the strip footing is calculated with different values of the cohesion. Subsequently, the calculations of the bearing capacity of the footing is carried out in Plaxis. In the calculations the settlement of the footing is simulated by a uniform displacement at the top of the soil layer instead of modelling the footing itself. This approach lead to a very simple model of the soil domain. As the soil domain is axisymmetric only half of the soil domain is modelled. The width and hight of the soil domain is 5 x 5 m. The considered domain with the given boundary conditions is shown in Figure 1.6.a.

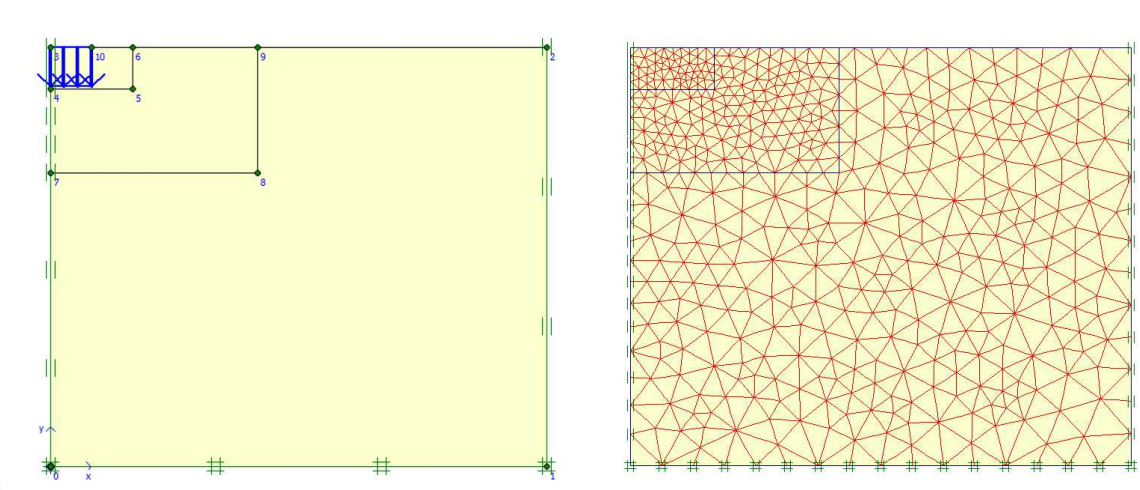

Figure 1.6: (a) The considered soil domain with boundary conditions, (b) Example of a mesh with 7905 elements and 3671 d.o.f.

The soil domain is modelled with both 6-node and 15-node elements and a forced displacement of $u = 0.5 - 1$ m is applied to the nodes located at the footing area. An example of the element mesh is seen in Figure 1.6.b.

The bearing capacity for the footing is given by the load-displacement curves computed in Plaxis with meshes of 6-noded and 15-node elements, see Appendix A.2. In Figure 1.7 the convergence of the bearing capacity is shown for a cohesion of 10 kN/m^2, and it appears that the 6-node elements provides a significantly slower convergence rate than the 15-node elements.

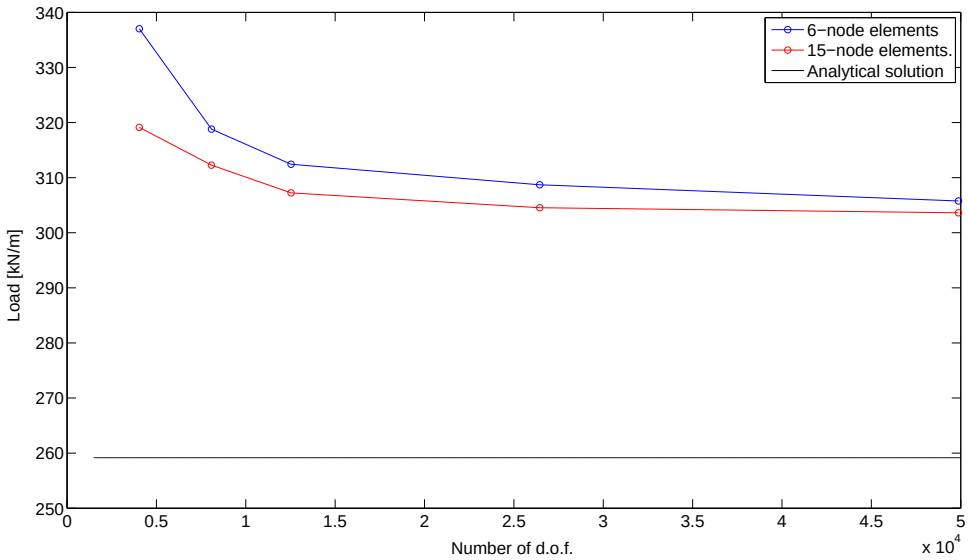

Figure 1.7: The convergence of the bearing capacity for a cohesion of 10 kN/m^2.

For both 6- and 15-node element it is seen that the bearing capacity is overestimated when comparing with the analytical solution. The bearing capacity is overestimated the most when using a coarse mesh of 6-node elements, whereas the bearing capacity is more accurately estimated when using a coarse mesh of 15-node elements. Thus, a mesh of 15-node elements provides reasonable accuracy even for coarse meshes. This validates the previous results in Section 1.1.1.

It is clear that the combination of fewer equilibrium equations, as the 6-node element provides, and the accuracy and flexibility of the 15-node element is preferable to the common elements used today. However, even with the 15-node element the bearing capacity is still overestimated.

A way to not overestimate the bearing capacity could be to use incompatible elements. An incompatible element allows a d.o.f. of an element to not conform to the corresponding d.o.f. of the adjacent element, see Figure 1.8.

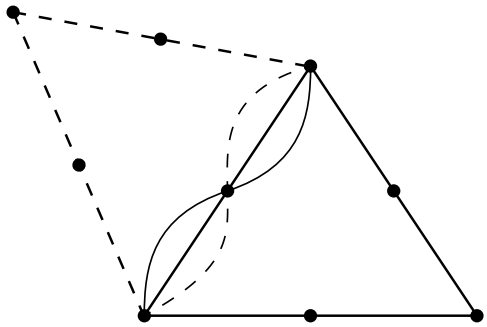

Figure 1.8: Internal incompatibility within elements.

The incompatible elements are known to be overly flexible for coarse meshes. But for a sufficiently refined mesh, the error caused by the incompatability becomes insignificant. Furthermore, these elements converges "from the opposite side" than compatible elements, i.e. an incompatible element would converge from below and towards the analytical value of the bearing capacity. This means that the incompatible elements probably will not overestimate the bearing capacity, and therefore be on the safe side.

This leads to the scope of the thesis.

1.2 Scope of work

The geotechnical software Plaxis contains the triangular 15-node element, which provides a higher accuracy compared to the standard triangular 6-node element. It has been shown that the accuracy of the 15-node element is preferable even though there is a significantly larger computational effort to solve the problems due to the extra degrees of freedom (d.o.f.).

If the advantages of the accuracy and flexibility of higher-order elements can be combined with the low computational costs of the standard 6-node element, the numerical procedure of geotechnical problems can be improved a great deal. This leads to the aim of this work:

> *Formulate a new extended triangular plane element with a high convergence rate and low computational costs.*

In Figure 1.7 it has been shown that both the 6-node and the 15-node elements overestimates the stability of a slope and overestimates the bearing capacity for at strip footing as well, which is a common geotechnical problems.

The purpose of the new extended element is to improve the finite element analyses of geotechnical problems. It has been shown that finite element analyses performed with both 6-node and the 15-node elements leads to an overestimation of the stability of a slope and an overestimation of the bearing capacity of a strip footing as well.

It is known that incompatible elements converges “from below" as opposed to “from above" which the 6-node and 15-node elements do. This imply that incompatible elements may not overestimate the bearing capacity. This feature is taken in to account in the formulation of the new extended element.

The new element is implemented in a Matlab program for solving both linear elastic problems as well as nonlinear elastic-plastic problems. First it is verified that the implementation of the element in the program, is correct. This is done by simple linear tests such as patch tests, Cook's membrane and a plate with a circular hole.

Subsequently, nonlinear tests of the element are performed with von Mises yield criteria in order to ensure that the the nonlinear part of the program is implemented correctly.

Finally, nonlinear tests of the element are performed using the Mohr-Coulomb material model. A set of tests is carried for the case of a strip footing resting on a soil layer in order to examine the performance of the element in the evaluation of the bearing capacity. The performance of the new extended element is compared with the performance of the LST element in the above-mentioned tests.

2 Formulation of the extended triangular element

In the following, the formulation of the new extended triangular element (EXT) is outlined. The element is based on the idea of combining the computational speed of having few global d.o.f. with the accuracy of having more internal d.o.f.

The new extended element is based on the quadratic-strain triangular element (QST), which is a 10-node element of 3. order. The element with its 10 nodes and 20 d.o.f., is shown in Figure 2.1.

As the aim of this work is to reduce the computational costs of solving geotechnical problems, it is intended to describe the QST element with fewer global nodes and d.o.f. This is done by reduction and static condensation of d.o.f. [11].

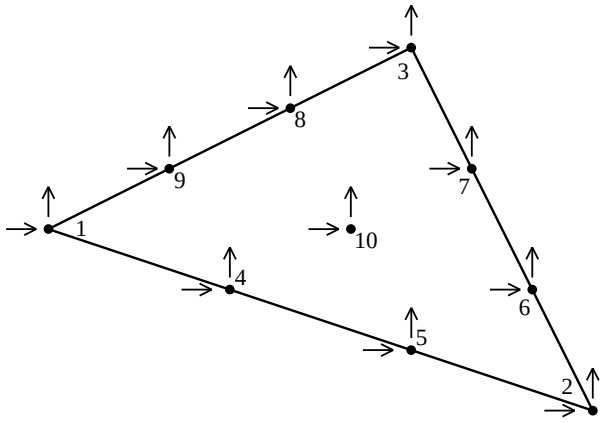

Figure 2.1: The quadratic-strain triangle and its 20 nodal d.o.f.

The QST element is reformulated to an element with 7 nodes by converting the 6 side nodes to 3 midside nodes. For each midside node, this results in 2 translational d.o.f. and 2 gradient d.o.f. As seen on Figure 2.2, the element still have 20 d.o.f. but only 7 nodes. This element forms the basis for the extended triangular element, and is subsequently mentioned as the full extended element (F-EXT).

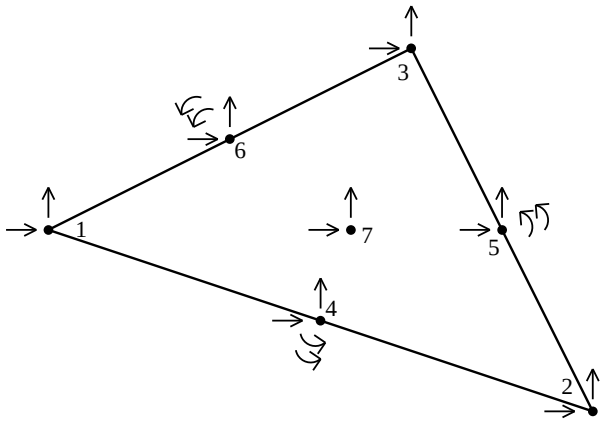

Figure 2.2: The full extended triangle element (F-EXT) and its 20 nodal d.o.f.

In order to produce the extended triangular element, the 2 gradient d.o.f. at each midside node and the 2 translational d.o.f. at the center node are expressed in terms of the remaining d.o.f. This can be done by allowing an incompatibility of gradients between elements. The reduction of d.o.f. is done by static condensation, which will be described in Section 2.1.

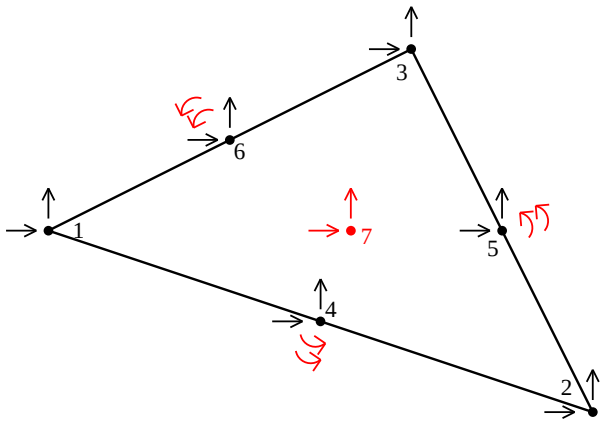

Figure 2.3: The extended triangle element (EXT) and the 8 condensed nodal d.o.f. represented with a red color.

The extended triangular element is illustrated in Figure 2.3, where the d.o.f. to be condensed are represented with a red color. These d.o.f. only acts within the element, giving the EXT element the advantages of rotations of the sides of the element.

The black d.o.f. are the global d.o.f. connected to adjacent elements. Globally, the EXT element has 6 external nodes; 3 corner nodes and 3 midside nodes. This is similar to the linear-strain triangular element (LST) which is shown in Figure 2.4.

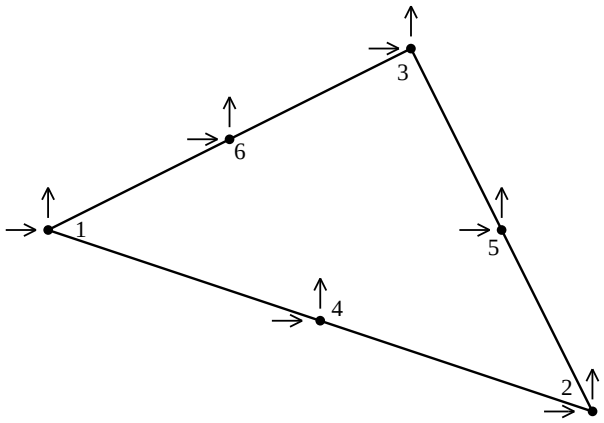

Figure 2.4: The linear-strain triangle and its 12 nodal d.o.f.

As mentioned, the 2 rotational d.o.f. at each midside node and the 2 translational d.o.f. at the center node are condensed before assembling the elements, i.e. the 20 d.o.f. are condensed to 12 d.o.f. When assembling the elements stiffness matrices into the global stiffness matrix, a less storages space is needed due to the reduction in global d.o.f. Hence, the cost of solving the global equations will practically be the same as for a regular 6-node triangular element.

Thus, the new element can possibly be very efficient in geotechnical problems due to the low computational costs of few global d.o.f., the accuracy provided by the internal d.o.f. and the flexibility from being an incompatible element.

2.1 Condensation of element vectors and matrices

The EXT element is defined internally by 20 d.o.f. as described in the previous section. When the element is assembled in a global system, 8 of these d.o.f. are condensed in order to express the element by 12 translational d.o.f. This means that the d.o.f. to be condensed are not connected to the d.o.f. of the other elements. The d.o.f. to be retained are d.o.f. on the element boundary, and are connected to the corresponding d.o.f. of the other elements. Static condensation is also known as a special case of substructuring [11].

The condensation is carried out by explicit matrix operations. The general term for each element $[K]\{u\} = \{Fr\}$ is given by:

$$\begin{bmatrix} [K_{rr}] & [K_{rc}] \\ [K_{cr}] & [K_{cc}] \end{bmatrix} \begin{Bmatrix} \{u_r\} \\ \{u_c\} \end{Bmatrix} = \begin{Bmatrix} \{Fr_r\} \\ \{Fr_c\} \end{Bmatrix}$$

Where the residual force vector applied to the element nodes is associated with the external force vector $\{F^{ext}\}$ and the internal force vector $\{F^{int}\}$:

$$\{Fr\} = \{F^{ext}\} - F^{int}\} \tag{2.1}$$

The indices r and c are retained and condensed d.o.f., respectively. The d.o.f. to be retained are all translational d.o.f. at corner nodes and midside nodes and are marked with a blue color on Figure 2.5:

$$r = [1\ 2\ 3\ 4\ 5\ 6\ 7\ 8\ 9\ 10\ 11\ 12] \tag{2.2}$$

While the d.o.f. to be condensed are the rotational gradients at midside nodes and translations of the middle node, and are marked with a red color on Figure 2.5:

$$c = [13\ 14\ 15\ 16\ 17\ 18\ 19\ 20] \tag{2.3}$$

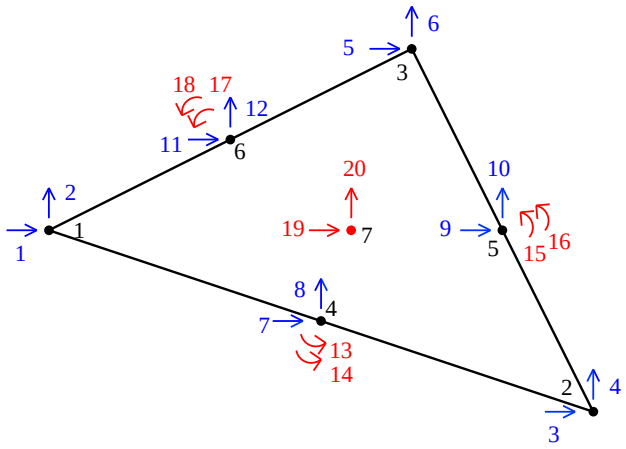

Figure 2.5: The EXT element with its 6 global nodes marked with black, 12 global d.o.f. marked with blue and 8 internal d.o.f. marked with red.

The condensed stiffness matrix for an element can be determined by:

$$[K_{red}] = [K_{rr}] - [K_{rc}]\,[K_{cc}]^{-1}\,[K_{cr}] \tag{2.4}$$

The condensed residual load vector for an element can be determined by:

$$\{Fr_{red}\} = \{Fr_r\} - [K_{rc}]\,[K_{cc}]^{-1}\{Fr_c\} \tag{2.5}$$

Thereby the condensed stiffness matrix can be assembled in a global stiffness matrix $[SysK]$ and the condensed residual load vector can be assembled in a global load vector $SysFr$ to produce the global equation:

$$[SysK]\{SysU\} = \{SysFr\} \tag{2.6}$$

where $SysU$ contains the retained d.o.f. u_r from all elements. After solving the global equation, the retained d.o.f. u_r are known, and the condensed d.o.f. u_c can be determined by solving:

$$\{u_c\} = [K_{cc}]^{-1}\,(\{Fr\}_c - [K_{cr}]\,\{u_r\}) \tag{2.7}$$

Thereby the full displacement vector containing contributions from both the retained and condensed d.o.f. can be assembled and used to determine the strains/stresses and the internal force vector.

2.2 Interpolation functions

In this section the interpolation functions of the F-EXT element are described. These functions are identical for the EXT element. Within the element the translational displacements $\{u\} = (u \quad v)^T$ and gradients of the displacements $\{u\}$ are obtained from the nodal values $\{d\} = (d_1 \ d_2 \ \ldots \ d_n)^T$ using interpolation functions assembled in the matrix $[N]$:

$$\{u\} = [N] \cdot \{d\} \tag{2.8}$$

Hence, the interpolation functions N_i are used to interpolate values inside the element based on known values in the nodes. The interpolation functions are also denoted as the shape functions.

The derivatives of the shape functions are used to compute the element stiffness matrix, as shown in Section B. Furthermore, the shape functions are used to convert distributed surface loads to consistent nodal loads. This is done in Section 2.3.

For triangular elements it is convenient to express the shape functions in terms of area coordinates, shown in Figure 2.6. The shape functions are all proposed by L. Damkilde [15].

$$\lambda_1 = \frac{A_1}{A} \qquad \lambda_2 = \frac{A_2}{A} \qquad \lambda_3 = \frac{A_3}{A} \tag{2.9}$$

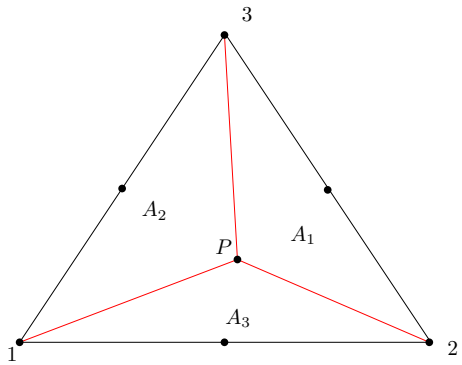

Figure 2.6: A triangle divided into areas in order to produce area coordinates.

For the translational displacement of a corner node the shape function is given as:

$$N_i = \lambda_i \left(2\,\lambda_i^2 + 2\,\lambda_j^2 + 2\,\lambda_k^2 + 3\,\lambda_j\,\lambda_k - 1\right) \qquad \text{for} \qquad i = 1, 2, 3 \tag{2.10}$$

The shape function for the translation displacement of a corner node is seen in Figure 2.7. As seen on the figure, the two sides adjacent to the corner node is stretched in the y-direction, while the side opposite to the corner node remains undeformed.

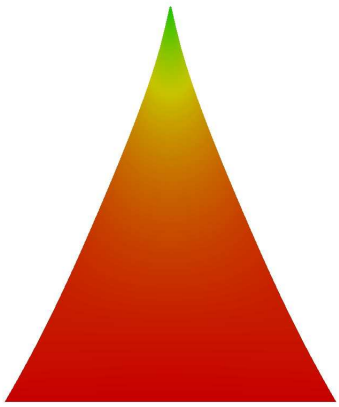

Figure 2.7: Shape function for the translational displacement in the y-direction the top corner node.

The shape functions for the translational displacements in the midside nodes are given by Eq. 2.11 and illustrated in Figure 2.8. The side on which the midside node is located is the only side that deforms when the shape function is activated.

$$N_{3+i} = 12\,\lambda_i\,\lambda_j\,\left(-\lambda_k + \frac{1}{3}\right) \qquad \text{for} \qquad i = 1,2,3 \tag{2.11}$$

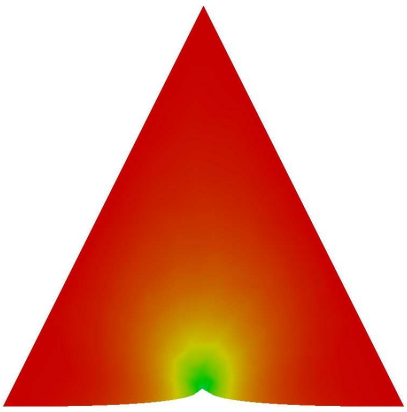

Figure 2.8: Shape function for the translational displacement in the bottom midside node.

The shape functions for the gradients in the midside nodes are given by Eq. 2.12 and are illustrated in Figure 2.9.

$$N_{6+i} = l_k\;\; 2\,\lambda_i\,\lambda_j(\lambda_i - \lambda_j) \qquad \text{for} \qquad i = 1,2,3 \tag{2.12}$$

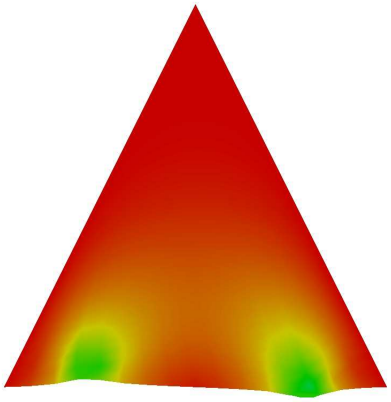

Figure 2.9: Shape function for rotational gradients in the midside nodes.

The shape function for the translational displacements in the center node is given by Eq. 2.13. It is defined by the triangle-bubble function as illustrated in Figure 2.10. All sides of the triangle remain undeformed by the shape function.

$$N_{10} = 27\,\lambda_i\,\lambda_j\,\lambda_k \tag{2.13}$$

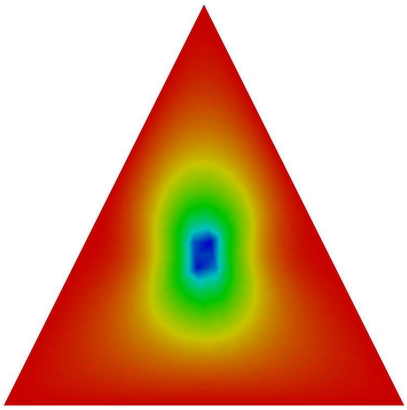

Figure 2.10: Shape function for the displacement in the center node.

2.3 Nodal loads

In this section it is explained how distributed loads applied to the side lines of an element are converted to consistent nodal loads. The distributed loads are converted by use of the shape functions [11]:

$$\{F\} = \int_s \{N\}^T \, p \, dS \tag{2.14}$$

where
$\{F\}$ is the vector of consistent nodal loads,
$\{N\}$ is the shape function vector, and
p is the distributed load function.

As an example of equation Eq. 2.14 a distributed load varying over the side of an element is considered, see Figure 2.11. The load p is given by a function of the side length x:

$$p = q_1 + (q_2 - q_1)\,\frac{x}{L} \tag{2.15}$$

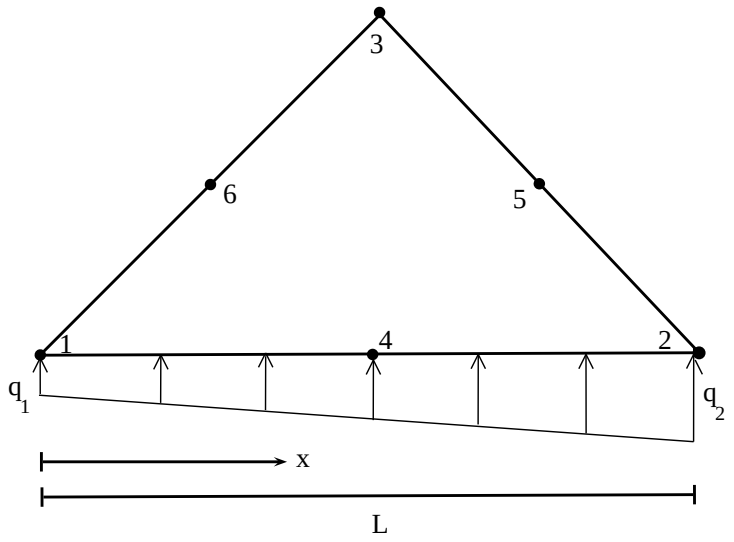

Figure 2.11: Distributed load on a side line of the EXT element.

Thus, the nodal loads associated with the distributed load on the side of the element with the length L can then be determined by:

$$\begin{Bmatrix} F_1 \\ F_2 \\ F_4 \\ F_7 \end{Bmatrix} = \int_0^L \{N\}^T \left\{ q_1 + (q_2 - q_1)\,\frac{x}{L} \right\} dx \tag{2.16}$$

$$= \int_0^L \begin{Bmatrix} 2\,{\lambda_1}^3 + 2\,\lambda_1\,{\lambda_2}^2 - \lambda_1 \\ 2\,{\lambda_2}^3 + 2\,{\lambda_1}^2\,\lambda_2 - \lambda_2 \\ 4\,\lambda_1\lambda_2 \\ L(2\,{\lambda_1}^2\,\lambda_2 - 2\,\lambda_1\,{\lambda_2}^2) \end{Bmatrix} \left\{ q_1 + (q_2 - q_1)\,\frac{x}{L} \right\} dx \tag{2.17}$$

The shape functions used in Eq. 2.17 is stated in Eq. 2.10 - Eq. 2.12. Notice, that the area coordinate λ_3 in the shape functions is equal to zero, as shown Figure 2.12.

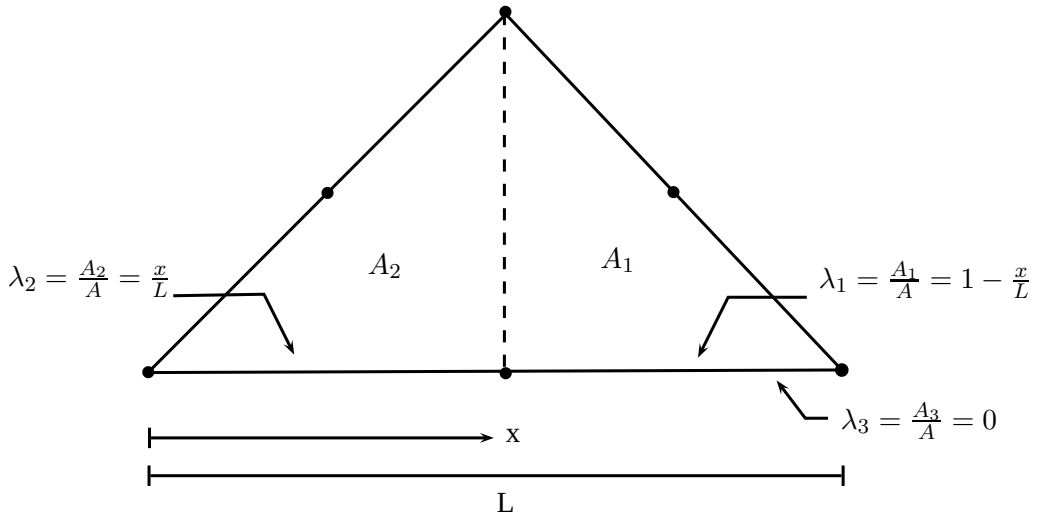

Figure 2.12: Area coordinates defined at side 3 of the triangular element.

In order to integrate Eq. 2.17 the area coordiantes is formulated as functions of the side length x, as illustrated in Figure 2.12. Thereby the integration of Eq. 2.17 gives the nodal loads:

$$\begin{Bmatrix} F_1 \\ F_2 \\ F_4 \\ F_7 \end{Bmatrix} = \int_0^L \begin{Bmatrix} 1 - \frac{5x}{L} + \frac{8x^2}{L^2} - \frac{4x^3}{L^3} \\ \frac{x}{L} - \frac{4x^2}{L^2} + \frac{4x^3}{L^3} \\ \frac{4x}{L} - \frac{4x^2}{L^2} \\ L(\frac{2x}{L} - \frac{6x^2}{L^2} + \frac{4x^3}{L^3}) \end{Bmatrix} \left\{ q_1 + (q_2 - q_1) \frac{x}{L} \right\} dx$$

$$= q_1 \begin{Bmatrix} \frac{1}{6}L \\ \frac{1}{6}L \\ \frac{2}{3}L \\ 0 \end{Bmatrix} + (q_2 - q_1) \begin{Bmatrix} \frac{1}{30}L \\ \frac{2}{15}L \\ \frac{1}{3}L \\ -\frac{1}{30}L^2 \end{Bmatrix}$$

Hence, if the applied load is uniformly distributed ($q_1 = q_2$) then the equation suggests that $\frac{1}{6}$ of the load on the side line is applied to each corner node and $\frac{2}{3}$ to the midside node of the element, see Figure 2.13. These results do not require that the distributed load act normal to the line.

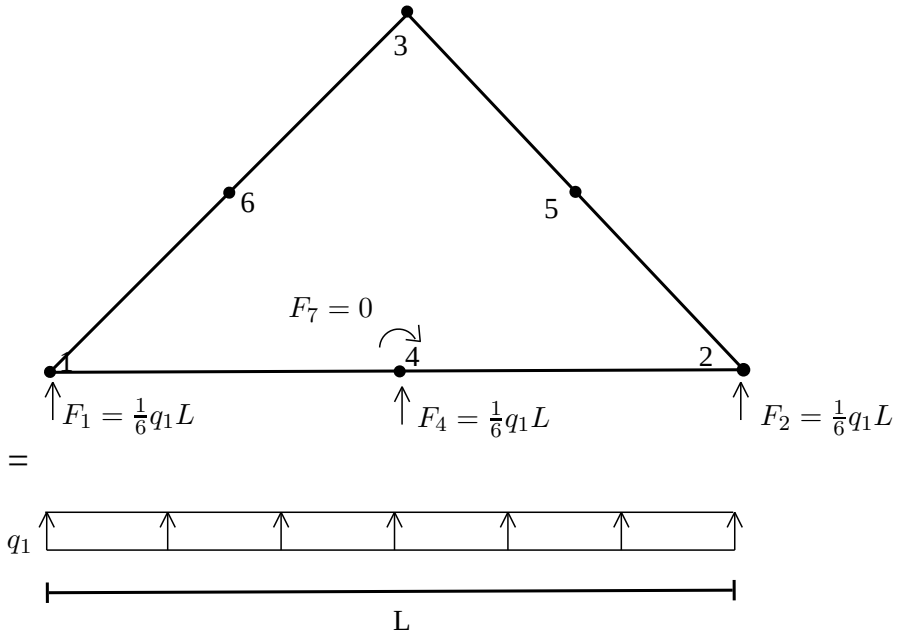

Figure 2.13: Application of uniformly distributed side load.

3 Linear tests of the extended element

The linear tests presented in Appendix C is conducted in order to validate the implementation of the extended element (EXT) and the full extended element (F-EXT) in the finite element code in Matlab. The tests performed include simple patch tests, Cook's membrane, a plate with a hole, and a strain energy test. These tests makes use of most of the parameters which influences the element accuracy. Parameters which influences accuracy are loading, element geometry, test geometry, material properties etc.

Inaccuracies of the element can occur by the presence of spurious modes induced of inadequate connections of elements, rank faults e.g. in connection with d.o.f., locking effects, elementary defects like rigid body motion etc. [11]. The patch tests should ensure that these defects is not present.

3.1 Patch and stability tests

The patch test performed in Appendix C.1 shows that the EXT and F-EXT elements are able to display a constant state of strains/stresses and thereby pass the patch test. It is possible for an element to pass the patch test even though it is unstable. Provided that the element is stable, it is able to exhibit rigid body motion without strains/stresses, states of constant strains/stresses, and compatibility between elements [11]. These requirement is necessary to guarantee convergence. Accordingly, the patch test is also applied to verify stability.

A stability test, see Appendix C.2, displays consistency between applied loads and calculated displacements. Another way to check stability of an element, is by determining if all eigenvalues of the stiffness matrix are positive. This is the case with the extended element, and therefore it passes the stability test.

However, the previous tests do not show how well the EXT and the F-EXT elements performs in other applications. The elements may in other applications provide a poor accuracy in a coarse mesh or provide a slow convergence rate. Thus, additional tests of the elements are performed with the intention to compare the performance of the element to the performance of the LST element.

3.2 Cook's membrane test

In Appendix C.3 the well-known test concerning Cook's membrane is performed with different meshes. This test verifies whether the extended element can provide a better accuracy and convergence rate for a linear elastic problem, than the linear-strain element [6].

The geometry of Cook's membrane is shown in Figure 3.1 with two different meshes, and it appears that the problem include both shear and bending combined with the geometry

distortion. The right side of the model is loaded by a constant traction of P=1 in the y-direction, and the left side of the model is restrained in the x- and y-direction. The modulus of elasticity is $E = 1$ and Poisson's ratio is $\nu = 0.333$.

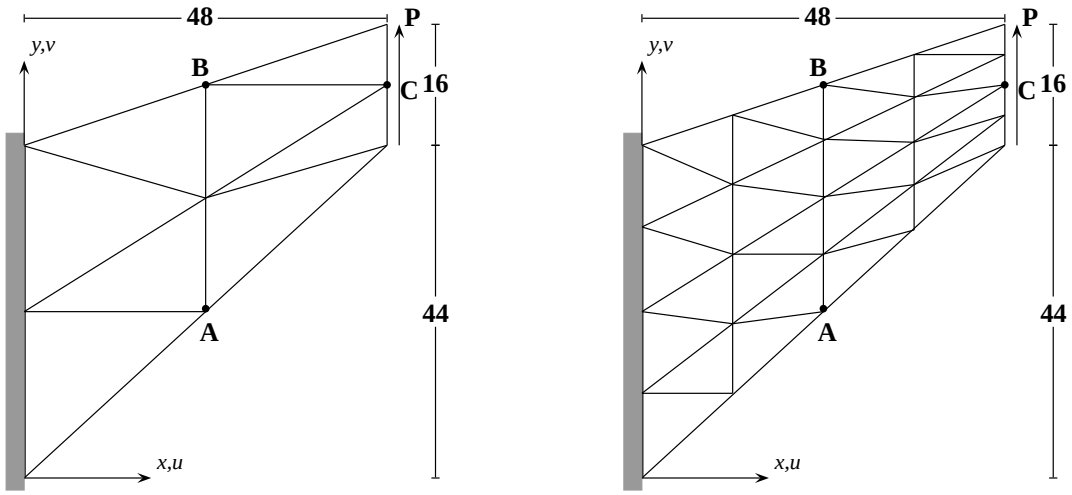

Mesh 2x2. Mesh 4x4.

Figure 3.1: Cook's membrane with mesh 2x2 and mesh 4x4.

The vertical displacement at point C and the maximum and minimum principal stress at the points A and B, respectively, are compared for the elements mentioned in Section 2. There is no known theorictical solutions, but the results provided by Bergan & Felippa [18] and Felippa & Alexander [4] are used for comparison purposes.

The convergence of displacements of the point C with respect to number of d.o.f. are displayed in Figure 3.2.

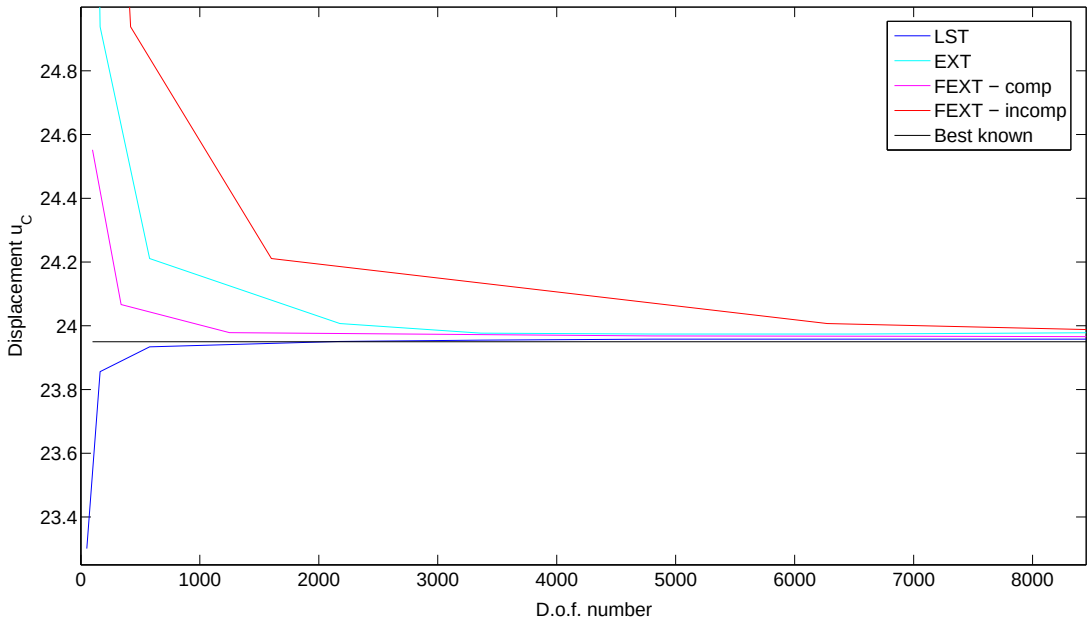

Figure 3.2: Convergence of displacements u_C with respect to number of d.o.f., close-up.

When comparing the displacement results with the best known results, it is seen that the convergence of EXT is poor compared to LST. It is also evident that the displacements calculated by EXT is higher than the displacements calculated by LST. This indicates that the extended element is too flexible to provide accurate results in a linear analysis.

Likewise, it is seen that the convergence of the F-EXT incompatible element is poor compared to LST. On the other hand it is seen that the F-EXT compatible element converges as fast as LST, and that the accuracy of the F-EXT compatible element is high even for coarse meshes.

In Figure 3.3 and Figure 3.4 the convergence of maximum and minimum principal stresses in the points A and B are illustrated with respect to d.o.f.

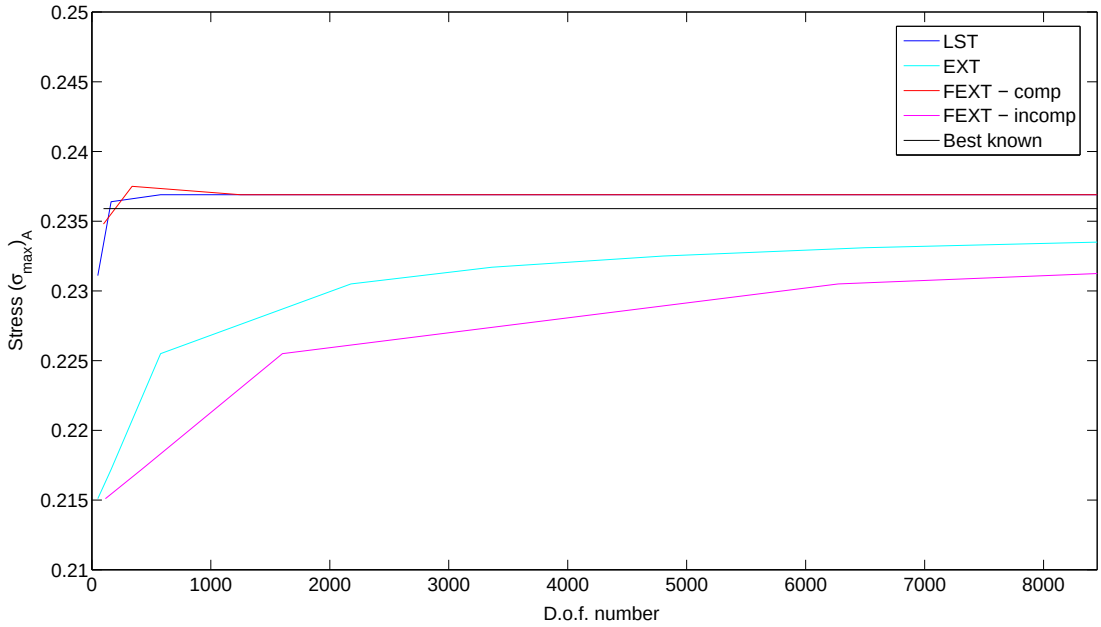

Figure 3.3: Convergence of stress $(\sigma_{max})_A$ with respect to number of d.o.f.

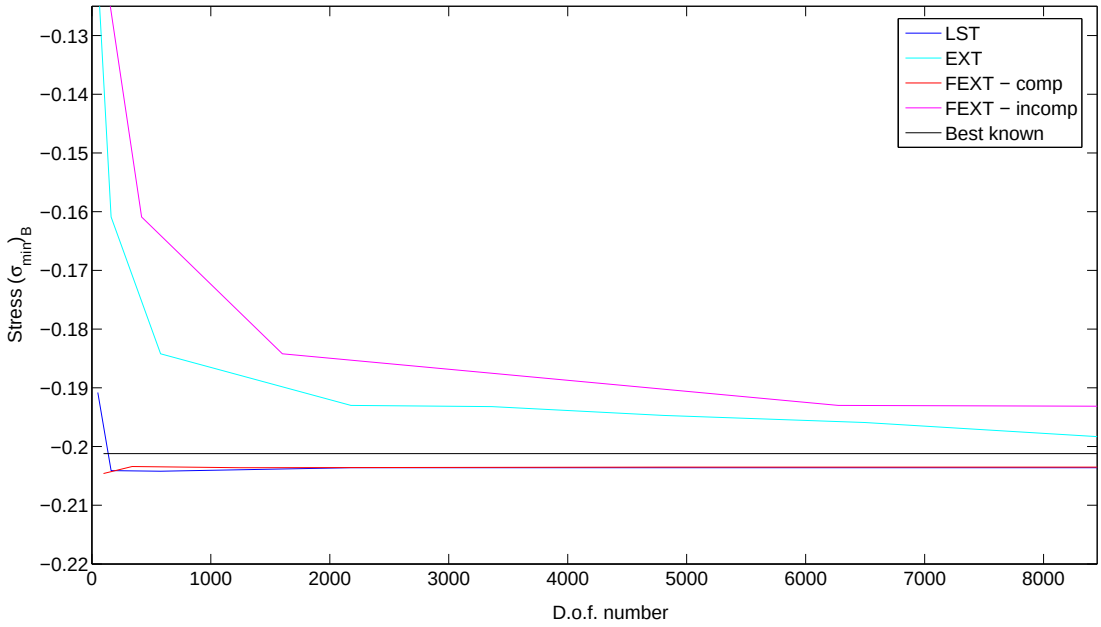

Figure 3.4: Convergence of stress $(\sigma_{min})_B$ with respect to number of d.o.f.

Likewise, it is seen that the convergence of principal stresses computed for the EXT element and the F-EXT incompatible element is poor compared to LST. However, it is seen that the convergence of the principal stresses computed for the F-EXT compatible is good compared to LST.

3.3 Plate with hole

The problem considered in the following test is a plate with a circular hole, which is loaded by a force per unit area on its edge. The plate is shown in Figure 3.5. The plate is assumed to be made of a linear elastic material, with the material parameters $E = 1$ and $\nu = 0.3$. Furthermore the plate is considered to be very thin, and thereby the tests can be solved for a plane stress state.

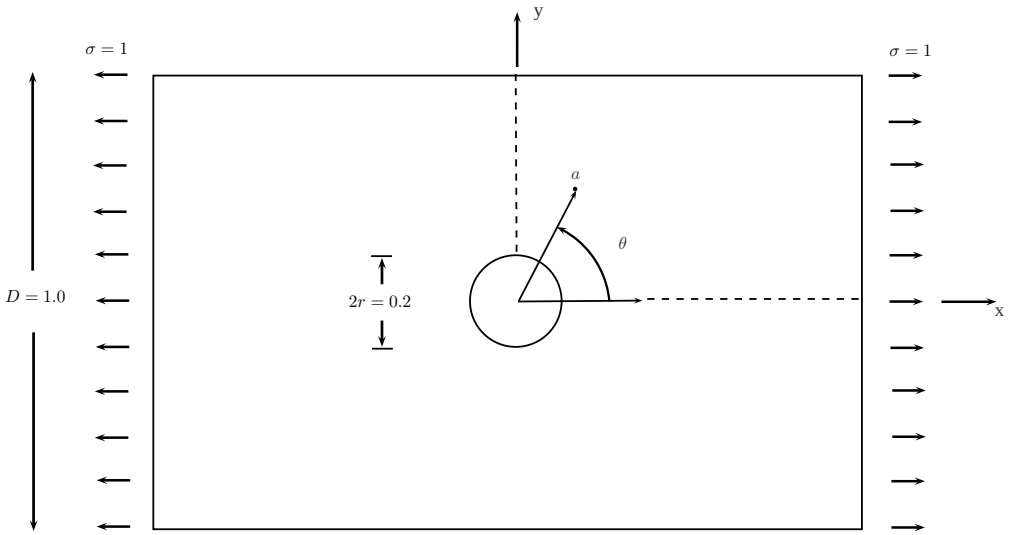

Figure 3.5: Plate with a circular hole, loaded in tension.

The problem is solved numerically with continuous mesh refinements, as shown in Appendix C.4, Figure C.9. The meshes is generated so that the elements near the hole are finer than those further from the hole, in this way the stress concentration around the hole is better described. Due to the axis symmetry only a quarter of the plate is discretized into a mesh.

The numerical results can be compared with the analytical solution given for a plate with an infinite length compared with the diameter for the hole. The solution for the stress throughout the plate is given by:

$$\sigma_\theta = \frac{\sigma}{2}\left(1 + \frac{r^2}{a^2} - (1 + 3\frac{r^4}{2\,a^4})\,cos(2\,\theta)\right) \tag{3.1}$$

where

r is the radius of the circular hole,
a is the radius of the stress location, and
θ is the related angle.

In Figure 3.6 the convergence of the maximum stress $\{\sigma_x\}_{\theta=90^\circ}$ at the edge of the hole is displayed for LST, EXT, F-EXT compatible and incompatible elements. It appears that the convergence of the EXT and F-EXT elements is poor compared to the convergence of the LST element. Furthermore problems with memory occurs in computation of the max-

imum stress with a very fine mesh of F-EXT incompatible elements due to the increasing number of d.o.f.

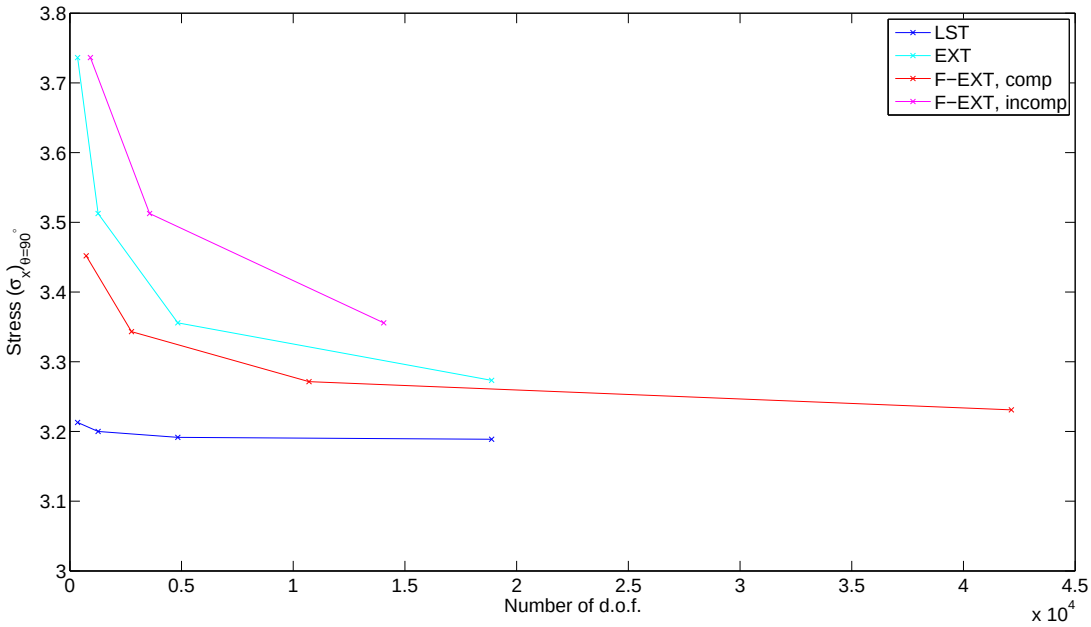

Figure 3.6: Convergence of maximum stress $\{\sigma_x\}_{\theta=90^\circ}$ at the edge of the hole.

Results of the normal stress along the vertical symmetry plane $\{\sigma_x\}_{\theta=90^\circ}$ computed for different meshes of LST elements, EXT elements, F-EXT compatible and incompatible elements are compared with the analytical solution of Eq. C.1. This is displayed in Figure 3.7, and in Figure C.12, Figure C.13 for refined meshes.

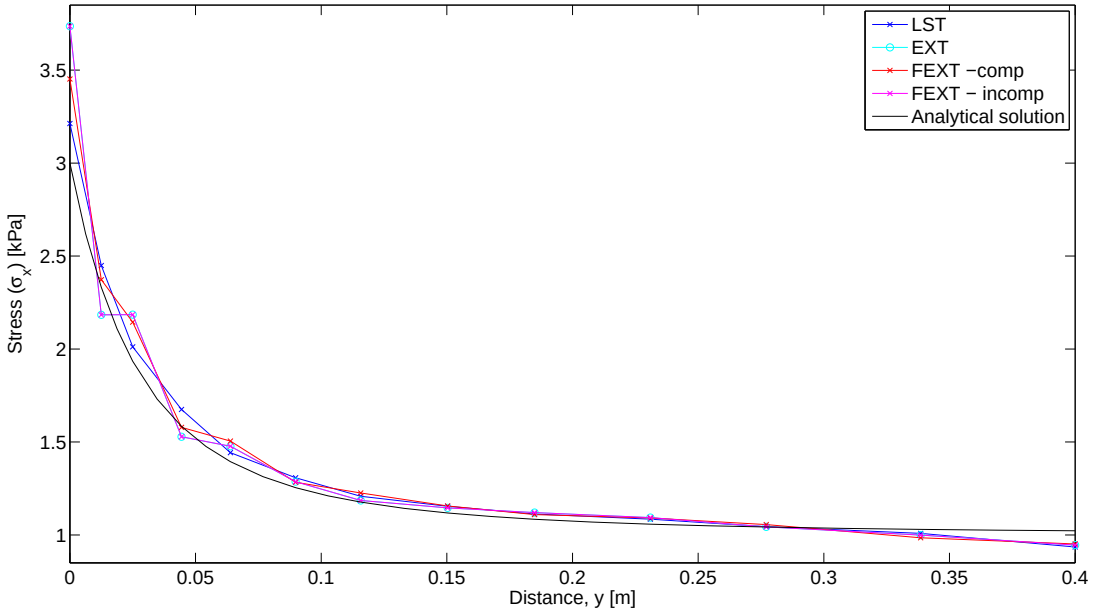

Figure 3.7: Normal stress σ_x along the vertical symmetry axis - mesh 1.

When comparing the numerical test results with the analytical results, it is seen that the results are not completely accurate for the numerical tests. The test results obtained with LST elements is more accurate than the results obtained with EXT elements, F-EXT compatible and incompatible elements. It appear that the results obtained with the EXT element are equal to the results obtained with the F-EXT incompatible element, and therefore it is evident that the behavior of the EXT and the F-EXT incompatible element is the same.

Common for the EXT element, the F-EXT compatible and incompatible element is that the influence of the gradients becomes significant for the stress results computed for a coarse mesh. The effect of the gradients is more expressive in the area around the hole, where large stress concentrations occurs. This is evident from the close-up on Figure 3.8, Figure **??** and Figure **??**:

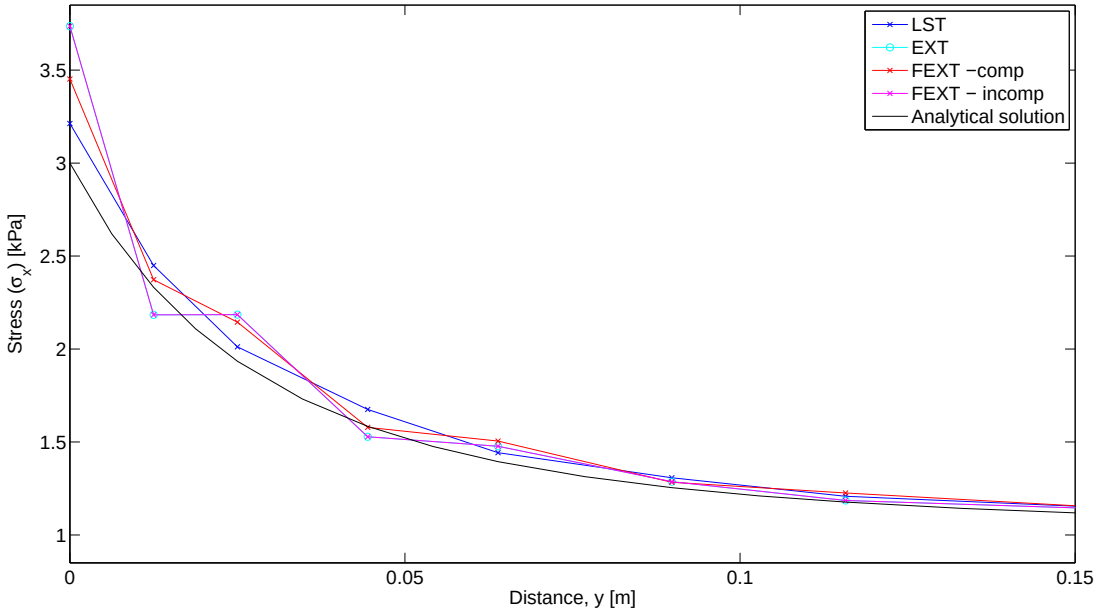

Figure 3.8: Close-up of the stress along the vertical symmetry axis - mesh 1.

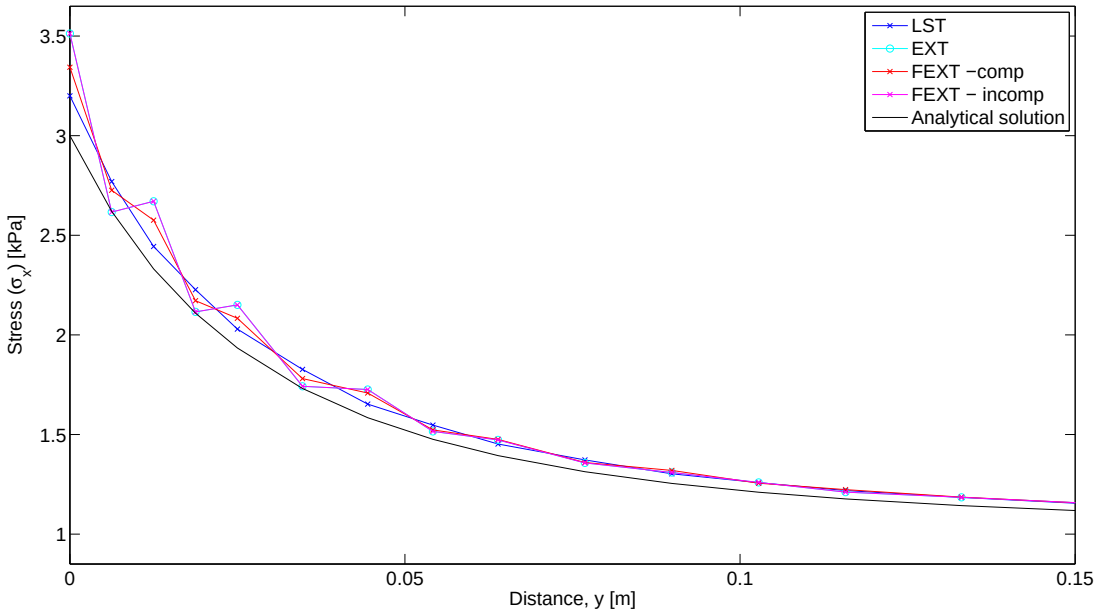

Figure 3.9: Close-up of the stress along the vertical symmetry axis - mesh 2

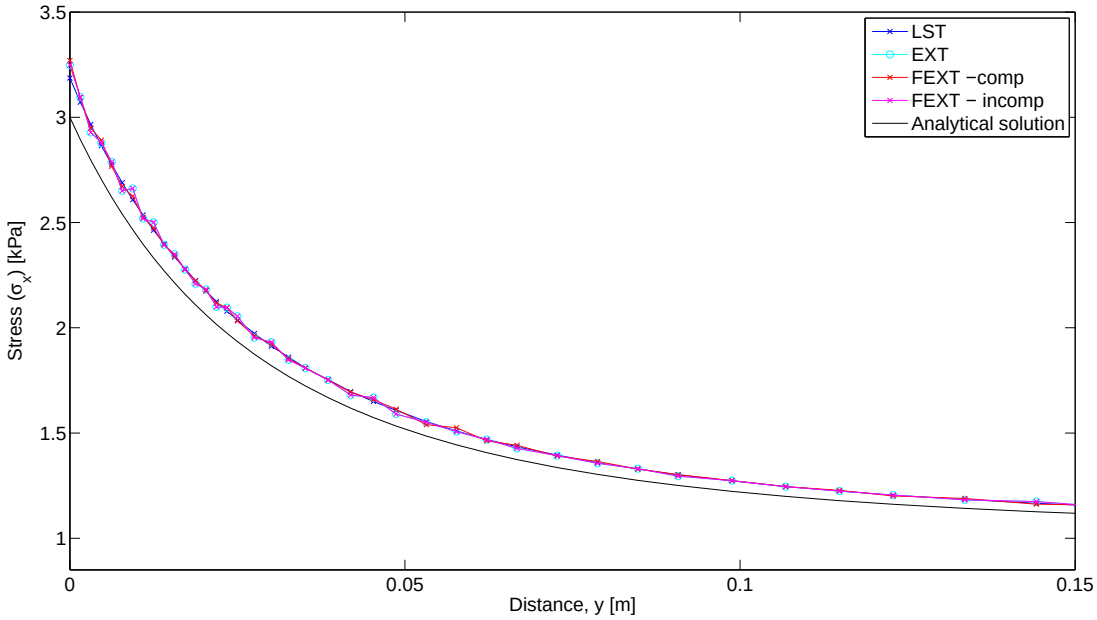

Figure 3.10: Close-up of the stress along the vertical symmetry axis - mesh 3

The influence of the gradients is more significant for the the EXT and the F-EXT incompatible compared with the F-EXT compatible element. Only for a very fine mesh the influence of the gradients becomes insignificant.

3.4 Conclusion

The tests presented in the previous sections indicates that the extended element is too flexible to provide accurate results for coarse meshes in linear analyses. However, this is a normal behaviour for incompatible elements and does not imply that it will perform poorly in other applications [11].

As shown in Section 1.1, the conventional elements overestimates the stability of a slope and the bearing capacity of a footing resting on soil. This suggests that the incompatibility of the element can be an advantage in nonlinear geotechnical analyses, because the element may not overestimate the bearing capacity of soil materials.

Therefore in the following the implementation of the element in Matlab is extended to nonlinear finite element analysis. Two material models is implemented, including the von Mises yield criteria and the Mohr-Coulomb yield criteria. The latter of the two criterias has been the basis in the calculations of geotechnicals problems for many years.

4 Nonlinear Finite Element Program

In this chapter the basic principles for computing the nonlinear finite element program is reviewed. This involves the iteration procedure, stress return to the yield surface, choices on updating the stiffness matrix, criteria and tolerance for convergence. The review is based on the case of perfect plasticity. In the following chapters, the von Mises and Mohr-Coulomb yield criterias are evaluated and tested for the different element types.

4.1 Incremental iteration procedure

The iteration procedure used in the program is the well-known Newton-Raphson routine. In this routine, the applied loads and prescribed displacements are divided into increments denoted i. For each increment, the routine iterates towards a solution that fulfills a given tolerance for equilibrium.

To start up the iteration procedure, with iterations denoted j, an initial guess of the displacement vector is needed, $\{dU\}_{i,j}$. The initial guess is taken as the converged displacement vector at the end of the last load step:

$$\{dU\}_{i,j} = \{dU\}_{i-1,j} \tag{4.1}$$

In the first load step the guess is initialized, $\{dU\}_{i-1,j} = 0$. Furthermore in the first iteration step the corrector displacement vector is initialized, $\{ddU\}_{i,j} = 0$. Consequently, the strains, stresses and internal forces computed in the first load step and the first iteration is zero.

The incremental strain vector, $\{d\varepsilon\}_{i,j}$, is computed from the incremental displacement vector, $\{dU\}_{i,j}$, using:

$$\{d\varepsilon\}_{i,j} = [B]\{dU\}_{i,j} \tag{4.2}$$

The incremental strain vector $\{d\varepsilon\}_{i,j}$ is used together with the strain vector from the last increment $d\varepsilon\}_{i,j-1}$ to compute an updated stress vector $\{\sigma\}_{i,j}$, see Section 4.2 and Section 4.3.

Depending on the updating method, see Section 4.4, the updated stress $\{\sigma\}_{i,j}$ can be used to compute the updated constitutive matrix $[D]^p_{i,j}$. The consitutive matrix is then used to determine the local tangent stiffness matrices:

$$[Ke]_{i,j} = \int [B]^T \, [D]^p_{i,j} \, [B] \, dV \tag{4.3}$$

The updated stress $\{\sigma\}_{i,j}$ is also used to calculate the local internal force vector:

$$F^{int}_{i,j,k} = \int [B]^T \{\sigma_{i,j}\} dV \tag{4.4}$$

Subsequently, the local residual force vector is determined using the external force vector and the internal force vector:

$$\{Fr\}_{i,j} = \{F\}^{ext}_{i} - \{F\}^{int}_{i,j} \tag{4.5}$$

When the global residual force vector is assembled, the reaction forces are take into account, i.e.:

$$\{SysFr\}_{i,j} = \{SysF\}_{i,j} + \{SysR\}_{i,j} - \{SysI\}_{i,j} \tag{4.6}$$

where $\{SysF\}_{i,j}$ is the global external force vector, $\{SysR\}_{i,j}$ is the global reaction force vector, and $\{SysI\}_{i,j}$ is the global internal force vector.

The global reaction force vector is extracted from the global internal force vector:

$$\{SysR\}_{i,j} = \{SysI(b_{dof})\}_{i,j} + \{SysI(p_{dof})\}_{i,j} \tag{4.7}$$

where b_{dof} indicates the restrained d.o.f. and p_{dof} indicates the d.o.f. with prescribed displacements.

The global equation is then solved for the unknown iterative displacements $\{ddU_{i,j}\}$, i.e. only the part of the global equation concerning the displacements in free d.o.f. is solved. In the first iteration Eq. 4.8 is used, and in the following iterations Eq. 4.9 is used:

$$\{ddU\}_{i,j} = [SysK(f_{dof}, f_{dof})]^{-1}([SysFr(f_{dof})] - [SysK(f_{dof}, pp_{dof})]\{d(pp_{dof})\}) \tag{4.8}$$

$$\{ddU\}_{i,j} = [SysK(f_{dof}, f_{dof})]^{-1}\,[SysFr(f_{dof})][SysFr(f_{dof})] \tag{4.9}$$

where f_{dof} are the free d.o.f., pp_{dof} are the restained and precribed d.o.f., $\{d(pp_{dof})\}$ are the displacement values in the restrained and prescribed d.o.f.

With the soultion of $\{ddU\}_{i,j}$ a correction of the incremental displacement can be computed:

$$\{dU\}_{i,j} = \{dU\}_{i,j-1} + \{ddU\}_{i,j} \tag{4.10}$$

Then the next iteration step $j+1$ is carried out, with displacement input:

$$\{dU\}_{i,j+1} = \{dU\}_{i,j} \tag{4.11}$$

The iterations are repeated untill convergence criteria is satisfied, se Section 4.1.1. When the iterations in an incremental step is terminated, the global displacement is updated with $\{dU\}_{i,j}$ and the next incremental step is carried out. If the convergence criteria is not satisfied within a reasonable number of iterations, the solution is terminated. The iteration procedure is outlined in Flowchart 4.1.

Flowchart 1: Iteration procedure for nonlinear FEM

$SysU = 0$	Initialize global displacement vector
Load Loop *i=1:numstep*	
$dU_i = 0$	Initialize incremental displacement vector
Iteration Loop *j=1:itstep*	
$dU_{i,j} = dU_{i,j-1}$	Initial guess of incremental displacement
$ddU_{i,j} = 0$	Initialize corrector displacement vector
$SysK = 0$	Initialize global stiffnes matrix
$SysI = 0$, $SysR = 0$ and $SysFr = 0$	Initialize global internal force vector, reaction vector and residual force vector
Element Loop *k=1:numel*	
$d\varepsilon_{i,j,k} = B \cdot dU_{i,j,k}$	Calculate incremental strain
$\sigma_{i,j,k}(d\varepsilon_{i,j-1,k}, d\varepsilon_{i,j,k})$	Update stress
$F^{int}_{i,j,k} = \int B^T \sigma_{i,j,k}$	Calculate local internal force vector
$D^p_{i,j,k}(\sigma_{i,j,k})$	Update constitutive matrix
$Ke_{i,j,k}\ (D^p_{i,j,k})$	Calculate local stiffness matrices
$SysK_{i,j}$, $SysI_{i,j}$, $SysF_{i,j}$	Assemble global stiffness matrix, global internal force and external force
End Element Loop *k=numel*	
$SysFr_{i,j} = SysF + SysR - SysI$	Calculate global residual force vector
$ddU_{i,j} = SysK^{-1} SysFr$	Calculate iterative displacement
$dU_{i,j} = dU_{i,j-1} + ddU_{i,j}$	Correct incremental displacement
Check convergence	
End Iteration Loop *j=itstep*	
$SysU_{i+1} = SysU_i + dU_{i,j+1}$	Update global displacement vector
End Load Loop *i=numstep*	

4.1.1 Convergence criteria and tolerance

The termination of the iterations in a incremental step is determined by the convergence criteria. The criteria relates to the convergence of the iterative solution, not the convergence of the discrete solution. In the matlab code the energy criteria is used to terminate the iterations:

$$U = \Sigma_e U^e = \Sigma_e \{d\}'[K_e]\{d\} \tag{4.12}$$

The energy criteria measures the sum of every elements' energy resulting from the residual. If the energy criteria is not satisfied, $U \neq 0$, there is an error in the iterative solution. The error tolerance used in the code determines the precision with which the criteria should be satisfied before terminating the iterations. The error tolerance have an influence on the speed and accuracy of the solution. If the tolerance is too high, the solution may be inaccuate. In the other hand, a tolerance which is too small results in unnecessary computations.

Usually an error tolerance of $tol = 1e^{-5}$ is used. In Section 9.2.2 a sensitivity analysis of the F-EXT incompatible element is carried out by changing the tolerance in the range of $1e^{-6} < \text{tol} < 1e^{-4}$.

4.2 Determining the plastic contributions

To determine the plastic part of a solution a trial elastic stress is computed, representing the stress state in point B, and it is determined if this point is outside the yield surface, see Figure 4.1. If so, a local iteration scheme is applied in order to return to the yield surface.

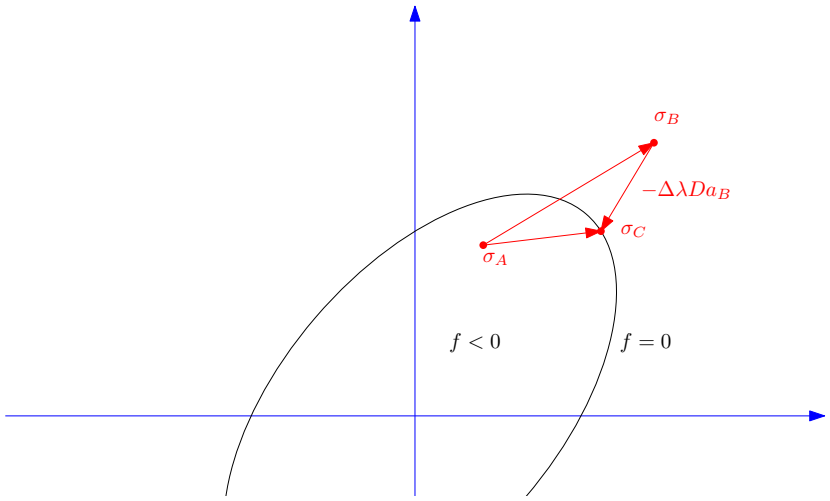

Figure 4.1: Backward-Euler stress return from inside the yield surface.

First, the difference between the trial stress and the yield surface is determined for the iteration increment j:

$$\sigma_B = D\left(\varepsilon_{i,j} - \varepsilon_{i,j-1}\right) \tag{4.13}$$

$$f_B = \sigma_e - \sigma_B \tag{4.14}$$

where the equivalent stress σ_{eff} is calcultated with respect to the yield function, see Chapter 5 for von Mises and Chapter 8 for Mohr-Coulomb.

If the difference $f_B > 1e^{-10}$, the trial stress is outside the yield surface. The trial stress can be returned to the yield surface with the use of a scalar, $\Delta\lambda$, called the plastic multiplier, which is computed by:

$$\Delta\lambda = \frac{f}{a^T\, D\, a} \tag{4.15}$$

With a being the flow vector, given as:

$$a = \frac{\partial f}{\partial \sigma} \tag{4.16}$$

This leads to a calculation of stress in point C, which is the first estimate of a stress on the yield surface:

$$\sigma_C = \sigma_B - \Delta\lambda\, D\, a_B \tag{4.17}$$

A graphic representation of this is seen in Figure 4.1. It is clear that if $f = 0$, the plastic multiplyer will also be 0, and the stress is on the yield surface.

4.3 Returning to the yield surface

The estimate of σ_C, described in the previous section, will most likely not be on the yield surface. Therefore, an iteration scheme called Backward-Euler is implemented in order to correct the trial stress back to the yield surface.

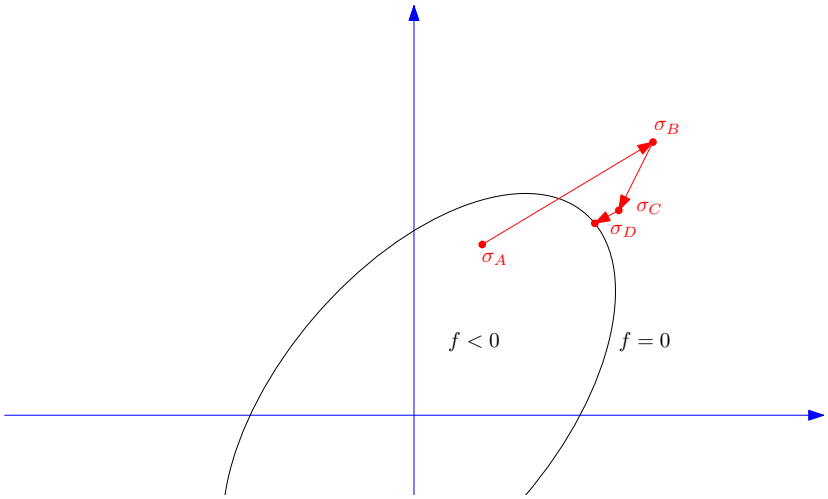

Figure 4.2: Return mapping.

With the stress in point C known, the yield state for C can be determined with use of either von Mises or Mohr-Coulomb's yield criteria. This gives the yield function f_C and the flow vector a_C.

It is inteded to reduce the difference between the current stress σ_C and the stress calculated with the use of a_C to almost zero:

$$r_C = \sigma_C - (\sigma_B - \Delta\lambda\, D\, a_C) < 1e^{-8} \tag{4.18}$$

This is done by determining the change in the plastic multiplier:

$$\dot{\lambda} = \frac{f_C - a_C^T\, Q^{-1}\, r_C}{a_C^T\, Q^{-1}\, D\, a_C} \tag{4.19}$$

where Q is defined in Eq. 4.24. The change in the stress in point C is also calculated:

$$\dot{\sigma_C} = -Q^{-1}\, r_C - \dot{\lambda}\, Q^{-1}\, D\, a_C \tag{4.20}$$

Then, the plastic multiplier and the stress is updated, and a new set of f_C and a_C can be computed:

$$\Delta\lambda = \Delta\lambda + \dot{\lambda} \tag{4.21}$$

$$\sigma_C = \sigma_C + \dot{\sigma_C} \tag{4.22}$$

If the relation between $\dot{\lambda}$ and $\Delta\lambda$ is less than $1e^{-8}$, r_C is reduced to almost zero, and the iteration procedure is done. If not, the iteration continues with the use of the new values.

4.4 Updating the stiffness matrix

The stiffness matrix can either be updated with the corrected constitutive matrix, $[D_p]$, for each iteration or for each loadstep or not be updated at all. The methods are also known as the Full Newton-Raphson, the Modified Newton-Raphson and the Initial Stiffness scheme, respectively [3]. The choise of a scheme has a great influence on how quickly the solution converges, as illustrated in Figure 4.3.

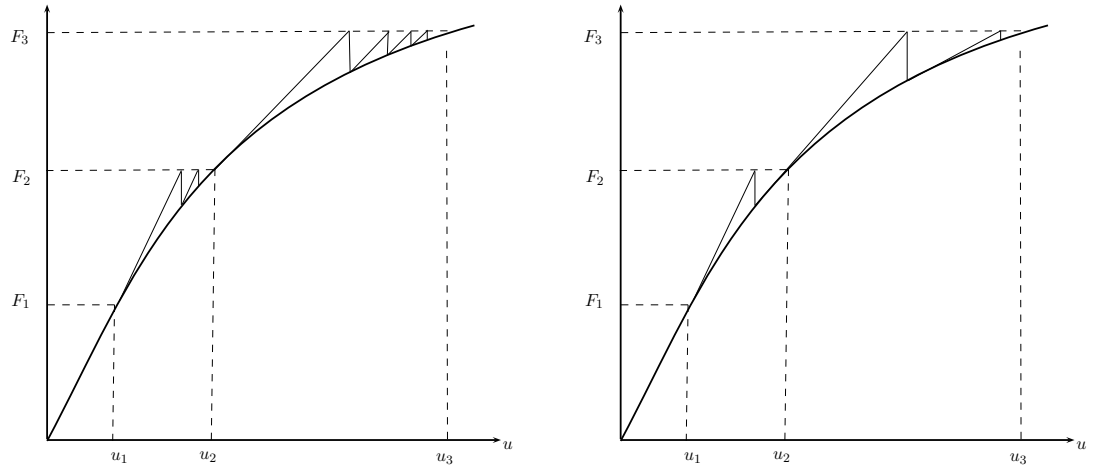

(a) Modified (b) Full

Figure 4.3: The choice between Newton-Raphson schemes has great influence on how fast the solution converges.

The simplest way to perform a nonlinear analysis is to use the initial stiffness matrix for each iteration and loadstep. It is a very cheap method regarding formulation of matrices, but it needs a lot of iterations to converge.

The modified scheme updates the stiffness matrix for each loadstep. It therefore needs more iterations than the previous mentioned method, but does not need as much memory as the stiffness matrix is only reformulated for every loadstep.

The Full Newton-Raphson scheme updates the stiffness matrix for each iteration. This means that it requires significantly more computer memory to reformulate the stiffness matrix with every iteration, but it also converges faster. All three methods is implemented in the Matlab program, but most analysis are done by the Full Newton-Raphson scheme.

The stiffness matrix is updated by the consistent constitutive matrix $[D]^{ep}$:

$$[Q] = [I] + \Delta\lambda\,[D]\,\{\frac{\partial a}{\partial \sigma}\} \tag{4.23}$$

$$[R] = [Q]^{-1}\,[D] \tag{4.24}$$

$$[D]^{ep} = [R]\,\left([I] - \frac{\{a\}\;[R]\,\{a\}^T}{\{a\}^T\,[R]\,\{a\} + A}\right) \tag{4.25}$$

where
$[I]$ is a unit matrix,
$\Delta\lambda$ is the plastic multiplier,
$[D]$ is the elastic matrix,
$[D]^{ep}$ is the elastic-plastic matrix,
$[R]$ is a helping matrix,
A is a hardning parameter, and
$\{a\}$ is the flow vector.

The flow vector $\{a\}$ dependent on the yield surface, is given by Chapter 5.

5 Von Mises yield criteria

In this chapter a short presentation of von Mises yield criteria for the states of plane stress and plane strain is provided. In the following chapter, patch tests with von Mises yield criteria are performed in order to validate the implementation of the extended element in the nonlinear finite element code.

By von Mises yield criteria associative plasticity is assumed ($f = g$) in which yielding encounter when the effective stress σ_e reaches a limiting value:

$$f = \sigma_e - \sigma_0 \tag{5.1}$$

where the effective stress in plane calculations is given by:

$$\sigma_e = \frac{1}{\sqrt{2}}\left((\sigma_x - \sigma_y)^2 + (\sigma_y - \sigma_z)^2 + (\sigma_z - \sigma_x)^2 + 6\tau_{xy}^2\right)^{1/2} \tag{5.2}$$

Two kinds of patch tests are performed - plane stress and plane strain tests. For plane stress, equation Eq. 5.2 is reduced by $\sigma_z = 0$, while for plane strain, i.e. $\varepsilon_z = 0$, the equation is the same as stated. The flow vector a used in the updating procedure is given by:

$$a = \frac{\partial f}{\partial \sigma} \tag{5.3}$$

which for an associative plasticity imply that the flow direction is normal to the yield surface. For plane stress the flow vector is then given by:

$$a = \frac{1}{2\sigma_e}\begin{bmatrix} 2 & -1 & 0 \\ -1 & 2 & 0 \\ 0 & 0 & 6 \end{bmatrix}\begin{bmatrix} \sigma_x \\ \sigma_y \\ \tau_{xy} \end{bmatrix} \tag{5.4}$$

while for plane strain:

$$a = \frac{1}{2\sigma_e}\begin{bmatrix} 2 & -1 & -1 & 0 \\ -1 & 2 & -1 & 0 \\ -1 & -1 & 2 & 0 \\ 0 & 0 & 0 & 6 \end{bmatrix}\begin{bmatrix} \sigma_x \\ \sigma_y \\ \sigma_z \\ \tau_{xy} \end{bmatrix} \tag{5.5}$$

6 Tests with von Mises yield criteria

The patch test with the use of von Mises yield criteria is performed for LST, EXT, F-EXT compatible and F-EXT incompatible in order to ensure that the elements can converge towards the exact solution. The cases of plane stress and plane strain are considered in the following sections.

Furhtermore, a test of a strip footing is carried out in order to examine how the elements performs, compared to the analytical solution.

6.1 Plane stress

In this section, the patch test is performed for plane stress. The geometry, mesh and boundary conditions are shown in Figure 6.1. The patch is subjected to a uniformly applied displacement of $u = 50$ in the x-direction.

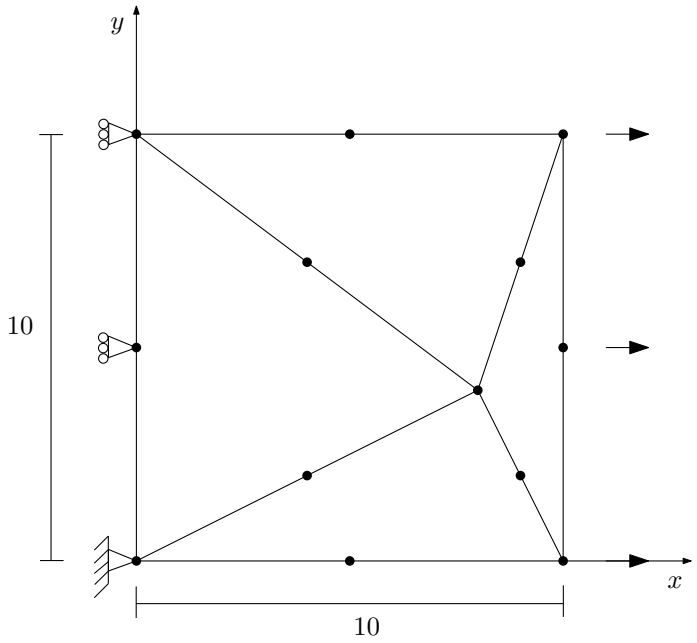

Figure 6.1: The geometry, mesh and boundary conditions for the plane stress patch test, with $u = 50$, $E = 1$, $\nu = 0.3$ and yield stress $y0 = 1$.

The test is done for both the Full and Modified Newton-Raphson iteration schemes. The results are displayed in Figure 6.2 and Figure 6.3.

It is clear from the graph that the EXT and the F-EXT elements do not converge when using the Modified and the Full Newton-Raphson schemes. Because it is a prerequisite for the EXT element to work, that the F-EXT element works properly, it is first examined why F-EXT does not converge.

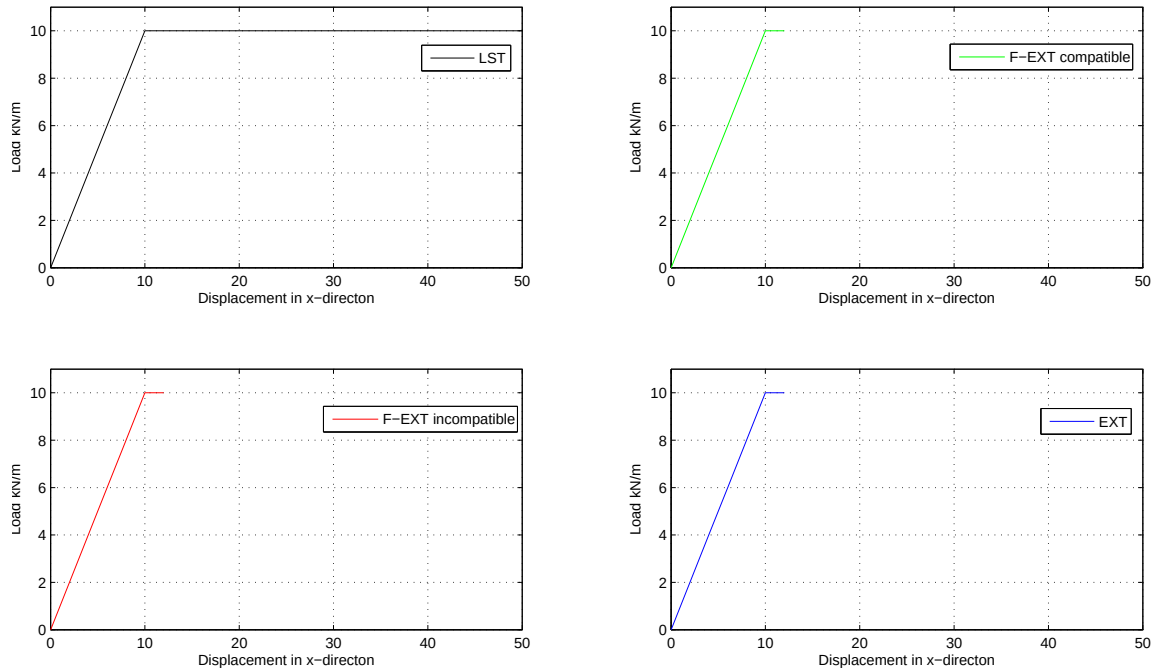

Figure 6.2: The results for the plane stress patch test using the Modified Newton-Raphson.

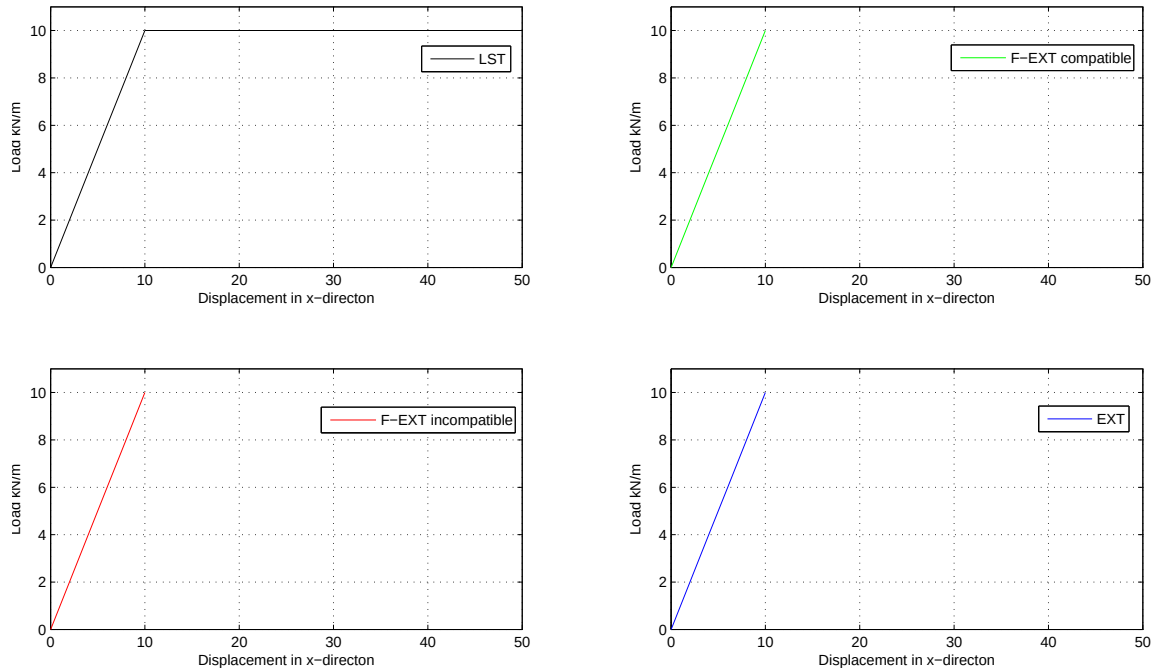

Figure 6.3: The results for the plane stress patch test using the Full Newton-Raphson scheme.

6.1.1 The gradients influence on convergence

A closer look at the geometry and mesh of the patch test reveals that each element is rather large compared to the size of the entire geometry. The constraints are only applied to the translational d.o.f. which means that the gradients on the constrained side of the patch is free to move, see Figure 6.4.

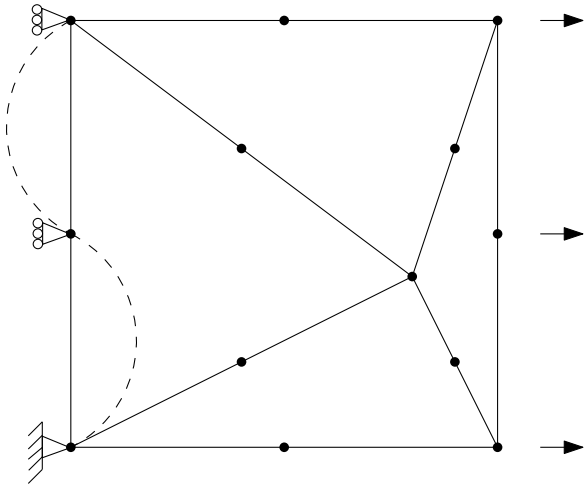

Figure 6.4: The gradients are free to move along the boundary of the geometry.

Because the shape functions for the gradients depend on the length of the elements sides, the size of the elements effect the accuracy of the solution. A mesh refinement of the patch test, as seen in Figure 6.5 will clarify if gradients in fact disrupt the convergence of the F-EXT element.

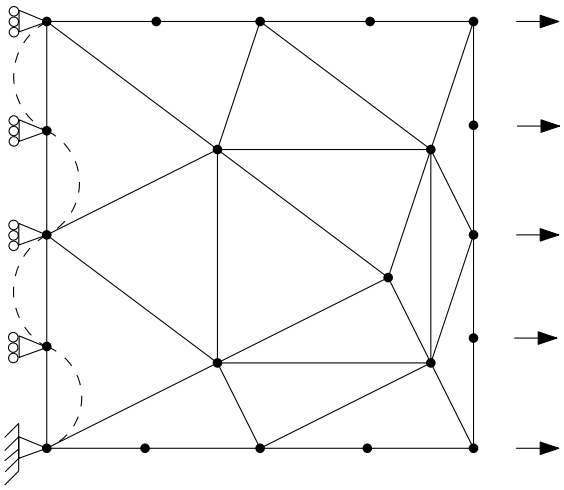

Figure 6.5: The effect of the gradients will be smaller when refining the mesh. $u = 50$, $E = 1$, $\nu = 0.3$ and $y0 = 1$.

The gradients depend on a smaller element, and will be equally smaller, as shown in Figure 6.5. This means that the solution is now converging for F-EXT compatible after the elements starts yielding. The results for the refined mesh of the patch, for Modified

and Full Newton-Raphson schemes, are shown in Figure 6.6 and Figure 6.7, respectively.

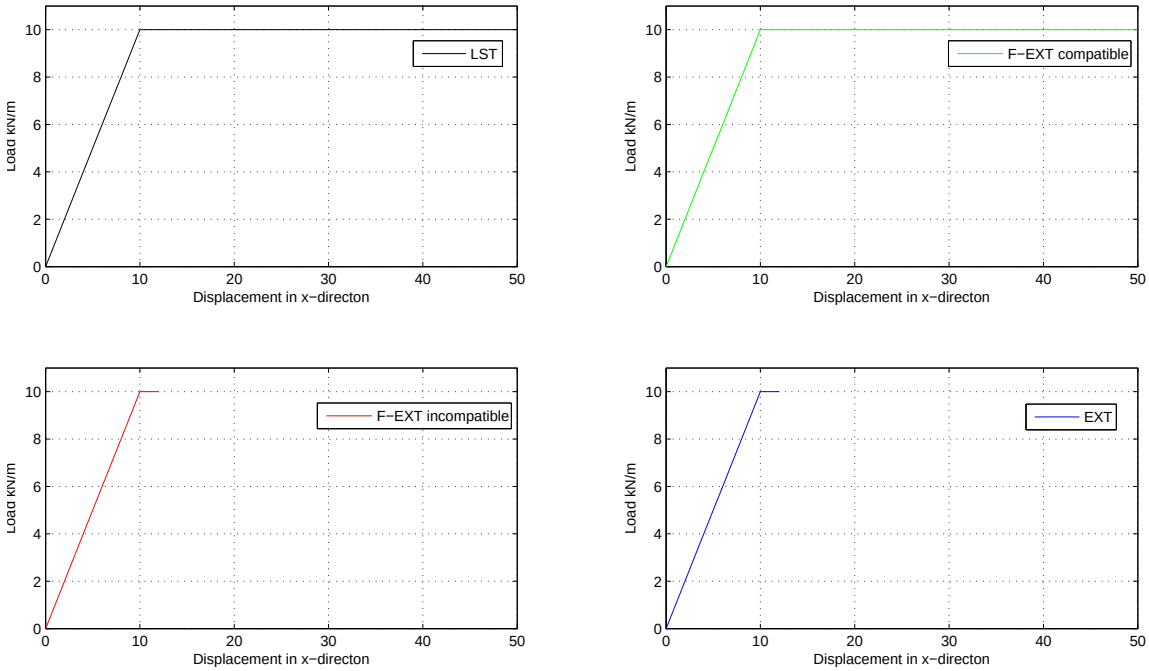

Figure 6.6: The results for the patch test of plane stress with the refined mesh, using the Modified Newton Raphson scheme.

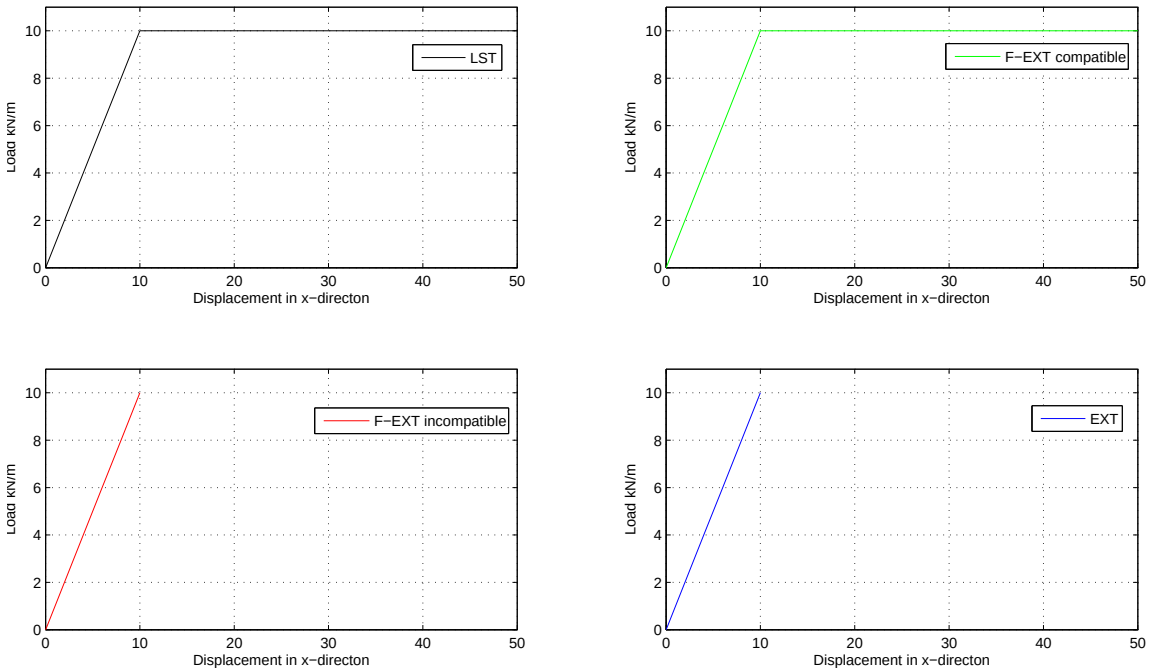

Figure 6.7: The results for the patch test of plane stress with the refined mesh, using the Full Newton Raphson scheme.

From the results, it is clear that EXT and F-EXT incompatible are unable to converge for the Full and Modified Newton-Raphson schemes. A closer look at where the program breaks, shows that the problem lies in updating the stiffness matrix after the elements yield. This is confirmed by running the same patch test, but with use of the Initial Stiffness Method. Here, the solution converges, see Figure 6.8.

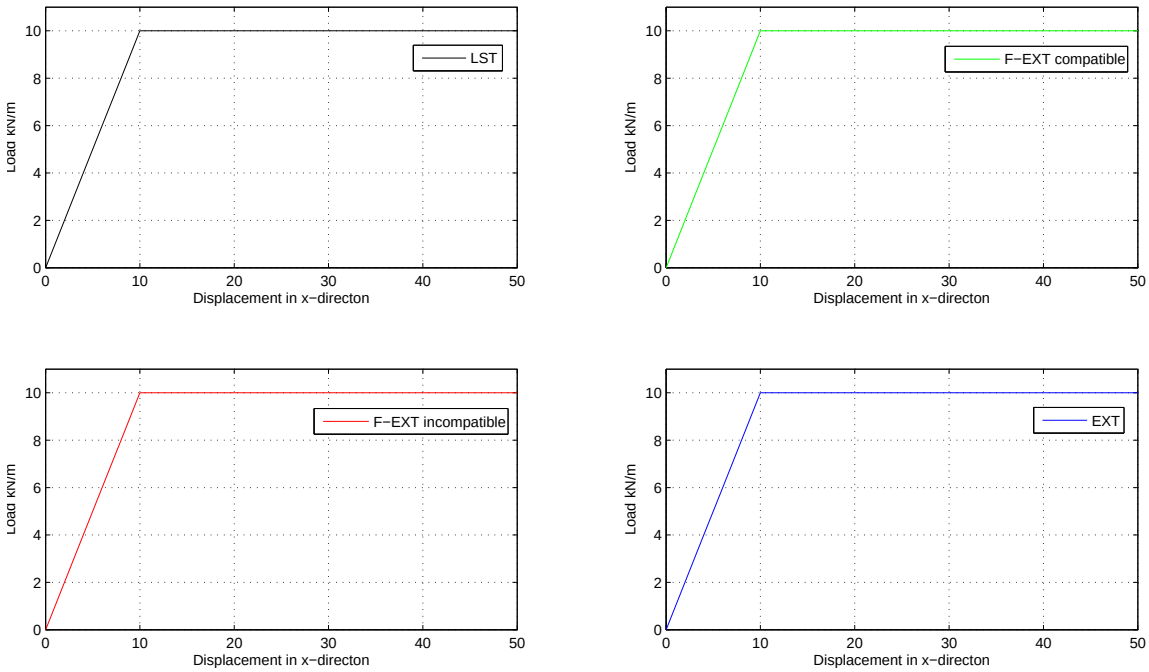

Figure 6.8: The results for the patch test of plane stress with the refined mesh, using the Initial Stiffness Method.

The results for the Initial Stiffness Method, which is converging, the Modified and the Full Newton-Raphson schemes indicates that the problem appears when the stiffness matrices are updated.

G. De Roeck et al. [12] mentions the phenomenon of singular stiffness matrices. This can arise in the case of a perfectly plastic analysis, where two adjacent elements are in a state of yielding. To test if the convergence problems are due to the state of perfect plasticity, a small hardening parameter is implemented in the following subsection.

6.1.2 Implementing a hardening parameter

As seen in the previous subsection, the EXT and F-EXT incompatible elements are unable to converge for the simple patch test. The convergence difficulties appear when the stiffness matrices are updated in the plastic solution. The tangent stiffness matrices becomes singular when the elements reaches a state of perfect plasticity.

Therefore, it can be an advantage to introduce a small hardening parameter, to ensure that the elements never acts fully perfectly plastic.

The geometry, mesh and boundary conditions are the same as used before for the patch test with the refined mesh, see Figure 6.5. A range of hardening and softening parameters are applied, and the results are plotted in Figure 6.9.

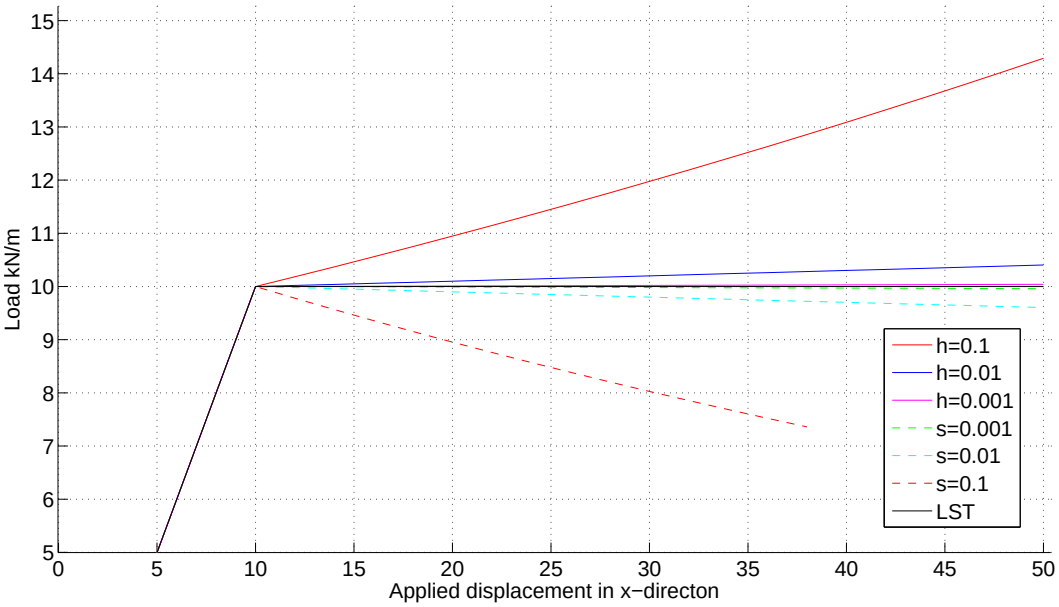

Figure 6.9: The patch test with different hardening (h) and softening (s) parameters.

As seen in Figure 6.9, the patch test is passed for a wide range of hardening parameters. It is also seen that adding a softening parameter is only valid for very small values of softening.

6.1.3 Conclusion on plane stress patch test

The EXT and the F-EXT incompatible elements are not able to converge for a plane stress patch test. The problem encounters after the first update of the stiffness matrix when the elements are yielding.

It is illustrated by adding different hardening parameters, that the convergence problem might only be for perfectly-plastic elements. For plane stress, the state of perfect plasticity is reached in the instance the elements of the patch starts to yield. For plane strain, however, perfect plasticity does not happen at the first yielding point.

Therefore, the case of plain strain for the patch is examined in the following section.

6.2 Plane strain

In the case of plane strain, the load-displacement curve is increasing after the first yielding is encountered. The increase continues until the curve reach a point where it becomes flat.

This is because the magnitude of the normal stresses, σ_x and σ_z, increases until a constant value is attained. During this, the effective stress, σ_e, which is a function of the three normal stresses, remains constant.

As seen in the previous section, the EXT and the F-EXT incompatible elements are unable to converge for a perfectly plastic state. As described, this state does not encounter at the first yielding point for the case of plane strain. Therefore, it is examined if the elements are able to converge for plane strain, without adding any hardening parameters.

The refined mesh is used, see Figure 6.5. As seen on Figure 6.10, the elements do converge for the Full Newton-Raphson scheme. Identical results are obtained for the Initial Stiffness Method and the Modified Newton-Raphson scheme.

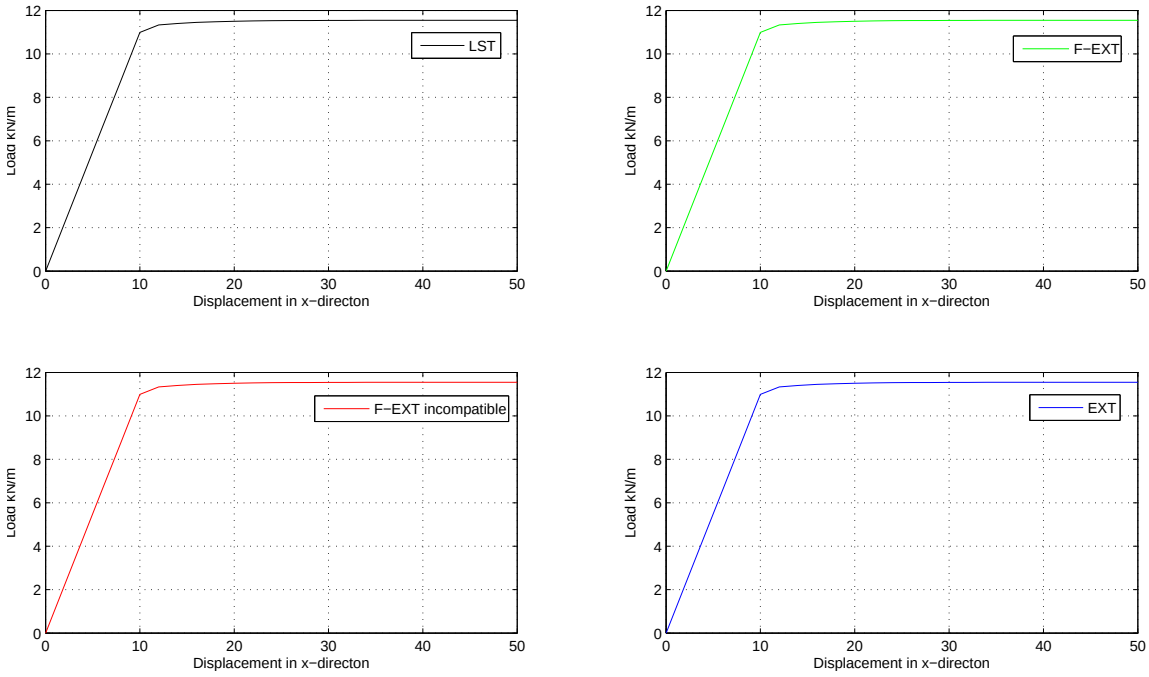

Figure 6.10: The results for the patch test of plane strain.

Because the elements are sensitive to the update of the stiffness matrix in the iteration scheme, it is interesting to examine what happens to the eigenvalues for the stiffness matrix during the increase on the load/displacement curve, as shown in Figure 6.11.

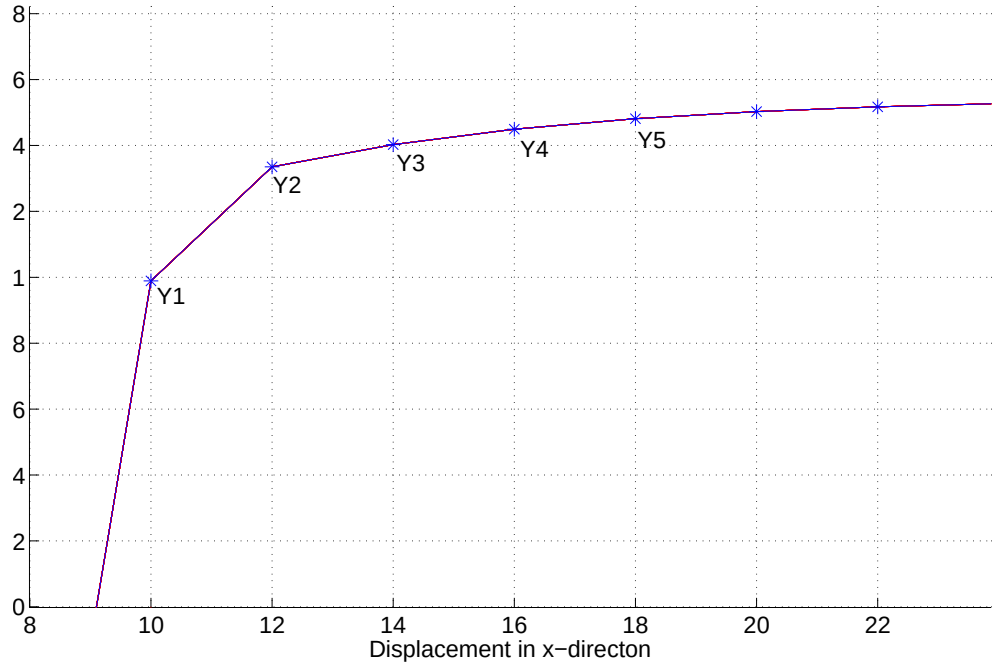

Figure 6.11: The EXT results for the patch test of plane strain, close up.

The eigenvalues for the points marked Y1-5 are given in Table 6.1. It is clear that the number of zero-values is not increasing, but the lowest eigenvalues are approaching zero.

Table 6.1: Eigenvalues for element 16 (see Figure 6.12) in the patch test of the extended element.

Y1	Y2	Y3	Y4	Y5
15.7900	15.5364	15.4015	15.2915	15.2020
10.2008	10.0422	9.9609	9.8942	9.8397
5.0764	4.9837	4.9667	4.9536	4.9434
4.3939	4.3244	4.2982	4.2765	4.2587
3.2393	3.2020	3.1949	3.1892	3.1846
2.6842	2.6663	2.6639	2.6622	2.6610
2.0071	1.9625	1.9503	1.9406	1.9330
1.5114	1.4618	1.4451	1.4321	1.4220
0.9842	0.9539	0.9469	0.9415	0.9374
0.4660	0.4486	0.4428	0.4384	0.4351
0.3347	0.3251	0.3229	0.3213	0.3201
0.3053	0.2980	0.2971	0.2966	0.2963
0.0244	0.0163	0.0111	0.0075	0.0050
0.0161	0.0107	0.0072	0.0049	0.0032
0.0083	0.0057	0.0039	0.0027	0.0018
0.0060	0.0041	0.0028	0.0019	0.0013
0.0008	0.0006	0.0004	0.0003	0.0002
0.0000	0.0000	0.0000	0.0000	0.0000
0.0000	0.0000	0.0000	0.0000	0.0000
0.0000	0.0000	0.0000	0.0000	0.0000

Thus, it is investigated why some of the eigenvalues are approaching zero-values.

6.2.1 The influence of residal forces on the global solution

W. Pan et al. comments on the on sub-modelling:

> "In theory the approach can be applied generally to non-linear problems. In practice, however, the sub-modelling approach cannot be used in cases where the local non-linear response of the sub-model, not included in the global model, even mildly affects the global model response." [23]

This means that the local respons, in this case the residual forces in the condensed d.o.f., must not influence the global solution. Thus it is investigated if the residual force vector for the condensed d.o.f., Fr_c, is large enough to have an impact on the global solution. In Table 6.2 the residual force vector for element 16, shown in Figure 6.12, is given for the loadstep marked Y5 in Figure 6.11.

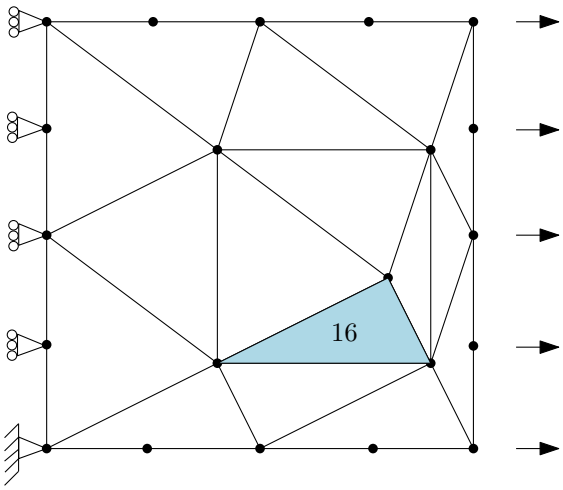

Figure 6.12: The geometry, mesh and boundary conditions for the patch test, with element 16 marked.

Table 6.2: Residual forces for element 16 in the plane strain patch test of the extended element.

Displacements in corner nodes - retained d.o.f.				
	Iteraion 1	Iteraion 2	Iteration 3	Iteration 5
Fr_1	0.382709218334343	0.416181125550998	0.383825524396519	0.383429652246723
Fr_2	0.000000027732312	0.017175053915695	0.000205490664015	0.000000027248940
Fr_3	-0.382709218334056	-0.416181125550684	-0.383825524396232	-0.383429652246438
Fr_4	0.000000110929248	0.068700215662733	0.000821962656062	0.000000108995768
Fr_5	-0.000000000000313	-0.000000000000335	-0.000000000000317	-0.000000000000314
Fr_6	-0.000000138661524	-0.085875269578398	-0.001027453320043	-0.000000136244677
Displacements in midside nodes - retained d.o.f.				
	Iteraion 1	Iteraion 2	Iteration 3	Iteration 5
Fr_7	0.000000000001191	0.000000000001297	0.000000000001197	0.000000000001195
Fr_8	0.000000554646183	0.343501078313660	0.004109813280247	0.000000544978776
Fr_9	-1.530836873337319	-1.664724502203947	-1.535302097586027	-1.533718608986840
Fr_{10}	-0.000000110929258	-0.068700215662796	-0.000821962656075	-0.000000108995782
Fr_{11}	1.530836873336146	1.664724502202676	1.535302097584847	1.533718608985681
Fr_{12}	-0.000000443716923	-0.274800862650882	-0.003287850624172	-0.000000435983029
Gradients in midside nodes - condensed d.o.f.				
	Iteraion 1	Iteraion 2	Iteration 3	Iteration 5
Fr_{13}	0.000000000000000	-0.000000000000003	0.000000000000006	-0.000000000000002
Fr_{14}	-0.000000000000002	-0.000000000000001	-0.000000000000015	0.000000000000008
Fr_{15}	-0.000000000000002	-0.000000000000000	-0.000000000000004	0.000000000000003
Fr_{16}	-0.000000000000002	-0.000000000000004	-0.000000000000001	-0.000000000000001
Fr_{17}	-0.000000000000004	-0.000000000000002	0.000000000000003	-0.000000000000006
Fr_{18}	0.000000000000022	0.000000000000003	0.000000000000012	-0.000000000000001
Displacements in middle node - condensed d.o.f.				
	Iteraion 1	Iteraion 2	Iteration 3	Iteration 5
Fr_{19}	0.000000000000007	-0.000000000000005	0.000000000000014	-0.000000000000007
Fr_{20}	-0.000000000000037	-0.000000000000011	-0.000000000000034	0.000000000000004

It is seen that Fr_c reaches a value of almost zeros when the loadstep has converged. The residual force vector for element 16 in the case of plane stress is quite different, see Table 6.3. At yielding point Fr_c has a small value, but as the stiffness matrix is updated for each iteration, the values for the gradients increase significantly and thereby impacts the global solution.

Table 6.3: Residual forces for element 16 in the plane stress patch test of the extended element.

Displacements in corner nodes - retained d.o.f.				
	Iteraion 1	Iteraion 2	Iteration 3	Iteration 5
Fr_1	0.333333333334481	0.339269471270347	-0.052487347744191	0.055916273800580
Fr_2	0.000000000000000	0.006103835769673	0.009513595277478	-0.046087149445755
Fr_3	-0.333333333334219	-0.339269471270080	0.048988457704825	-0.100312162759481
Fr_4	-0.000000000000001	0.024415343078670	0.104097746148590	-0.227624883186249
Fr_5	-0.000000000000261	-0.000000000000266	0.005971395231174	-0.048109177507434
Fr_6	-0.000000000000000	-0.030519178848343	-0.028331290229273	-0.025463331989333
Displacements in midside nodes - retained d.o.f.				
	Iteraion 1	Iteraion 2	Iteration 3	Iteration 5
Fr_7	0.000000000001040	0.000000000001058	0.015441680502742	-0.083505721740749
Fr_8	-0.000000000000001	0.122076715393374	0.137502862798224	-0.228351316011182
Fr_9	-1.333333333337913	-1.357077885081373	-1.183518536206551	1.149609545086807
Fr_{10}	0.000000000000002	-0.024415343078688	-0.126019286412382	0.501245973275580
Fr_{11}	1.333333333336871	1.357077885080312	1.326832021759944	-1.257189737149031
Fr_{12}	-0.000000000000001	-0.097661372314685	-0.053046483915117	0.117031235746863
Gradients in midside nodes - condensed d.o.f.				
	Iteraion 1	Iteraion 2	Iteration 3	Iteration 5
Fr_{13}	-0.000000000000000	-0.000000000000008	1.168595782212472	-1.257995027840322
Fr_{14}	0.000000000000001	0.000000000000001	-0.089957765959764	0.299613305903213
Fr_{15}	0.000000000000000	0.000000000000001	0.092491869399998	-0.159911049481703
Fr_{16}	-0.000000000000002	0.000000000000000	-0.069141338725196	-0.088289224558179
Fr_{17}	0.000000000000000	0.000000000000005	0.078164173535174	-0.053932767911452
Fr_{18}	0.000000000000000	-0.000000000000000	-0.006290459928105	0.041039836290726
Displacements in middle node - condensed d.o.f.				
	Iteraion 1	Iteraion 2	Iteration 3	Iteration 5
Fr_{19}	0.000000000000001	0.000000000000004	-0.161227671247944	0.283590980269307
Fr_{20}	0.000000000000001	-0.000000000000001	-0.043717143667520	-0.090750528389924

6.2.2 Conclusion on plane strain patch test

Since EXT and F-EXT incompatible shows good results for the case of plane strain, the elements are tested in an example of a strip footing. This will show if the elements can be used in other applications where plane strain is assumed.

6.3 Strip footing with von Mises yield criteria

In this section tests are carried out for the case of a strip footing, in order to examine the performance of the EXT element with a small hardening parameter introduced.

The strip footing has a width of b = 1 m and the length is assumed to be infinite in relation to the width. The soil layer is assumed to be weigthless and is modelled as an elastic-perfectly plastic material satisfying the von Mises yield criteria [8]. The material constants used in the tests is, $E = 10^7$ kPa, $nu = 0.48$, $y_0 = 848.7$ kPa.

Due to the infinite length of the footing the tests is solved for a plane strain state. Due to the symmetry only half of the soil layer is discretized into a finite element mesh. The boundaries of the mesh are sufficiently far from the footing, extending 4.5 m horizontally and 5 m vertically. The finite element model for the coarse mesh is shown in Figure 6.13, whereas the two finer mesh are shown in Appendix D.

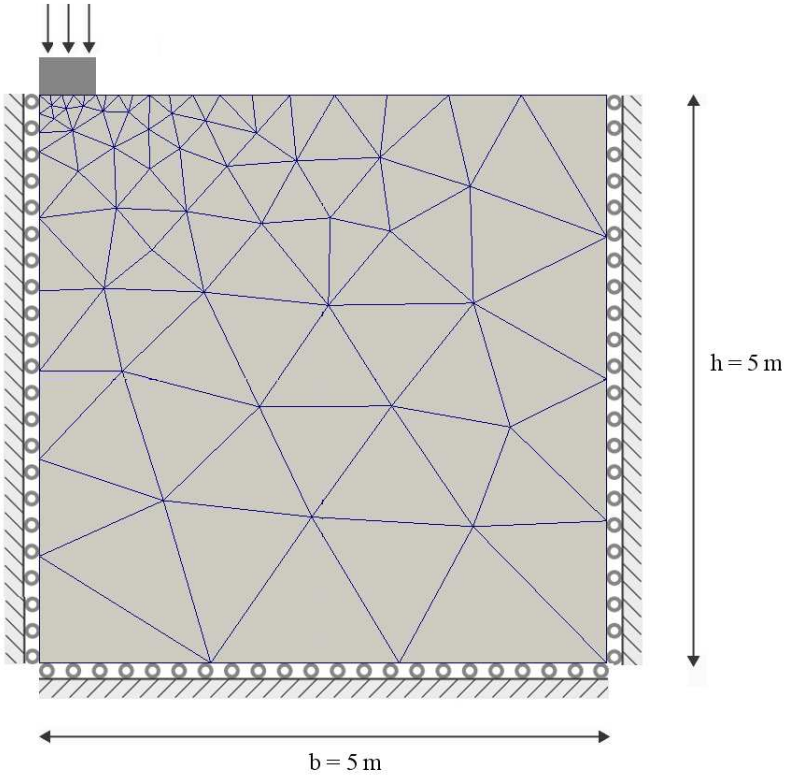

Figure 6.13: Geometry and boundary conditions for strip footing.

The footing is considered to be rigid and smooth, i.e. there is no friction at the footing/soil interface. The settlement of the footing is then simulated by applying a uniform vertical displacement of $u = 0.002\,m$ in increments to the nodes loacted at the top of the interface elements. The load bearing capacity is then computed by summing up the vertical reaction at the nodes, which have been subjected to displacements. The sum reaction at the nodes is divided by the width.

A theoretical solution of the bearing capacity have been derived by Prandtl and Hill [8]. They give the following equation for the bearing capacity in the case of a frictionless footing/soil interface:

$$P_{lim} = (2 + \pi)c \approx 5.14c \approx 2.97\sigma_y \tag{6.1}$$

where the cohesion of the soil is given by $c = \sigma_y/\sqrt{3}$ for the von Mises yield criteria.

The bearing capacity for the first mesh, computed in the finite element program, is plotted in Figure 6.14 as a function of the settlement. The bearing capacity found by the other two mesh can be seen in Appendix D.

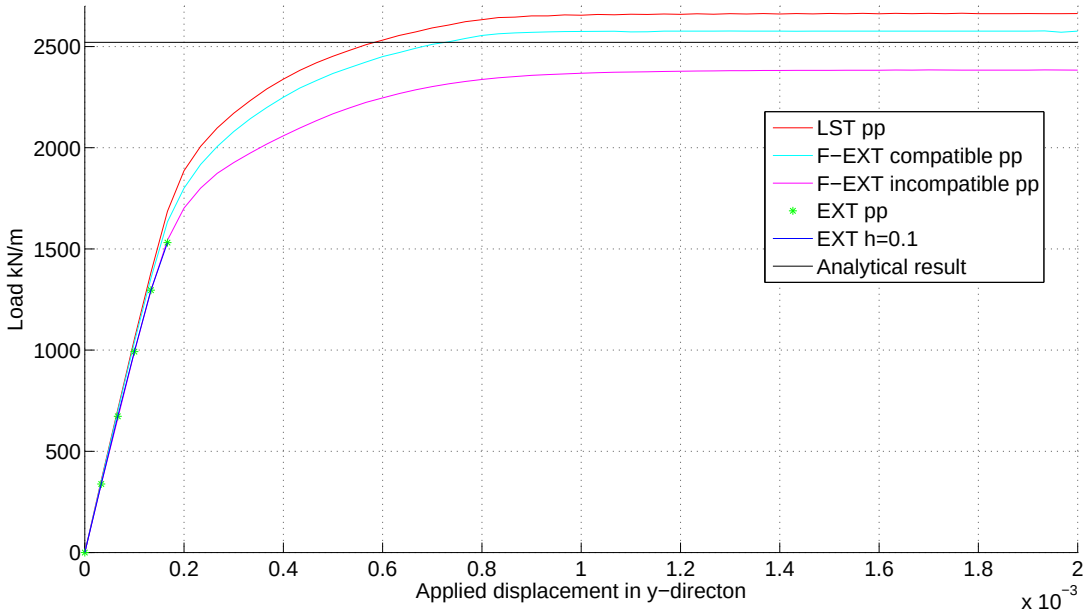

Figure 6.14: Settlement of a strip footing with pp indicating perfect plasticity and h=0.1 indicating a hardening parameter.

As seen on the figures, the EXT element does not converge towards the exact solution. This can be due to the residual force in the gradients, which might not be going towards zero in a test with a load acting on only some of the top boundary line, while the other boundarys are restrained in some way.

A hardening parameter has also been implemented, but this does not help the EXT element to converge.

It should be noted that the F-EXT incompatible element does not overestimate the bearing capacity of the soil, while LST and F-EXT compatible is on the unsafe side. This indicates that the F-EXT incompatible element is better suited to soil-structure interaction analysis than the LST and F-EXT compatible elements. Further investigation of this is done in Chapter 9, where Mohr-Coulombs yield criteria is used, as it is more appropriate for geotechnical problems.

If the EXT element had been able to converge in the analysis of the strip footing performed in this section, the results would be similar to F-EXT incompatible and thereby not overestimating the bearing capacity.

In the next section, a test of the patch is performed again to verify that the EXT element is unable to converge for plane strain, when an unsymmetrically applied displacement.

6.3.1 Test with an unsymmetrically applied displacement

The patch with the refined mesh is submitted to the boundary conditions shown in Figure 6.15. The displacements are applied to only half of the patchs' height, while the

constraints remain the same as previous.

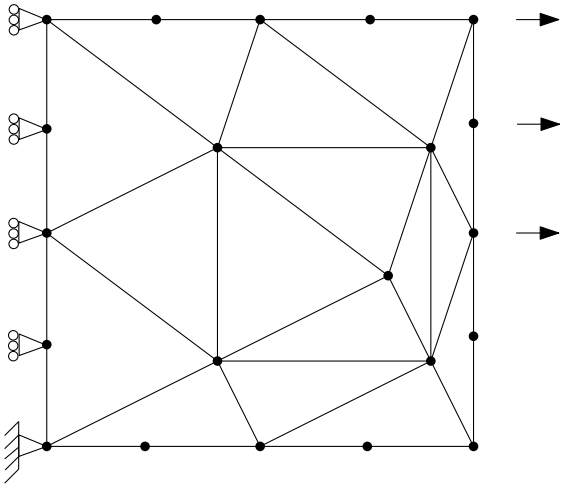

Figure 6.15: The patch with an unsymmetrically applied displacement of $u = 50$. The material parameters are $E = 1$, $\nu = 0.3$ and $y0 = 1$.

The results for the different element types are shown in Figure 6.16, from which it is clear that EXT does not converge.

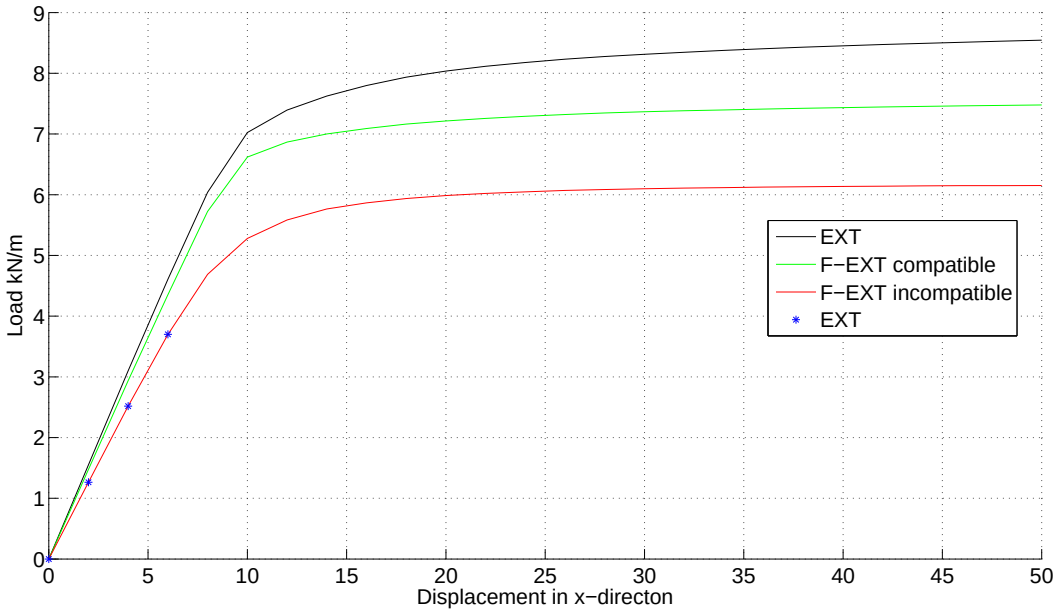

Figure 6.16: Load-displacement curve for the test with the unsymmetrically applied displacement.

The residual force vectors for the first four iterations of the loadstep, for which the element does not converge, are shown in Table 6.4. As seen in the table, the residual force vector is subjected to a small value in the condensated d.o.f. The values of the vector shifts

between the shown values from iteration to iteration until the limit of maximum iterations is reached.

Table 6.4: Residual forces for element 16 in the plane strain patch test with the unsymmetrically applied displacement.

Displacements in corner nodes - retained d.o.f.				
	Iteraion 1	Iteraion 2	Iteration 3	Iteration 4
Fr_1	0.056001916971212	0.075017196543187	0.068398477213653	0.068192809890429
Fr_2	0.011214321470858	0.015008542479844	0.013856735778070	0.013824306141399
Fr_3	0.179570835619354	0.239262465811755	0.253380761671432	0.252557191510664
Fr_4	0.019740501452271	0.026076289706092	0.023928771718140	0.024555499983120
Fr_5	-0.079635982519485	-0.106339251431946	-0.105572155188004	-0.104441523103936
Fr_6	0.040975585208491	0.054742979589391	0.055315992275102	0.055439550254920
Displacements in midside nodes - retained d.o.f.				
	Iteraion 1	Iteraion 2	Iteration 3	Iteration 4
Fr_7	0.189859081609423	0.254287422306575	0.238798517914633	0.237537964313874
Fr_8	0.178891811718250	0.238194074005424	0.243423013678773	0.243335803450497
Fr_9	-0.597992128474481	-0.799501876427534	-0.767605358192722	-0.766569982373887
Fr_{10}	-0.285303101764242	-0.380680446573383	-0.377026498790213	-0.376517751488201
Fr_{11}	0.252196276793974	0.337274043197965	0.312599756581006	0.312723539762856
Fr_{12}	0.034480881914395	0.046658560792630	0.040501985340154	0.039362591658261
Gradients in midside nodes - condensed d.o.f.				
	Iteraion 1	Iteraion 2	Iteration 3	Iteration 4
Fr_{13}	0.000000000000006	-0.000000000000000	0.000000000000006	-0.000000000000000
Fr_{14}	-0.000000000000018	0.000000000000001	-0.000000000000017	-0.000000000000001
Fr_{15}	-0.000000000000001	0.000000000000000	-0.000000000000001	0.000000000000001
Fr_{16}	-0.000000000000002	0.000000000000001	-0.000000000000002	0.000000000000000
Fr_{17}	0.000000000000002	0.000000000000000	0.000000000000002	0.000000000000001
Fr_{18}	-0.000000000000001	-0.000000000000002	0.000000000000004	0.041039836290726
Displacements in middle node - condensed d.o.f.				
	Iteraion 1	Iteraion 2	Iteration 3	Iteration 4
Fr_{19}	0.000000000000002	-0.000000000000001	0.000000000000002	-0.000000000000005
Fr_{19}	-0.000000000000022	0.000000000000003	-0.000000000000026	-0.000000000000001

6.4 Conclusion on tests with von Mises yield criteria

In the present chapter, a varied range of tests have been performed on the different element types used in this thesis. The tests involves perfect plasticity, hardening and softening parameters, plane stress and plane strain, subjected to both uniformly and asymmetrical distributed displacements.

As described in the foregoing sections, the EXT element is unable to converge when the stiffness matrices are updated in a nonlinear analysis. When two adjacent elements are in a state of perfect plasticity yielding, the stiffness matrices becomes singular which makes it impossible to solve the governing equations.

Furthermore, when the residual forces in the condensed d.o.f. have an impact on the global solution, it is hard for the extended elements to converge. It is evident that some effort should be made to overcome these difficulties.

A solution method could be to add a small hardening parameter in order to prevent the state of perfect plasticity. The results for the plane stress patch test are good. But the hardening parameter is not able to solve the convergence difficulties in the plane strain example of a strip footing. Thus, adding a hardening parameter does not mean that the

element is able to converge for all cases. The outcome varies from case to case, and the solution method should be tested thoroughly.

The litterature reports on combining nonlinearity and substructuring, with the conclusion that nonlinear parts of a structure must be regarded as a single substructure, while the linear parts may be described with one or more substructures [11], [12], [20]. The substructuring is a special case of static condensation, where the element itself is the substructure.

> "The part of (the) structure which is known to remain elastic during the loading process is defined as either one or several substructures, while the part of the structure which undergoes plastic deformation is defined as one nonlinear substructure." Han & Abel, [22].

Other articles mentions that the nonlinear parts of a structure must remain in isolated regionsand those regions are defined as separate substructures [13], [7].

Because every EXT element is a substructure in itself, the statements above is obviously not met. Sheu Chyi-Horng et al. [21] describes how multilevel substructuring can be used in fully nonlinear problems. However, this method does not apply here, as it would require almost as many levels as elements used, due to the status of a single EXT element as a substructure.

W. Pan et al. has developed an iterative substructure method, which can be used for elastic-plastic analysis [23]. The conclusion is, however, that the interface nodes between the substructures must not be too close to the nonlinear regions.

Clearly the proposed method of substructuring does not apply to the single-element substructuring used in this thesis. This is due to, as previously stated, every element in an analysis is a substructure by itself and therefore it is impossible to keep the nonlinear regions (elements) distant from the global nodes of an adjacent element.

It is evident that some effort should be made to overcome these difficulties. A solution could be to only condensate non-yielding elements, as done in [2]. This is examined in the following chapter.

7 Condensation of non-yielding elements

Several articles and litterature suggests that static condensation, or substructuring, should only be applied for the linear domains in a non-linear analysis. In an analysis it is sought to treat all elements in a mesh as EXT elements untill an element starts to yield. When this happens, the program should change the element type for that particular element to F-EXT, i.e. the same element but without condensation of the gradients and the translations in the center node. By applying this to the program, the advantages of few d.o.f. and the accuracy of many d.o.f. should be maintained.

7.1 Patch test

The same patch test with the refined mesh, as used previously, is performed in order to validate the results. To control which elements are yielding, a yield criteria of $y0 = 100$ is applied to all elements but one. The last element, element 16, is given a yield criteria of $y0 = 1$. This means that element 16 will start to yield and the rest of the elements will remain elastic. In Figure 7.1 the geometry, mesh, boundary conditions and element 16 is depicted.

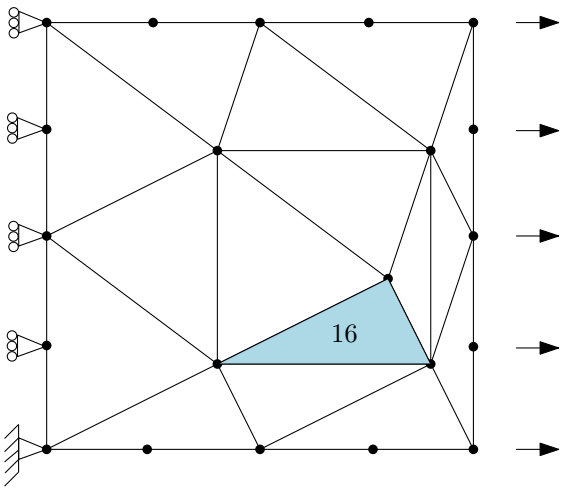

Figure 7.1: The geometry, mesh and boundary conditions for the patch test.

Running the patch test shows that the solution method of only condensating the elastic elements are not resulting in convergence, see Figure 7.2. This may be a consequence of the assemblage of the elements into global matrices and vectors. When element 16 starts to yield, the residual force vector of the element is applied to the global residual force vector.

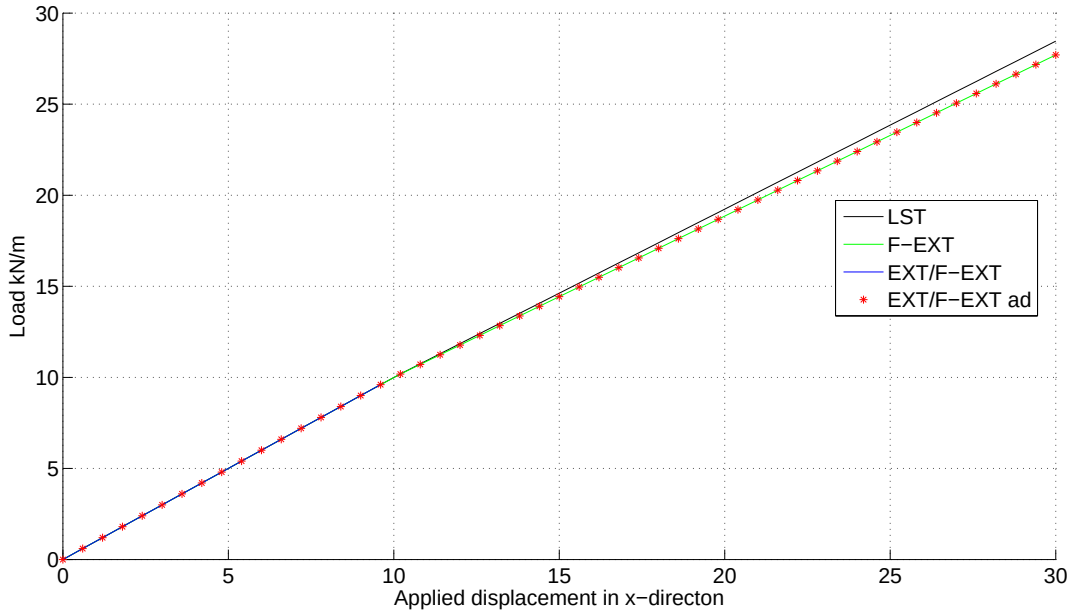

Figure 7.2: Results for patch test, where 'ad' indicates that the adjacent elements to element 16 is also treated as F-EXT elements.

But for the adjacent elements, shown on Figure 7.3, the local residual forces are condensated and represented through the 12 remaining d.o.f because these elements are elastic. When an element is unpacked, the displacements for the 8 condensated d.o.f. are calculated without taking the residual forces from element 16 into account.

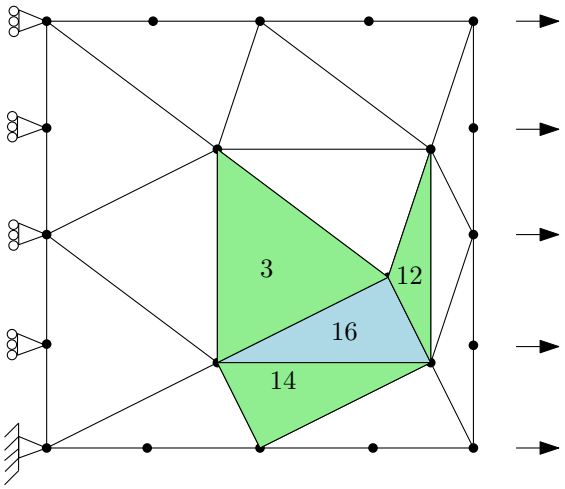

Figure 7.3: The geometry, mesh and boundary conditions for the patch test.

This problem is corrected by treating the adjacent elements to element 16 as F-EXT elements, i.e. not condensating the elements, but remain a yield criteria of $y0 = 100$. The patch test is performed with this small correction to the program, resulting in a converging solution, as indicated with red in Figure 7.2.

Furthermore, it is investigated if this change in the program is also able to converge if two adjacent elements are yielding. The mesh, boundary conditions, yielding elements and new adjacent elements are shown on Figure 7.4.

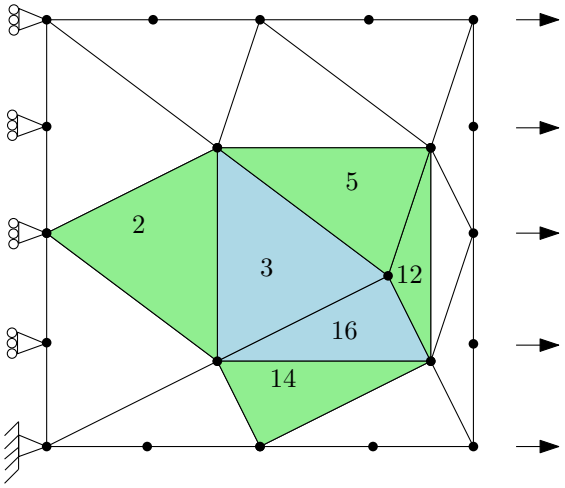

Figure 7.4: The geometry, mesh and boundary conditions for the patch test.

The test with two adjacent elements in a state of perfect plasticity shows that the solution is able to converge. Compared to results obtained with a full mesh of F-EXT elements, shown in Figure 7.5, it is clear that the results are coherent with each other. This means that the proposed method of only condensating the non-yielding elements provides a valid solution.

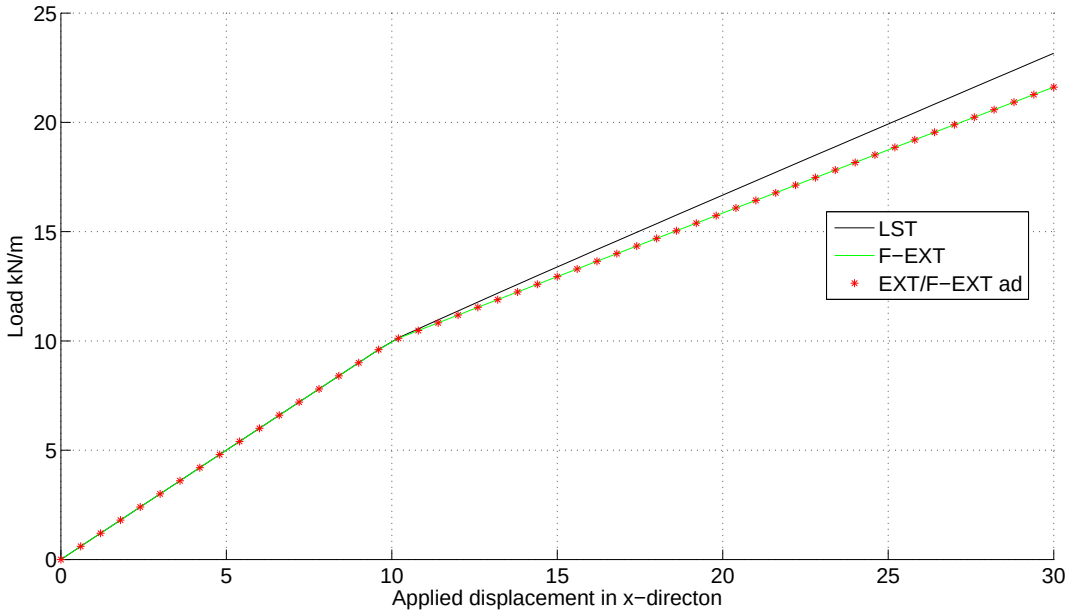

Figure 7.5: Results for patch test, where 'ad' indicates that the adjacent elements to element 16 is also treated as F-EXT elements.

Another important feature of this method is that it allows the program to only update the elements that are in fact yielding, and thereby saving a considerable amount of recalculations, condensations and unpacking of elements.

7.1.1 Conclusion

Obviously, it is difficult to identify, which elements that are yielding, in order to regard them as F-EXT incompatible elements instead of EXT elements. This requires extensive computations, where the yielding elements are identified. A. Hadoush and A. H. van den Boogaard has developed such a procedure, see [2].

Eventhough the EXT element is not able to converge for the tests performed in the previous chapter, it is possible to predict the outcome of nonlinear tests by using the F-EXT incompatible element.

Therefore it can still be investigated if EXT would give more accurate results and not overestimate the bearing capacity for geotechnical problems. In the following chapter the Mohr-Coulomb material model is presented and implemented in the nonlinear finite element program, in order to investigate how the EXT element should work when this is applied in geotechnical problems.

In the subsequent chapter, the bearing capacities of a strip footing resting on three different soil layers is determined for F-EXT incompatibel and LST, and compared to analytical solutions.

8 Mohr-Coulomb yield criteria

In the following chapter the Mohr-Coulomb yield criteria is presented. For many years this yield criteria has been the basis in the calculations of geotechnicals problems. The Mohr-Coulomb criteria is implemented in the nonlinear finite element code, so that tests of the F-EXT incompatible element can be carried out for different geotechnical problems.

When working with the Mohr-Coulomb yield criteria, there are two cases to consider: the associated plasticity case (f=g=0), and the non-associated plasticity case (f=0, g≠0). In this chapter both cases will be discussed, but the main focus will be on the non-associated plasticity.

8.1 Implementation of the Mohr-Coulomb criteria

In principal stress space the Mohr-Coulomb yield criteria is usually described by:

$$f(\bar{\sigma}) = (\sigma_1 - \sigma_3) + (\sigma_1 + \sigma_3)\sin\varphi - 2\,c\,cos\varphi \tag{8.1}$$

where φ is the angle of friction and c is the cohesion. If the principal stresses are arranged according to Eq. 8.2 the yield criterion forms a triangular plane.

$$\sigma_1 \geq \sigma_2 \geq \sigma_3 \tag{8.2}$$

If the interrelationship between the principal stresses changes, so must the equation. This imply that the yield criteria contains six equations, all on the form of Eq. 8.1. In the principal stress space these equations forms an irregular hexagonal pyramid with the apex located in $\sigma_1 = \sigma_2 = \sigma_3 = c\cot\varphi$, see Figure 8.1.

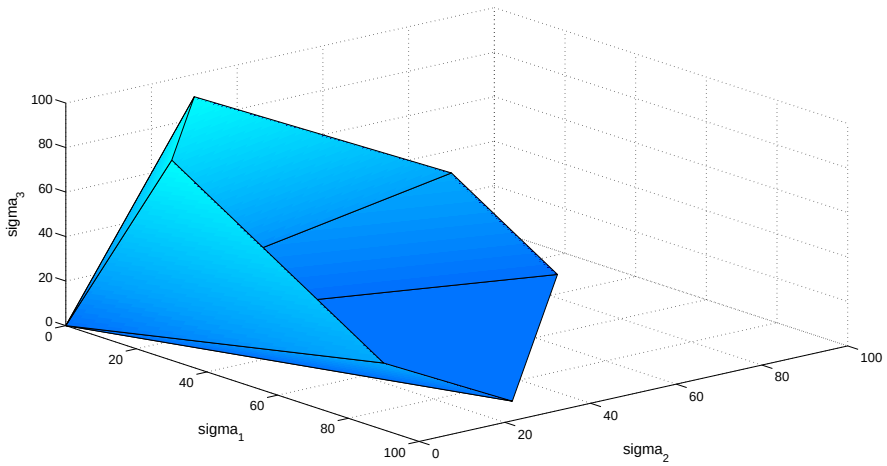

Figure 8.1: Graphical representation the Mohr-Coulomb criteria, $\varphi = 30$ $c = 0$.

8.1.1 Associated flow rule

In a yield criteria where an associated flow rule applies, the plastic potential is equal to the yield plane, ($f = g = 0$). An associated flow rule for the Mohr-Coulomb criteria indicates that the dilatation angle is equal to the friction angle ($\varphi = \psi$), and that the cohesion is zero, see Eq. 8.3 and Eq. 8.4.

8.1.2 Non-associated flow rule

With a non-associated flow rule, the plastic potential is not equal to the yield criteria, ($f \neq g$). For a Mohr-Coulomb material f and g are given by:

$$f = \sigma_1 - \sigma_3 + (\sigma_1 + \sigma_3)\sin\varphi - 2c\,\cos\varphi = 0 \tag{8.3}$$

$$g = \sigma_1 - \sigma_3 + (\sigma_1 + \sigma_3)\sin\psi \tag{8.4}$$

where φ is the angle of friction, c is the cohesion and ψ is the dilatation angle. As seen in the equations, the angle of friction and the cohesion of the soil material is included in the yield criteria, whereas the dilataion angle is the only material property influencing the plastic potential.

For computational purposes the equations for the yield plane, Eq. 8.3, and the plastic potential, Eq. 8.6, are rewritten:

$$f(\bar{\sigma}) = \bar{a}_1^T\,(\bar{\sigma} - \bar{\sigma}_a) = k\sigma_1 - \sigma_3 - \sigma_c = 0 \tag{8.5}$$

$$g(\bar{\sigma}) = \bar{b}_1^T\,(\bar{\sigma}) = m\sigma_1 + \sigma_3 \tag{8.6}$$

where $\bar{a}_1$ and $\bar{b}_1$ are gradients of the yield plane and plastic potential, respectively.

$$\bar{a} = \frac{\partial f}{\partial \bar{\sigma}} = \begin{Bmatrix} k \\ 0 \\ -1 \end{Bmatrix}, \quad k = \frac{1+\sin\varphi}{1-\sin\varphi} \tag{8.7}$$

$$\bar{b} = \frac{\partial g}{\partial \bar{\sigma}} = \begin{Bmatrix} m \\ 0 \\ -1 \end{Bmatrix}, \quad m = \frac{1+\sin\psi}{1-\sin\psi} \tag{8.8}$$

σ_c is the uniaxial strength and $\bar{\sigma}_a$ is the apex point of the criteria:

$$\sigma_c = 2\,c\,\sqrt{k} \tag{8.9}$$

$$\bar{\sigma}_a = \frac{\sigma_c}{k-1}\begin{Bmatrix} 1 \\ 1 \\ 1 \end{Bmatrix} \tag{8.10}$$

Eq. 8.5 describes a triangular plane in the principal stress space, when the stresses are arranged according to $\sigma_1 \geq \sigma_2 \geq \sigma_3$, as shown in Figure 8.2. Likewise for other arrangements of the stresses.

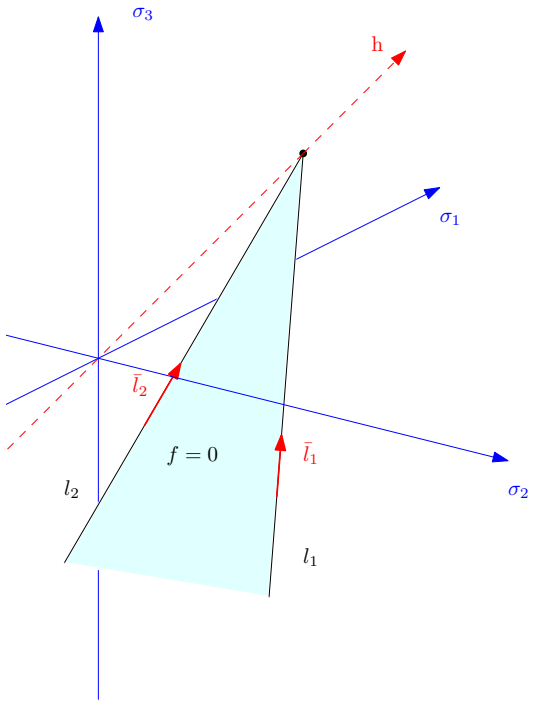

Figure 8.2: Mohr-Coulomb yield plane in principal stress space.

The edge lines of the triangular yield plane, l_1 and l_2, are expressed by:

$$l_1 : \ \bar{\sigma} = t_1 \bar{l_1} + \bar{\sigma}_a, \quad \text{and} \quad l_2 : \ \bar{\sigma} = t_2 \bar{l_2} + \bar{\sigma}_a, \tag{8.11}$$

where

$$\bar{l_1} = \begin{Bmatrix} 1 \\ 1 \\ k \end{Bmatrix} \quad \text{and} \quad \bar{l_2} = \begin{Bmatrix} 1 \\ k \\ k \end{Bmatrix} \tag{8.12}$$

and t_1 and t_2 are unit parameters.

8.2 Return mapping for the Morh-Coulomb criteria

The Mohr-Coulomb criteria imply four different cases of stress returns:

- Return to a yield plane
- Return to a line, l_1 or l_2
- Return to the apex point

When the return mapping scheme is used to return the stress back to a yield plane, line or point, it is important to know where the trial stress is located. The location is described

in terms of a stress region, which are separated by boundary planes.

In the following sections, the definition of the boundary planes and as well as stress regions is examined further, and the routine for returning to a yield plane, line and point is described.

8.2.1 Mohr-Coulomb boundary planes

Boundary planes are defined by the intersection line between two yield planes, $\bar{l}$, and by the plastic corrector $\bar{r}^p$. The directions of these two vectors form a boundary plane, see Figure 8.3.

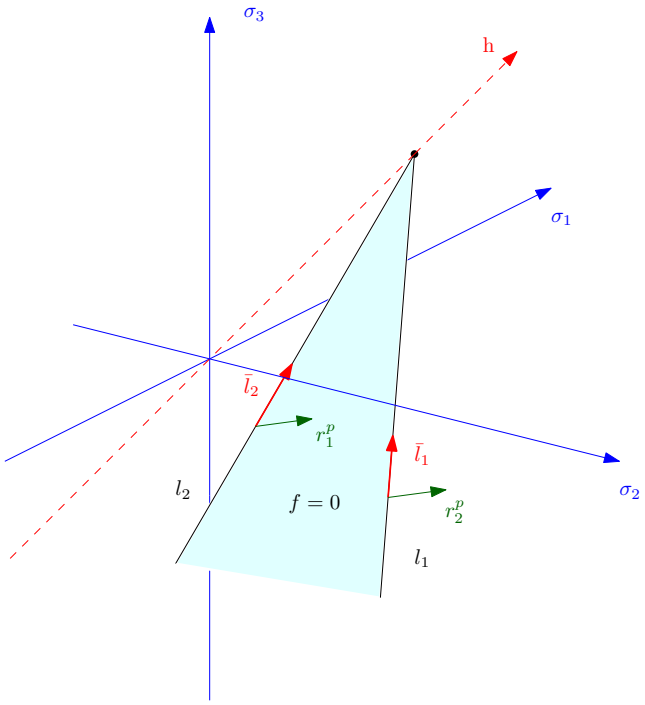

Figure 8.3: Intersection lines $\bar{l}_1$, $\bar{l}_2$ and the plastic corrector $\bar{r}_p$ defining the boundary planes.

The normal to the boundary plane points into one of the stress regions from another stress region. This is indicated by the indices II (into) and I (from). A boundary plane can be expressed with the following equation:

$$p_{\text{II-I}}(\bar{\sigma}) = \left(\bar{r}^p \times \bar{l}\right)^T (\bar{\sigma} - \bar{\sigma}_l) = \bar{n}_{II-I}^T (\bar{\sigma} - \bar{\sigma}_l) \tag{8.13}$$

A Mohr-Coulomb criteria applicable with $\sigma_1 \geq \sigma_2 \geq \sigma_3$ has four boundary planes. For other arrangements of the principal stresses there will also be four boundary planes.

8.2.2 Mohr-Coulomb stress regions

Stress regions are limited by boundary planes and they are as mentioned defined by intersection lines and apex points. Therefore, a Mohr-Coulomb yield criteria will have four stress regions.

Region I is limited by two boundary planes, $p_{\text{I-II}}$ and $p_{\text{I-III}}$. They are defined by the two intersections lines and their corresponding plastic correctors.
Region II and Region III is limited by $p_{\text{I-II}}$ and $p_{\text{I-III}}$, respectively, and the boundary planes formed by the apex, $p_{\text{II-IV}}$ and $p_{\text{III-IV}}$. These boundary planes lies perpendicular on $p_{\text{I-II}}$ and $p_{\text{I-III}}$, and they form Region IV. An illustration of the stress regions is seen on Figure 8.4.

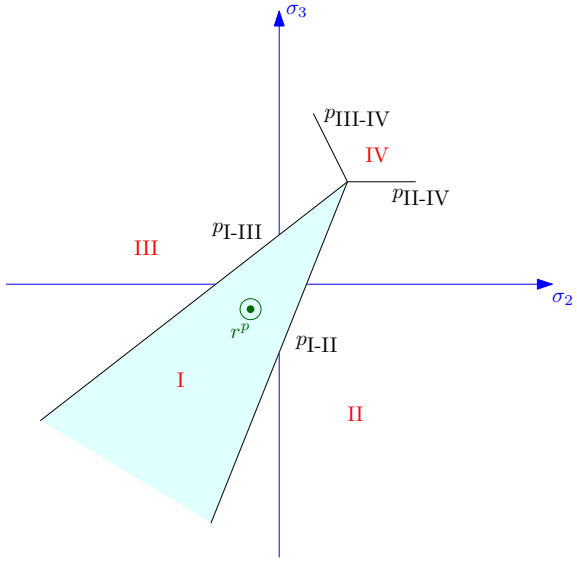

Figure 8.4: Stress regions illustrated by roman numerals.

Depending on which region the trial stress is located, there are four possible outcomes for the Mohr-Coulomb stress return, as given in Table 8.1.

Table 8.1: The possible outcomes for the Mohr-Coulomb stress return.

Region	Conditions for boundary planes			Return to
I	$p_{\text{I-II}} \geq 0$	$\wedge$	$p_{\text{I-III}} \leq 0$	Plane, $f = 0$
II	$p_{\text{I-II}} < 0$	$\wedge$	$p_{\text{I-III}} < 0$	Line, l_1
III	$p_{\text{I-II}} > 0$	$\wedge$	$p_{\text{I-III}} > 0$	Line, l_2
IV	$t_1 > 0$	$\wedge$	$t_2 > 0$	Apex point, $\bar{\sigma}_a$

8.2.3 Return mapping

With the stress regions and boundary planes defined, and the possible outcomes described, the return mapping procedure can take place. According to the previous sections, there are three different return schemes to consider: Returning to a yield plane, to the intersection of two planes i.e. a line, and to the intersection of three or more planes i.e. a point.

With three return schemes follows three constitutive matrices. The returns and constitutive matrices for a plane, line and point are outlined in the following subsection.

Returning to a plane

The yield plane is linear in the principal stress space, see Eq. 8.5, and is given by:

$$f(\bar{\sigma}) = \bar{a}^T \left(\bar{\sigma} - \bar{\sigma}^f \right) = 0 \tag{8.14}$$

The plastic potential is also linear in the principal stress space, see Eq. 8.6, and is given by:

$$g(\bar{\sigma}) = \bar{b}^T \bar{\sigma} \tag{8.15}$$

In the equations above $\bar{a}$ and $\bar{b}$ are gradients of the yield plane and the plastic potential, respectively. With the gradients known, see Eq. 8.7 and Eq. 8.8, the scaled direction of the plastic corrector can be determined:

$$\bar{r}^p = \frac{\bar{D}\bar{b}}{\bar{b}^T \bar{D}\bar{a}} \tag{8.16}$$

With all contributions to the plastic corrector stress know, it can be established:

$$\Delta\bar{\sigma}^p = f\left(\bar{\sigma}^B\right)\bar{r}^p \tag{8.17}$$

With the plastic corrector stress determined, the stress can be returned to the Mohr-Coulomb plane:

$$\bar{\sigma}^C = \bar{\sigma}^B - \Delta\bar{\sigma}^p \tag{8.18}$$

It is seen that the return mapping for a plane is similar to the scheme outlined in [5].

Constitutive matrix for return to a Mohr-Coulomb plane

The constitutive matrix should be determined by:

$$\begin{aligned}[\bar{D}]^{ep} =& \frac{E}{(1-\nu)(mk - mk\nu - m\nu - k\nu + 1 + \nu)} \\ &\cdot \begin{bmatrix} 1 & (m+1)\nu & m \\ (k+1)\nu & 1 - m\nu - k\nu + mk & m(k+1)\nu \\ k & (m+1)k\nu & mk \end{bmatrix}\end{aligned} \tag{8.19}$$

And the shear part is defined by:

$$[\bar{G}] = \frac{E}{2\,(1+\nu)}[I] \tag{8.20}$$

Returning to a line

The line is defined as an intersection between two yield planes f_1 and f_2, and is defined by the equation:

$$\bar{\sigma} = t\bar{l} + \bar{\sigma}_l \tag{8.21}$$

Here $\bar{\sigma}_l$ is a point on the intersection line, and $\bar{l}$ is the direction vector of the intersection line. The latter is given by Eq. 8.12. The parameter t of Eq. 8.21 is then given by:

$$t = \frac{\left(\bar{r}_1^p \times \bar{r}_2^p\right)^T \left(\bar{\sigma}^B - \bar{\sigma}_l\right)}{\left(\bar{r}_1^p \times \bar{r}_2^p\right)^T \bar{l}} \tag{8.22}$$

Constitutive matrix for returning to a Mohr-Coulomb line

When a trial stress should be returned to a Mohr-Coulomb line, there are two returns to consider and therefore two constitutive matrices to calculate. The shear part of the constitutive matrices is given by Eq. 8.20, and the normal component part for l_1 and l_2, respectively:

$$[\bar{D}]_{l,1}^{ep} = \frac{E}{2 - 2\nu - 2k\nu - 2m\nu + mk} \begin{bmatrix} 1 & 1 & m \\ 1 & 1 & m \\ k & k & mk \end{bmatrix} \tag{8.23}$$

$$[\bar{D}]_{l,2}^{ep} = \frac{E}{1 - 2k\nu - 2m\nu - 2mk + 2mk\nu} \begin{bmatrix} 1 & m & m \\ 1 & mk & mk \\ k & mk & mk \end{bmatrix} \tag{8.24}$$

8.2.4 Returning to a point

When the outcome of the analysis of stress regions is to return to a point, it can obviously only be to the apex point. The apex point is a known point, which leaves no need for calculations, as the returned stress is:

$$\bar{\sigma}^C = \bar{\sigma}^a \tag{8.25}$$

Since the apex is located on the hydrostatic line, the constitutive matrix for returning to a point is:

$$[\bar{D}_{point}]^{ep} = [0] \tag{8.26}$$

9 Bearing capacity of a strip footing on a Mohr-Coulomb material

Even though the application of the extended element in a nonlinear program did not succeed, it is still investigated how EXT should behave for a Mohr-Coulomb yield criteria. This can be done by using the F-EXT incompatible element, which behaves exactly like the EXT element.

In this chapter nonlinear tests of the F-EXT element are performed using the Mohr-Coulomb material model. A set of tests is carried out using the associated Mohr-Coulomb material model for the case of a strip footing resting on a soil layer in order to examine the performance of the element in the evaluation of the bearing capacity. The performance of the F-EXT incompatible element is compared with the performance of the LST element.

9.1 Analytical solution

The performance of the elements is examined by how well the finite element results converge toward the analytical solution of the bearing capacity.

The analytical solution of the bearing capacity of a strip footing resting on a soil layer is usually determined by Terzaghi's expression, which implies an associated perfect plastic Mohr-Coulomb material model:

$$p = \gamma\, r\, N_\gamma \; + q\, N_q + c\, N_c \tag{9.1}$$

where r is the halfwidth of the strip footing, q is the surface load and c is the cohesion of the soil. The N_γ, N_q and N_c are bearing capacity factors, which all are functions of the friction angle, φ.

The factors N_γ, N_q and N_c have a considerable influence on the the bearing capacity. The exact values of N_q and N_c can be determined using Prandtl's equations, see [9]. Different methods of determination have been proposed for the values of N_γ. Recently values of N_γ has been determined for both rough and smooth footings by Martin, see [16] and [17]. These values are considered as exact values, and therefore the values for a rough footing are used throughout this study.

The bearing capacity will be calculated for three soil materials. The first soil material is sand which is also referred to as a friction material, the second material is clay with a varying cohesion, and the last material is undrained clay also reffered to as a cohesion material.

9.2 Finite element analyses

The following study focuses on the application of the F-EXT incompatible element in the finite element analyses of the bearing capacity for the strip footing.

9.2.1 Finite element model

Due to the summetry of the footing only half of the problem is discretized, in order to reduce the computational costs. Only the soil is discretized into an element mesh, and an example of the mesh is shown in Figure 9.1. The boundaries of the mesh are sufficiently distant from the footing, 6 m horizontally and 5 m vertically. The vertical sides of the mesh are restrained in the horizontal direction, while the base of the mesh is restrained in the vertical direction. Along the top of the mesh, both horizontal and vertical movements are allowed.

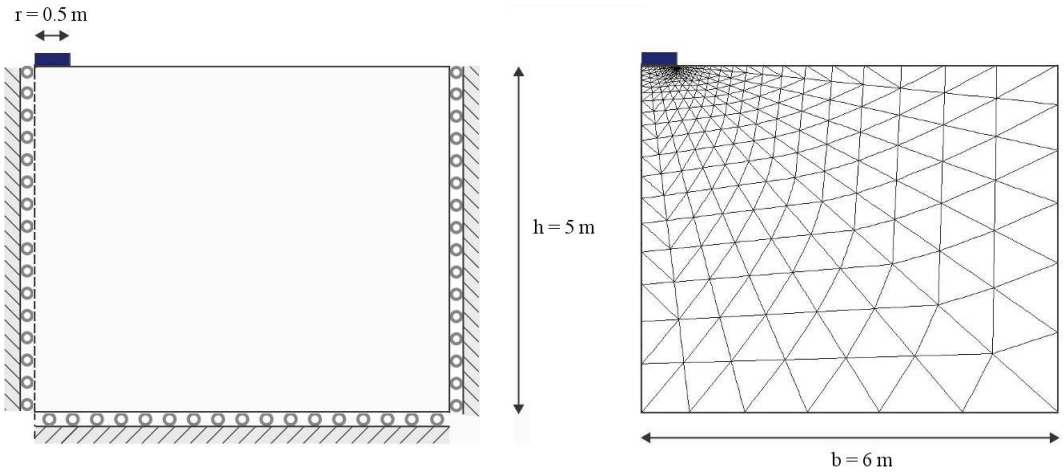

Figure 9.1: Geometry, boundaries and an example of element mesh with 540 elements.

The footing is considered to be rough, which means that the interface nodes at the footing are fixed in the horizontal direction. The loading is then applied in increments of an uniform vertical displacement to the same interface nodes. The load bearing capacity is then obtained by summing up the vertical reaction at the nodes, which have been subjected to displacements.

9.2.2 The influence of tolerance on the results

In the finite element tests, the energy convergence criteria is used, see Section 4.1.1. It is investigated if the solutions obtained for LST and F-EXT incompatible are sensible to the choice of tolerance.

The normalized bearing capacity is plotted as a function of the tolerance of energy error for both friction soil and cohesion soil, see Figure 9.4. The Full Newton-Raphson scheme is used to obtain these results, which are not sensible to the choice of a tolerance value.

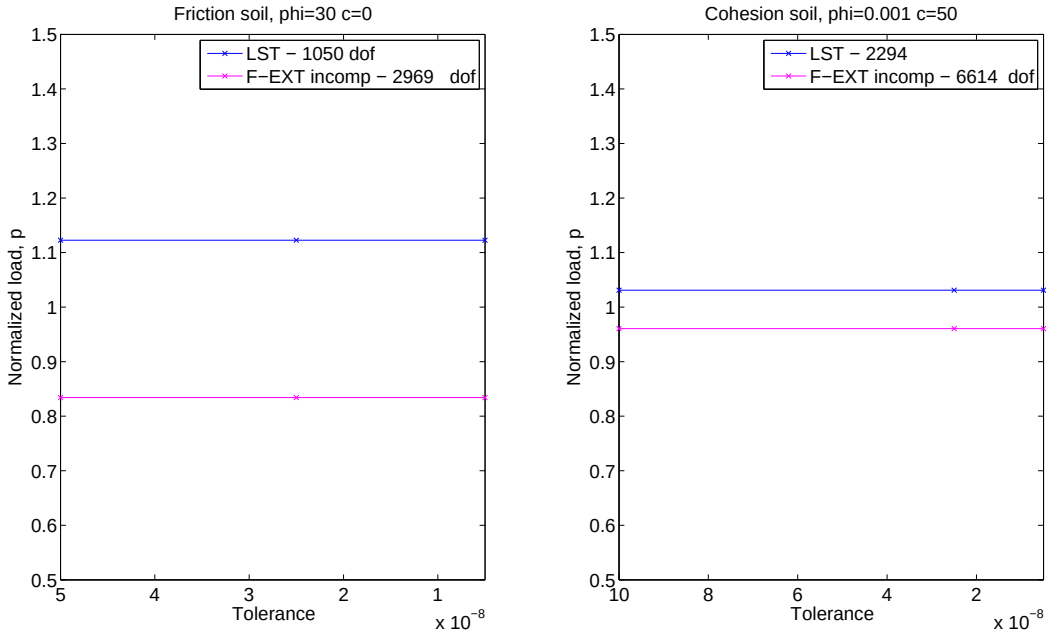

Figure 9.2: The normalized bearing capacity plottet as a function of the tolerance of energy error, $\phi = \psi = 30°$, $c = 0$. Full Newton-Raphson Method.

However, with the Initial Stiffness Method, consistent solutions of the bearing capacity is not obtained with F-EXT incompatible, when the tolerance value of energy error is changed. This is shown in Figure 9.3, where the normalized bearing capacity is plottet as a function of the tolerance. It is seen that the tolerance has an influence on the solution. Furthermore the Initial Stiffness Method requires a considereable number of iterations to converge, and only more as the tolerance value decreases. Therefore the bearing capacaty is not computed with a tolerance smaller than $1e - 6$.

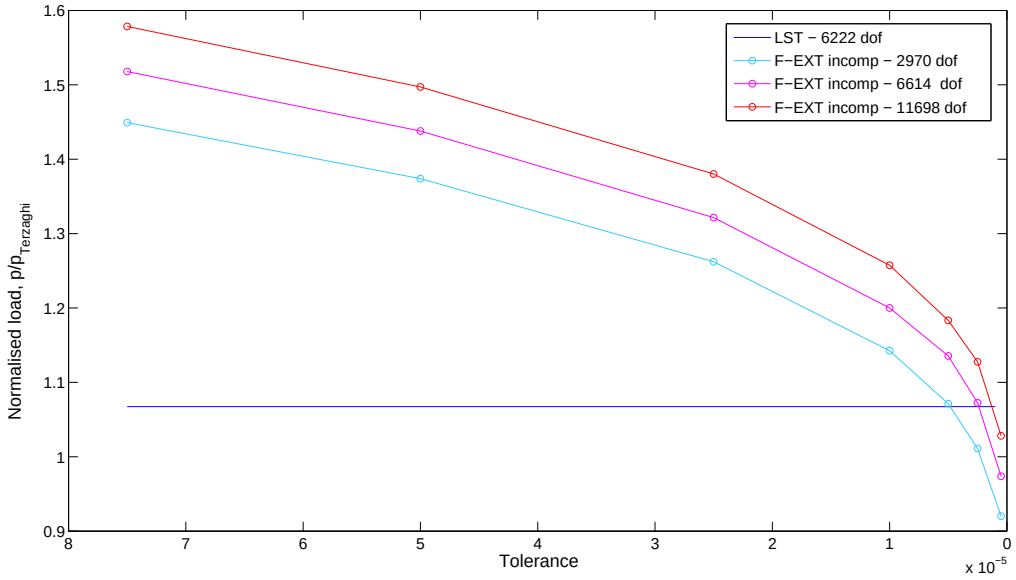

Figure 9.3: The normalized bearing capacity plottet as a function of the tolerance of energy error, $\phi = \psi = 30°$, $c = 0$. Initial Stiffness Method.

In Figure 9.4 the bearing capacity and tolerance is plottet in 3D with the number of d.o.f. in the third direction. It appears that if the number of d.o.f. is increased the tolerance of error should be decreased.

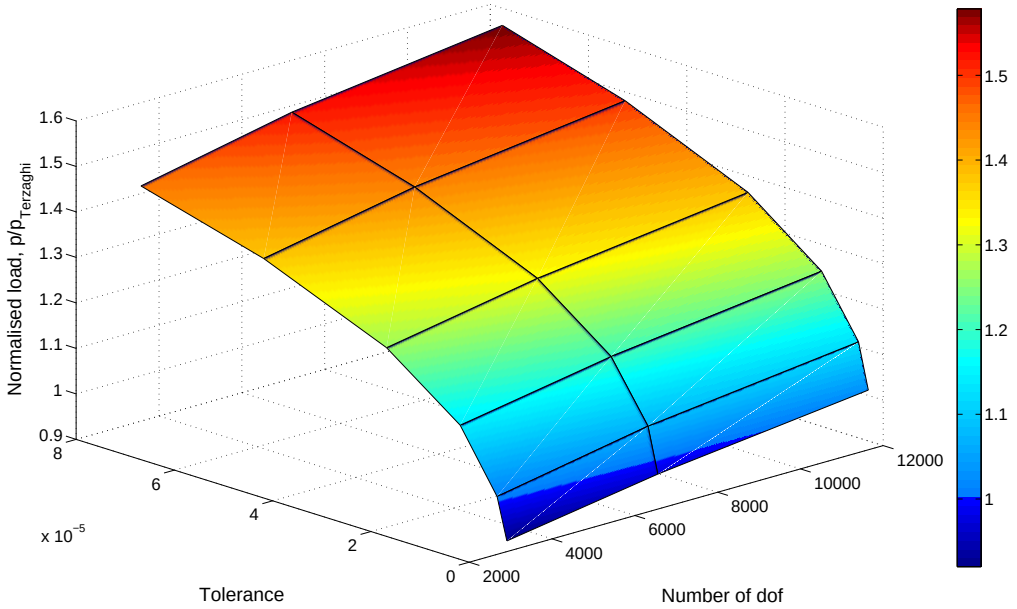

Figure 9.4: The normalized bearing capacity plottet as a function of the tolerance of convergence and number of d.o.f, $\phi = \psi = 30°$, $c = 0$. Initial Stiffness Method.

Thus, the tolerance has an influence on the accuracy of F-EXT incompatible when the Initial Stiffness Method is used with a Mohr-Coulomb material model, but the tolerance also has influence on the speed of the solution. If the tolerance is too high, the results may be inaccuate, and if the tolerance is too small it results in a high computational time.

The results for the Initial Stiffness Method are obviously not satisfying. In the following section, the results of analyses carried out with the Full Newton-Raphson scheme are presented.

9.2.3 Results

Test 1 - Sand

The bearing capacity is at first computed for the strip footing resting on a sand material, also reffered to as a friction material, see Table 9.1.

Table 9.1: Material parameters of the sand.

		Material 1	
Type of material behaviour Parameters		Drained	-
Soil unit weight	γ'	15	kN/m^3
Friction angle	φ'	30	$^\circ$
Dilatation angle	ψ'	30	$^\circ$
Cohesion	c'	0	kN/m^2
Pressure coefficient at rest	K_0	0.5	$^\circ$
Young's modulus	E'	50000	kN/m^2
Poisson's ratio	ν'	0.3	-
Interface stregth		rough	-

The bearing capacity for different meshes of F-EXT incompatible and LST are given from the load-displacement curves computed with LST and F-EXT incompatible on Figure 9.8. The load-displacement curves are displayed together with the bearing capacity calculated analytically, $p_{Terzaghi} = 110.657$ kN/m.

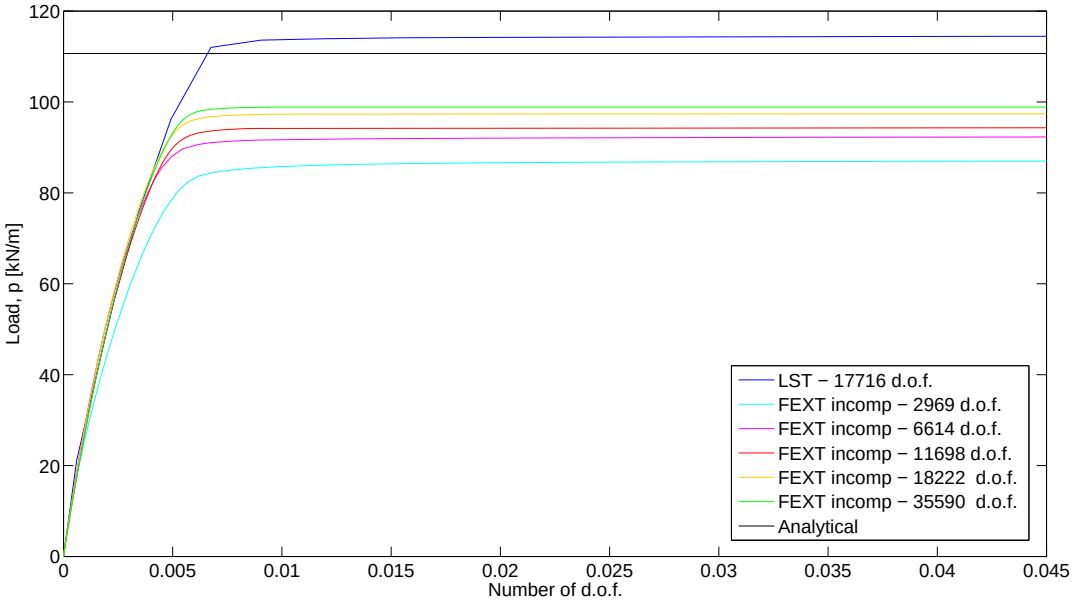

Figure 9.5: Load-displacement curves for a friction material, $\phi = \psi = 30°$, $c = 0$.

The convergence of LST and F-EXT incompatible is displayed in Figure 9.9, where the bearing capacity is normalized with the analytical solution.

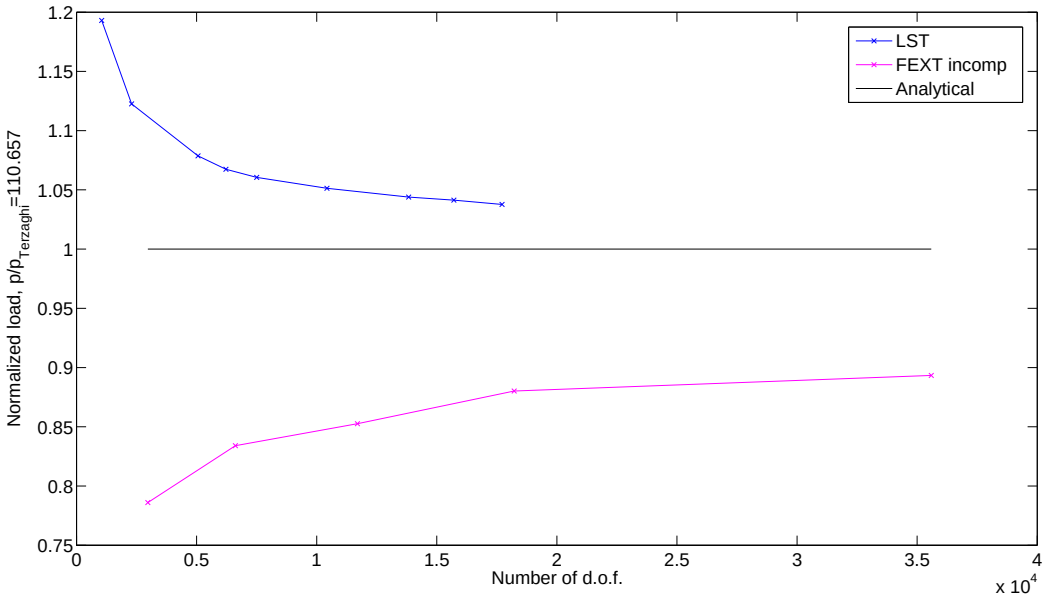

Figure 9.6: Convergence of the normalized bearing capacity for a friction material, $\phi = \psi = 30°$, $c = 0$.

The error of the bearing capacity obtained for the discretization with the LST element is

3.76 % compared to the analytical solution, whereas the error for the F-EXT incompatible element is 10.67 %.

LST converges from above and towards the analytical solution, while F-EXT incompatible converges from below and towards the analytical solution. Thereby, the bearing capacity is not overestimated with use of the F-EXT incompatible element.

Thus, the F-EXT incompatible element can be used with advantage for cohesionless soils, even though the computational time is higher compared to LST. Accordingly, a set of tests is carried out for a soil material with a varying cohesion, in order to investigate whether or not the F-EXT incompatible element is benefitial in cases with cohesive soil.

Test 2 - Clay

If the bearing capacity is computed for the strip footing on a clay material with varying cohesion, as outlined in Table 9.2, the results displayed in Figure 9.7 are obtained.

Table 9.2: Material parameters of the clay material.

		Material 2	
Type of material behaviour		Drained	-
Parameters			
Soil unit weight	γ'	15	kN/m^3
Friction angle	φ'	30	$^\circ$
Dilatation angle	ψ'	30	$^\circ$
Cohesion	c'	varying	kN/m^2
Pressure coefficient at rest	K_0	0.5	$^\circ$
Young's modulus	E'	10000	kN/m^2
Poisson's ratio	ν'	0.3	-
Interface stregth		rough	-

In addition to the results of the bearing capacity computed with LST and F-EXT incompatible at different values of cohesion, Figure 9.7 shows the corresponding analytical solutions.

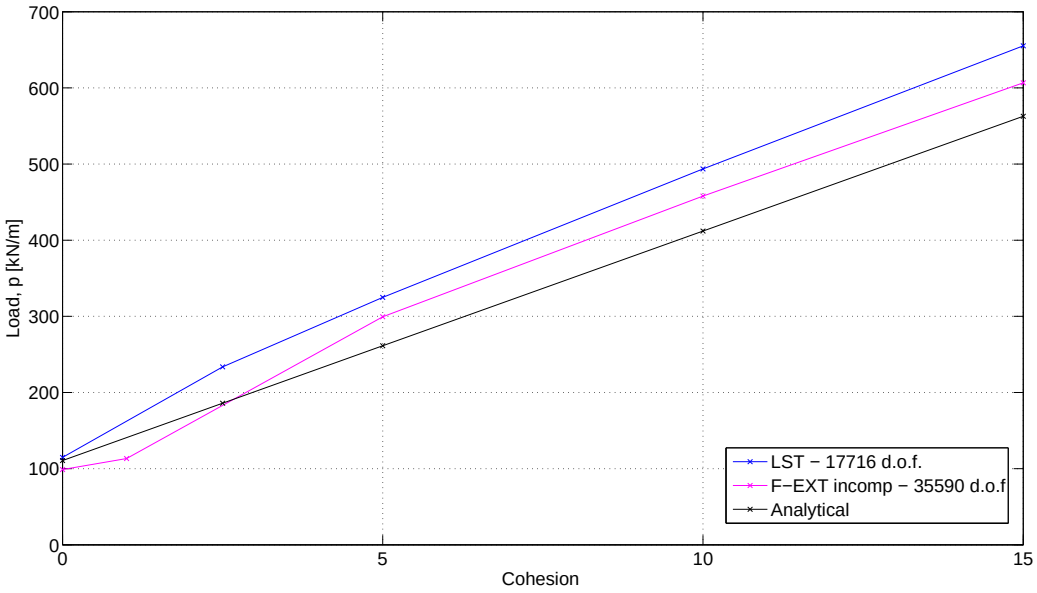

Figure 9.7: The bearing capacity computed with LST and F-EXT incompatibel at different values of cohesion.

It is evident that the bearing capacity is overestimated with a refined mesh of F-EXT incompatible elements, when the cohesion of the material increases. However, the results are still closer to the analytical solutions compared to LST.

Test 3 - Undrained clay

The bearing capacity for the strip footing resting on an undraind clay material is computed, i.e. in the case of a cohesion material. However, the computation can not run with zero value of friction and dilatation when the Mohr-Coulomb model is used, and therefore the bearing capacity of the cohesion material is computed by assigning a low value of $\phi = \psi = 0.001°$.

Table 9.3: Material parameters of the undrained clay material.

		Material 3	
Type of material behaviour		Undrained	-
Parameters			
Soil unit weight	γ	15	$\mathrm{kN/m^3}$
Friction angle	φ	0.001	°
Dilatation angle	ψ	0.001	°
Cohesion	c_u	50	$\mathrm{kN/m^2}$
Pressure coefficient at rest	K_0	1	°
Young's modulus	E	10000	$\mathrm{kN/m^2}$
Poisson's ratio	ν	0.3	-
Interface stregth		rough	-

On Figure 9.8 load-displacement curves for LST and F-EXT incompatible are displayed with the analytically bearing capacity, $p_{Terzaghi} = 257.091$ kN/m.

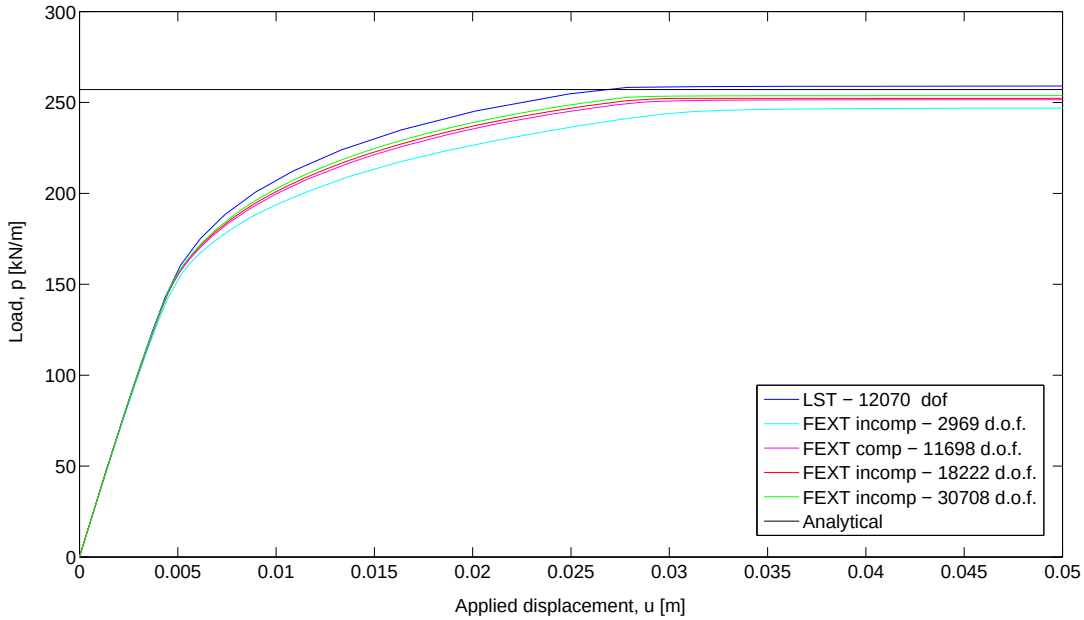

Figure 9.8: Load-displacement curves for a friction material, $\phi = \psi = 0.001°$, $c = 50$ kN/m^2.

The convergence of the normalized bearing capacity computed with LST and F-EXT incompatible is displayed in Figure 9.9:

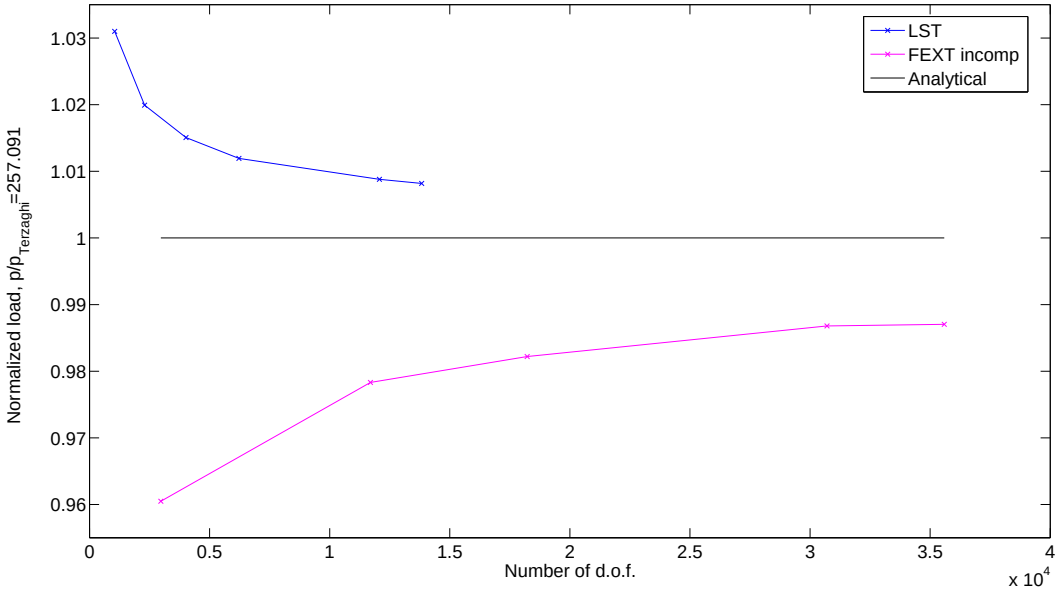

Figure 9.9: Convergence of the normalized bearing capacity for a friction material, $\phi = \psi = 0.001$, $c = 50$ kN/m^2.

The bearing capacity obtained for the refined mesh of LST gives an error of 0.88 % in error compared to the analytical solution. The error for the F-EXT incompatible element is 1.30 %. As seen in the case of cohesionless soil, the F-EXT element converges from below towards the analytical solution in the case of cohesion soil. Thereby, the bearing capacity is not overestimated.

When the bearing capacity of the footing is reached, the following failure mechanism of the soil occurs with the F-EXT incompatible element. Figure 9.10 shows the failure of the soil in x-direction, which is consistent with the theoretical failure figure for cohesion soil. The theoretical failure figure consists of straight lines and circular arc, as shown on the figure [9].

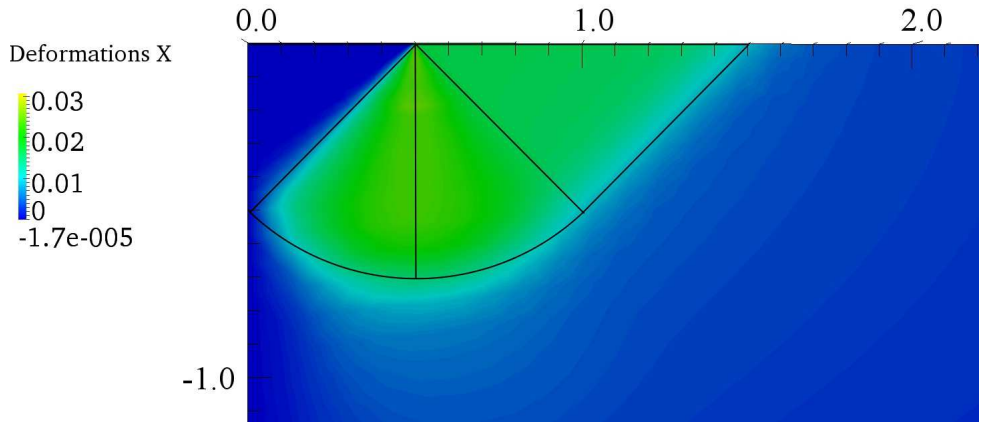

Figure 9.10: Plot of failure in x-direction

Figure 9.11 shows the failure of the soil in y-direkction

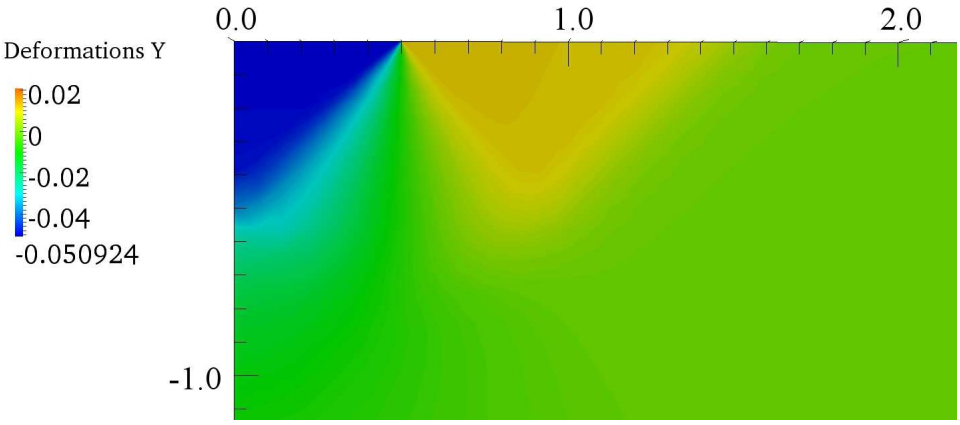

Figure 9.11: Plot of failure in y-direction.

9.3 Conclusion on tests of a strip footing with Mohr-Coulomb's criteria

For a strip footing resting on a friction soil material it appears that the F-EXT incompatible converges from below and towards the analytical solution. Thereby, the load bearing capacity is not overestimated with use of this element, as opposed to when the LST element is used.

It is seen for a material with both friction and cohesion that the bearing capacity is overestimated with use of F-EXT, when the cohesion is increased. However, the results are closer to the analytical solutions compared to LST, and the F-EXT incompatible element is therefore preferable.

For a strip footing in a frictionless cohesive material it is also evident that F-EXT incompatibel does not overestimate the bearing capcity. Thus, it can be concluded that the F-EXT element with advantage can be used in the finite element analysis of the bearing capacity of a strip footing, even though the computational time is higher compared to LST.

10 Discussion

A new triangular element has been implemented in a nonlinear, elastic-plastic finite element program in order to test the abilities of the element. The performance of the extended element (EXT) as well as the full extended element (F-EXT) is compared to the well-known LST element.

The first tests of the element was linear-elastic analyses in order to ensure that the element is stable and provides the expected results. The element was able to pass the patch test. For the test of Cook's membrane, the element overestimated the displacements and stresses. The same conclusion was made for the test of a plate with a circular hole.

The stress at the edge of the hole was highly overestimated for coarse meshes, but as the mesh was refined, the results improved. The stresses along the symmetri line was plottet, revealing that the gradients in the EXT and F-EXT elements had a significant impact on the stress distribution. For finer meshes, that impact was reduced a great deal.

The results for the linear-elastic tests revealed that the new extended element does not perform well in those kinds of analyses, and especially not for coarse meshes, as the element is too flexible and overestimates the displacements. However, this behavior is expected for incompatible elements. The overly flexible properties of EXT and F-EXT incompatible decreases and eventually becomes insignificant for a sufficient refined mesh.

The elements were also tested in a nonlinear finite element program with von Mises yield criteria, in order to ensure that the application of the nonlinear part of the finite element program was implemented correctly. The case of plane stress applied to a patch test was first considered, and it quickly became apparent that the extended element has serious difficulties with perfectly-plastic nonlinearities.

The problem arise when the stiffness matrix for each element is updated. This generates additional zero-eigenvalues which results in a singular stiffness matrix. This phenomenom is limited to perfect-plasticity, and can appear when two adjacent elements are in a state of yielding [12].

The authors have been unable to resolve the problem, but suggests an approach of adding a small hardening parameter in order to prevent the state of perfect-plasticity. For the patch test this method was useful, but the subject must be examined further.

The case of plane strain applied to a patch has also been tested with the use of von Mises yield criteria. In this test, the EXT element was able to converge.

According to W. Pan et. al. [23] the solution in the condensed d.o.f. must not effect the global solution. Therefore it is examined what happens to the residual force vector for an element in the patch for plane stress and plane strain, respectively. It turns out that the nonlinearity with the following update of the stiffness matrix does not influence the global solution in the case of plane strain. This is seen in the residual force for the condensed d.o.f. where the values stays close to zero.

However, in the case of plane stress the residual forces in the condensed d.o.f. increases drastically. Since the residual force vector is used to unpack the displacements for the next iteration, this increase has an imidiate impact on the solution. The high residual forces leads to an overestimation of the displacement of the condensed d.o.f., which then again

gives an even higher residual forces and thus the element is unable to converge.

Since a patch test does not represent any real structure, regarding boundary conditions or loadings, it is useful to examine plane strain in other applications. The bearing capacity of a strip footing on a soil layer was therefore analysed as an analytical bearing capacity has been calculated for von Mises yield criteria. The analyses shows that LST and F-EXT compatible overestimates the bearing capacity, as expected.

However, EXT is not able to converge after it reaches the yielding point. This may be due to the residual forces of the condensed d.o.f. If they become too large, the element is unable to converge. As seen in the plane stress test, good results were obtained by adding a small hardening parameter. A hardening parameter has also been implemented in this case, but the solution still do not converge.

The bearing capacity has also been determined with use of F-EXT incompatible elements, in order to investigate which results could have been obtained for EXT if it had been able to converge. The bearing capacity for F-EXT incompatible is less than the analytical bearing capacity, and therefore on the safe side. This is in good correspondance with one of the aims of this thesis: to obtain a more accurate solution to geotechnical problems.

As a final demonstration of the problems with using the EXT elements in a nonlinear analysis, a test of the patch subjected to an unsymmetrically applied displacement is performed. Again, EXT is unable to converge, whereas the other three element types do converge. The residual forces of the condensed d.o.f. are subject to investigation again, and it is seen that the values herein shifts within a certain range. The values are too small to cause severe problems when updating the stiffness matrix, but large enough to prevent convergence. Instead, the program runs through iterations until the maximum limit is allowed - even at a maximum number of iterations of 500.

Even though the EXT element was not able to converge with the somewhat simple von Mises yield criteria, the F-EXT incompatible element is tested with the application of Mohr-Coulomb's yield criteria. This is because F-EXT incompatibel gives the same results as EXT should have given if the authors had succeeded on implementing the element in a nonlinear program. The computational costs of using F-EXT incompatibel are, when looking at number of d.o.f., higher, but it can be doubted how much computational time could be saved by using EXT.

Normally, the substructuring method implies that the global stiffness matrix can be formulated ones, and when using this stiffness matrix several times throughout the same analysis, computational costs are saved. But with the use of a Full Newton-Raphson scheme, all stiffness matrices of yielding elements must be reformulated for every iteration. Thus, a lot of the inteded savings will be outrun by reformulation and condensation with every iteration.

The method of only condensating the linear part of the structure is to the author's belief the most economic way to perform a nonlinear analysis. However, the user must be able to identify which parts of a structure that remains elastic and can be represented by EXT, and which parts should be represented by F-EXT incompatible.

If the nonlinear region is unknown, an identifyer of how close an element is to yielding, should be implemented. W. Pan et al. suggests that an element who has reached 60-70 % of the yielding limit, should be included in the nonlinear region [23].

Note should be taken on the importance of having a sufficiently large nonlinear region, as the solution can be disrupted if a yielding element is too close to the boundary of the nonlinear region.

The purpose of the EXT element was to improve the finite element analyses of geotechnical problems. The purpose is not achieved with the EXT element, however it is shown that the F-EXT incompatible element improves the finite element analyses of a common geotechnical problem significantly. This is seen in the analyses of the bearing capacity for a strip footing resting on a friction soil material and a cohesion soil material, respectively. In both cases the F-EXT incompatible converges from below and towards the analytical solution. Thus, the bearing capacity is not overestimated with the F-EXT, as opposed to when the LST element is used.

It is seen for a material with both friction and cohesion that the bearing capacity is overestimated with use of F-EXT, when the cohesion is increased. However, the results are closer to the analytical solutions compared to LST, and the F-EXT incompatible element is therefore preferable even though the computational cost is higher. The computational costs can be reduced if the condensation of the element (EXT) can be solved in connection with nonlinear problems.

Although the F-EXT incompatible element provides good results it would be advisable to perform additional tests of the convergence and accuracy of the element in other geotechnical applications. This may be done for a finite element analysis of slope stability, where the factor of safety is often overestimated with use of conventional elements.

11 Conclusion

The purpose of this thesis was to formulate a new flexible triangular element, that was suitable for geotechnical analyses. The element is based on the accuracy of the quadratic strain triangular element and the computational speed of the linear strain triangular element.

By reduction of nodes of the QST element and the following static condensation of d.o.f., the element consists of only 6 nodes and 12 d.o.f. when it is assembled in the global system. But internally, the element consists of 7 nodes and 20 d.o.f. This formulation maintains the accuracy of the strains calculated for each element, but has the advantage that the global equilibrium equations are faster to solve due to the fewer d.o.f. used in the global stiffness matrix.

Furthermore, condensation of the gradients allows an incompatibility between elements for these d.o.f. This adds to the flexibility of the element, and makes the element converge from "the opposite side" compared to compatible elements. This is favorable in geotechnical problems, as numerical solutions tends to overestimate the bearing capacity. i.e. the solution is on the unsafe side.

Several tests has been carried out to verify if the element is in fact able to combine accuracy and low computational costs. First of all, it was validated that the element was able to pass the patch test and provides a stable solution.

The results for the linear tests was consistent with the expectations: the element did not perform well for coarse meshes, but with sufficient refinements of the mesh, reasonable results are obtained.

The results for the tests with von Mises yield criteria did not meet the expectations. The element was unable to converge for a plane stress patch test. It was nescesarry to add a hardening parameter to overcome the difficulties, and the initial test with hardening did look promising.

Subsequently, the same test was performed for the case of plane strain. In this test the element converged. A study of the residual force vectors for the condensed d.o.f. for plane stress and plane strain showed that for the latter, the values of the residual force vector for the condensed d.o.f. remained close to zero during the analysis.

This was opposite to the residual force vector for the case of plane stress, where the residual force in the condensed d.o.f. increased drastically and thereby making the stiffness matrix singular.

In other tests of plane strain, the element was not able to converge. The residual force vector was again examined, and the residual forces for the condensed d.o.f. shifted between a few values large enough to prevent the solution to converge.

The bearing capacity of a strip footing on a soil layer was also investigated for von Mises yield criteria. For this problem, the element was not able to converge either. However, the full extended incompatible element performed well and therefore the full extended incompatible element has been tested for Mohr-Coulomb's yield criteria.

The full extended incompatible element is identical to the extended element prior to the static condensation. Therefore it can be used to show how the results would look like if the extended element was able to converge in a nonlinear analysis.

The results are promising as the full extended incompatible element, for most of the cases considered, did not overestimate the bearing capacity of the strip footing. If the extended element can be formulated in such a way that it can be used in nonlinear analyses, the number of d.o.f. needed in the global analysis can be reduced a great deal.

But as discussed previously, the question is if the reformulation and condensation of the extended element in every iteration for a nonlinear analysis, is in fact reducing computational costs.

Bibliography

[1] *Eurocode 7: Geotechnical design - Part 1: General rules.* Dansk standard, 2nd edition edition, 2007.

[2] A. H. van den Boogard A. Hadoush. Substructuring in the implicit simulation of single point incremental sheet forming. Technical report, Materials Innovation Institute, University of Twente, 2008 [Annex].

[3] Lars Andersen. Material modelling in civil engineering, lecture 3-3: Solution of non-linear equations. Technical report, Aalborg University, 2010.

[4] S. Alexander C. A. Felippa. Membrane triangles with corner drilling freedoms. implementation and performance evaluation. Technical report, Finite Elements in Analysis and Design 12, pp. 203-239, 1985.

[5] Johan Clausen. Efficient non-linear finite element implementation of elasto-plasticity for geotechnical problems. Technical report, Esbjerg Institute of Technology, 2007.

[6] R. D. Cook. Improved two-dimensional finite element. Technical report, Journal of the Structural Division, Vol. 100, No. 9, pp. 1851-1863, 1974.

[7] O. J. A. Goncalves D. R. J. Owen. Substructuring techniques in material nonlinear analysis. Technical report, Department of Civil Engineering, University of Wales, 1985 [Annex].

[8] D. R. J. Owen E. A. de Souza Neto, D. Peric. *Computational Methods for Plasticity, Theory and Application.* John Wiley and Sons pp. 583-597, 1980.

[9] N. K. Ovesen et ak. *Lærebog i geoteknik.* Polyteknisk Forlag, 1rd edition, 2007.

[10] R. Chowdhury et al. *Geotechnical Slope Analysis.* CRC Press, 3rd edition, 2010.

[11] R. D. Cook et al. *Concepts and applications of finite element analysis.* John Wiley & Sons, 4th edition, 2002.

[12] Sheu Chyi-Horng G. De Roeck, M. Van Laethem. Multi-level substructuring in the elasto-plastic domain. Technical report, Department of Civil Engineering, Catholic University of Leuven, 1988 [Annex].

[13] T. K. Hellen. Use of substructuring in non-linear material analysis. Technical report, Berkeley Nuclear Laboratories, 1984 [Annex].

[14] Niels Ole Jessen. Numerisk analyse af centralt og excentrisk belasted stribefundamenter. Technical report, Esbjerg Institute of Technology, 2007.

[15] R. R. Pedersen L. Damkilde. A new accurate yet simple shear flexible triangular plate element with linear bending strains. Technical report, Esbjerg Institute of Technology, 2010 [Annex].

[16] C. M. Martin. Exact bearing capacity calculations using the method of characteristics. Technical report, Department of Engineering Science, University of Oxford, 2005 [Annex].

[17] C. M. Martin. Exact bearing capacity for strip footings. Technical report, Department of Engineering Science, University of Oxford, 2005 [Annex].

[18] C. A. Felippa P. G. Bergan. A triangular membrane element with rotational degrees of freedom. Technical report, Computer methods in applied mechanics and engineering, 1985.

[19] Plaxis. Plaxis 2d referencece manual, version 9.0. Technical report.

[20] L. A. Lopez Robert H. Dodds Jr. Substructuring in linear and nonlinear analysis. Technical report, University of Kansas, 1985.

[21] M. Van Laethem P. Geyskens Sheu Chyi-Horng, G. De Roeck. Multi-level substructuring and an experimental self-adaptive newton-raphson method for two-dimensional nonlinear analysis. Technical report, Department of Civil Engineering,Catholic University of Leuven, 1988 [Annex].

[22] John F. Abel Tao-Yang Han. Adaptive substructuring techniques in elasto-plastic finite element analysis. Technical report, Department of Structural Engineering and Program of Computer Graphics, Cornell University, 1985 [Annex].

[23] T. H. Hyde W. Pan, S. B. Leen. Investigation of an iterative sub-structure method for elastic and elastic-plastic framework analysis. Technical report, University of Nottingham, 2005 [Annex].

[24] Hai Sui Yu. *Plasticity and Geotechnics*. Springer Science, 2006.

A Geotechnical problems

One of the geotechnical problems considered in this appendix is the stability of a simple slope model consisting of one soil layer. Another geotechnical problem considered is the bearing capacity of a strip footing placed on a soil layer. Common to these problems are that they can be assessed by analytical calculations. Thus, the finite element results from the software Plaxis can be compared with the results obtained by analytical calculations.

A.1 Slope stability analysis

The stability analysis of a slope model is carried out to assess the factor of safety associated with a critical slip surface. The factor of safety for a slip surface is calculated as a ratio of resisting forces and driving forces:

$$F = \frac{\text{Sum of resisting forces}}{\text{Sum of driving forces}}$$

Within a slope, various potential slip surfaces can be considered. Each of these slip surfaces will have a different factor of safety. The slip surface for which the factor of safety is minimum is called a critical slip surface. Thus, the minimum of this factor is regarded in the slope stability analysis. For a simple slope model consisting of a Mohr-Coulomb soil, this can be carried out by analytical calculation based on limit equilibrium (LE) methods. However, it is often necessary to calculate a various number of potential slip surfaces to finde the critical slip surface, and therefore it can be usefull to use a software based on the same methods. In the following the slope stability analysis is carried out using the software Slope/w based on the LE methods. Similarly, the analysis is carried out using the software Plaxis based on the finite element (FE) method.

A.1.1 Geometry and material parameters

Figure A.1 shows the simple slope model with an external load of 50 kN/m^2. The slope is 20 m wide and 10 m high, i.e. the slope has an inclination of 1:2.

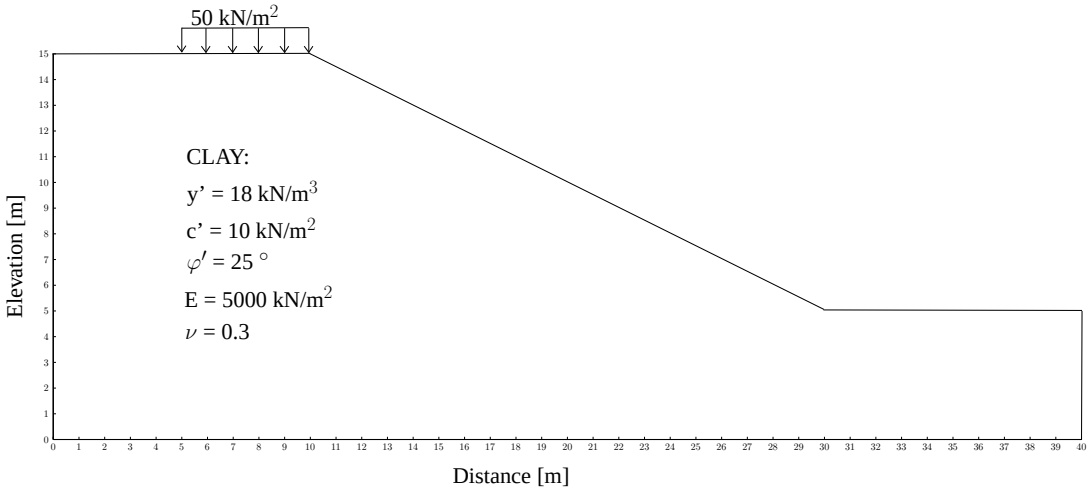

Figure A.1: Slope model with an external load of 50 kN/m^2.

The slope itself is composed of a clay material with the parameters given in Table A.4.

Table A.1: Material parameters of the soil layer.

General		Soil layer	
Material model	Model	Mohr-Coulomb	-
Soil Type		Clay	-
Type of material behaviour		Drained	-
Parameters			
Soil unit weight above p.l.	γ_d	18	kN/m^3
Cohesion	c	10	kN/m^2
Friction angle	φ	25	°
Dilatancy angle	ψ	25	°
Permeability	k	1.0	m/day
Young's modulus	E	50.000	kN/m^2
Poisson's ratio	ν	0.3	-

A.1.2 Analytical solution using LE

The stability of the slope is first assessed by Slope/w calculations based on the most commonly used limit equlibrium (LE) method referred to as the Ordinary method of slices [10]. By this method a circular slip surface is assumed as shown in Figure A.2.a, and the soil mass above the assumed slip surface is divided into vertical slices. The forces on a slice are shown in Figure A.2.b.

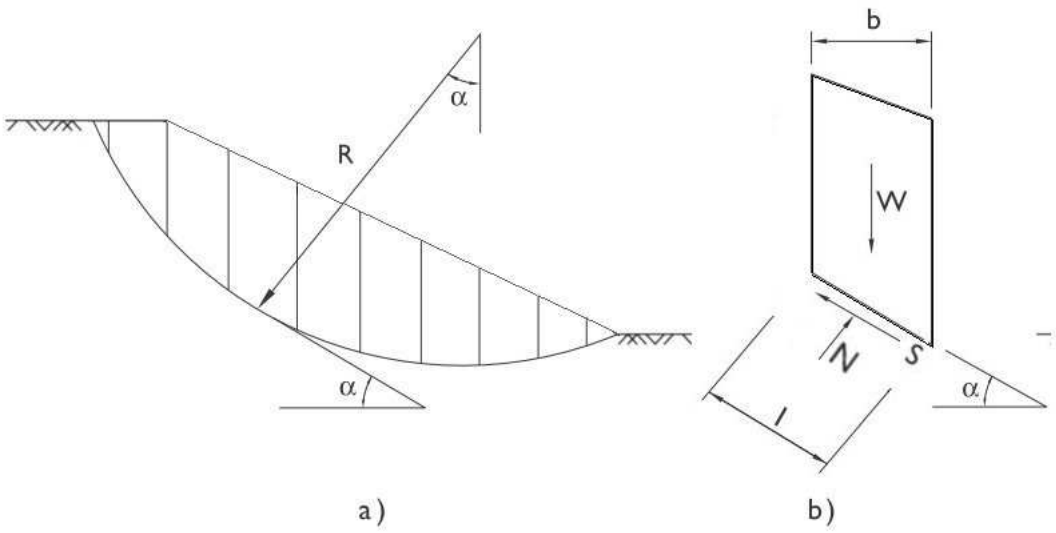

Figure A.2: Ordinary method of slices: (a) Circular slipe surface (b) Forces acting on a slice. [10]

Moment equilibrium about the centre of the slip circle implies the following equation obtained for the factor of safety defined as a ratio of resisting and driving moments:

$$F = \frac{\sum(c'l + N' \tan \varphi')}{W \sin \alpha}$$

$$N' = (W \cos \alpha - U) \tag{A.1}$$

Where,

c' is the effective cohesion,
φ' is the effective friction angle,
l is the base length of the slice,
α is the inclination of slipe surface at the middle of the slice,
N is the normal force at each slice,
U is the force due to pre-pressure at each slice, and
W is the weight of each slice.

The stability analysis of the simple slope model shown in Figure **??** is carried out in Slope/w. The minimum factor of safety and the corresponding critical slip surface obtained in the analysis are given in Figure A.3.

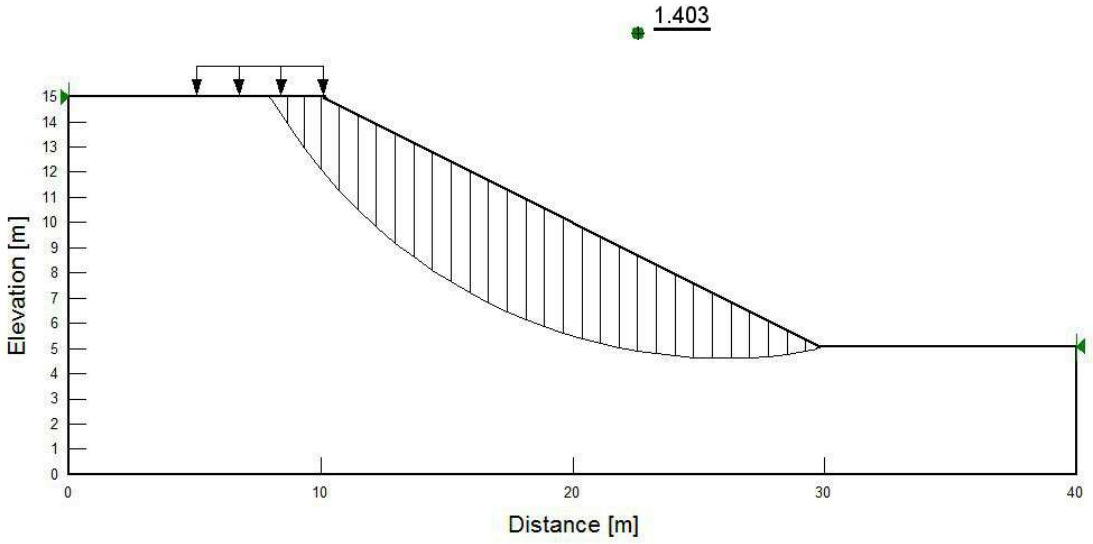

Figure A.3: Factor of safety F=1,403 and corresponding critical surface from Slope/w.

The critical slip found is searched from 125 possible slip surfaces by defining the input of the entry and exit of slip surfaces. The critical slip surface is located with the center coordinates (x,y) = (25.9,25.3) and radius R = 20.7, and is obtained at the factor of safety F = 1.403. This factor is used to compare with the factors obtained from the FE based software.

A.1.3 Finite element solution using Plaxis

The slope stability analysis is then carried out for the same slope model using the software Plaxis. This software computes the factor of safety by a $c-\varphi$ reduction procedure [19]. In this procedure the strength parameters c' and $\tan(\varphi')$ of the soil are reduced until failure of the slope (the critical slip surface) occurs. In this way the factor of safety is computed as the ratio of the input shear strength and the shear strength at failure:

$$F = \frac{\text{Input strength}}{\text{Strength at failure}} \tag{A.2}$$

For a Mohr-Coulomb model, the factor of safety is obtained by:

$$F = \frac{c - \sigma_n \tan(\varphi)}{c_r - \sigma_n \tan(\varphi_r)} \tag{A.3}$$

where,

c and φ are the input strength parameters,
c_r and φ_r are the reduced strength parameters,
σ_n is the actural normal stress component.

First, a plane strain model is defined using 6-node elements to generate the finite element mesh. The results of a refined mesh of 3152 elements and 12942 is shown in Figure A.4.

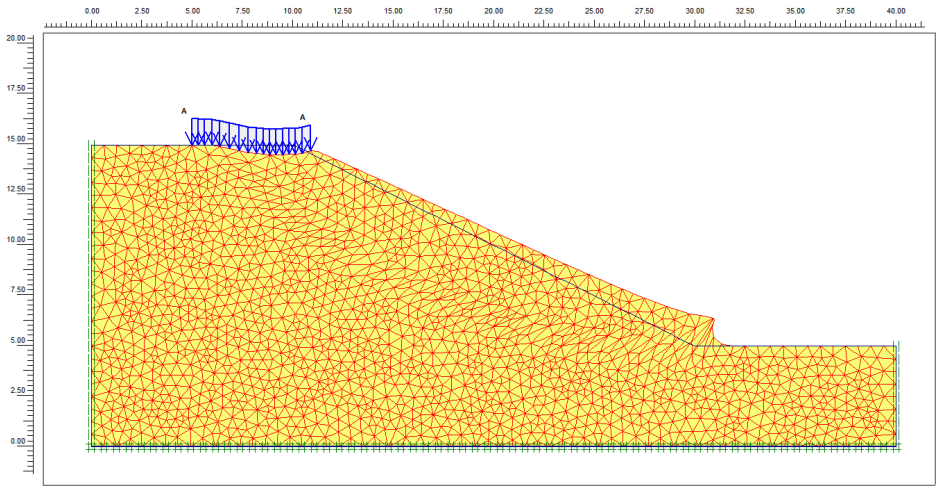

Figure A.4: Deformed mesh with 6-node elements (deformations are scaled to $500*10^{-6}$)

The factor of safety and the critical slip surface obtained with this mesh is given in Figure A.5. The critical slip surface is indicated with a contour plot of the total displacements.

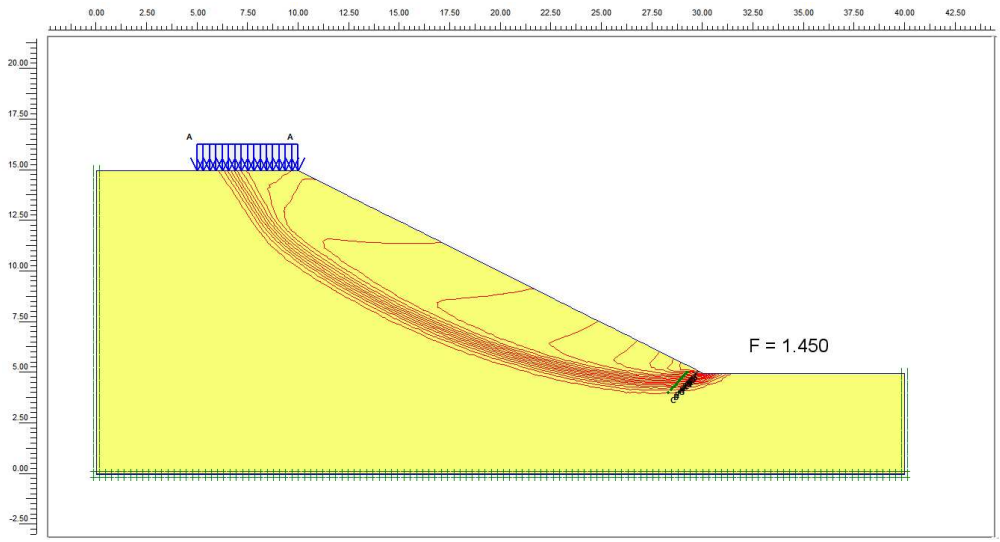

Figure A.5: Factor of safety and a contour plot og the displacements obtained with 6-node elements in Plaxis

Table A.2 shows the factor of safety obtained by further mesh refinements. It is seen that the use of 6-node elements cause a slow convergence, as the convergence is not achieved before 29309 elements and 118312 d.o.f.

Table A.2: The factor of safety obtained by different meshes with 6-node elements

Mesh refinement	Element nr.	Dof nr.	Avg. element size	Factor of safety
1	157	712	1950 mm	1,489
2	336	1466	1340 mm	1,479
3	747	3156	895 mm	1,465
4	1556	6466	620 mm	1,455
5	3152	12942	436 mm	1,450
6	6713	27332	299 mm	1,444
7	13194	53446	213 mm	1,444
8	29309	118312	143 mm	1,443

Next, a plain strain model is defined using 15-node elements to generate the finite element mesh. The results of a well-refined mesh of elements 747 and 12286 d.o.f. is shown in Figure A.6.

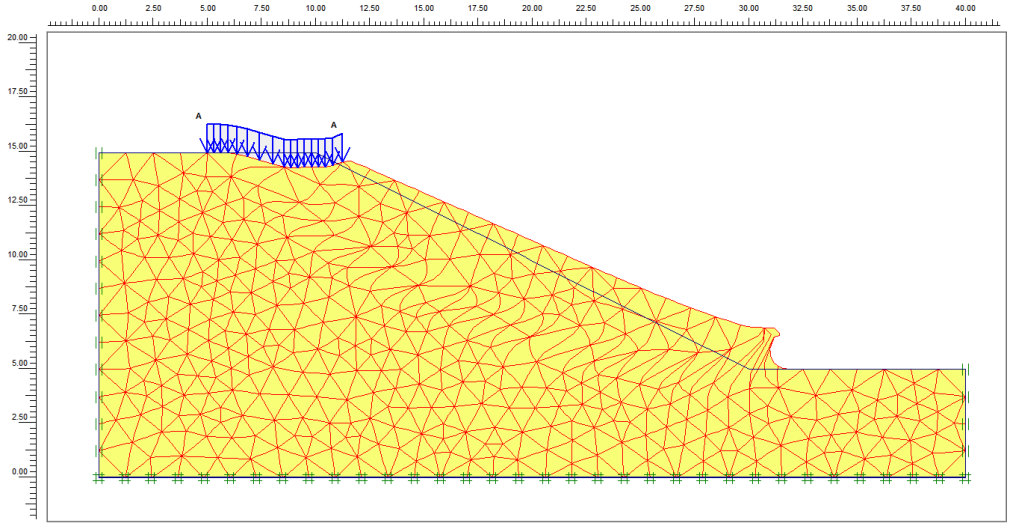

Figure A.6: Deformed mesh with 15-node elements (deformations are scaled $500*10^{-6}$)

The factor of safety and the critical slip surface is given in Figure A.7. The critical slip surface is indicated with a contour plot of total displacements.

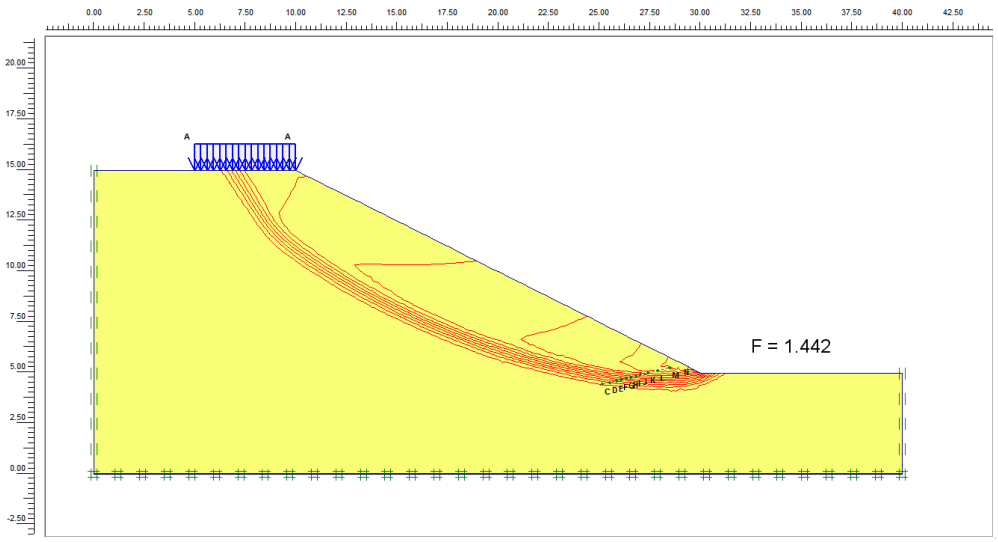

Figure A.7: Factor of safety and a contour plot of the displacements obtained with 15-node elements in Plaxis

The factor of safety obtained by additional mesh refinements is given in Table A.3. It can be seen that the mesh refinements has no significant impact on the factor of safety.

Table A.3: The factor of safety obtained by different meshes with 15-node elements

Mesh refinement	Element nr.	D.o.f. nr.	Avg. element size	Factor of safety
1	57	1030	3240 mm	1,481
2	157	2678	1950 mm	1,450
3	336	5618	1340 mm	1,443
4	747	12286	895 mm	1,442
5	1556	25378	620 mm	1,439
6	6713	108366	299 mm	1,439

It is shown in Figure A.8 that the 15-node elements provides a higher convergence rate than the 6-node elements. The convergence is achieved by only 1556 elements and 2556 d.o.f. with the mesh of 15-node elements, whereas convergence is not achieved before 29309 elements and 118312 d.o.f. with the mesh of 6-node elements.

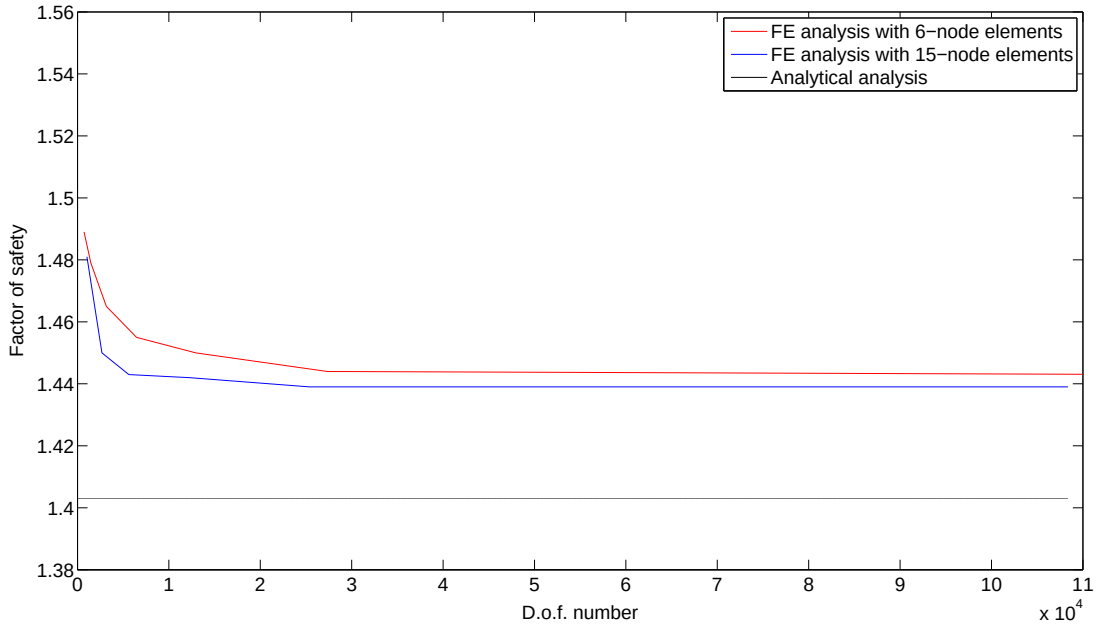

Figure A.8: Convergence rate for FE and LE analyses.

Compared to the factor of safety obtained from the LE based software, as shown in Figure A.8, the factor is overestimated when using a coarse mesh of 6-node elements, whearas the factor is more accurately estimated when using a coarse mesh of 15-node elements. Thus, a mesh of 15-node elements provides reasonable accuracy even for coarse meshes.

Further studies of the convergence and accuracy in analysis with 6-node and 15-node elements is necessary, to validate the statement of the 15-node elements.

A.2 Bearing capacity of a strip footing

In this section the bearing capacity of a strip footing is calculated analytical and then numerical in the software Plaxis. In the numerical calculations 6-node and 15-node elements is used to generate the meshes of the footing. The purpose is to show that the 15-node element provides a better convergens toward the bearing capacity calculated analytically.

A.2.1 Geometry and material parameters

The strip footing considered has a width of b = 1 m and is placed on a soil soil layer of 5 m thickness as shown in Figure A.9. The footing is considered rough. Appendix **??**

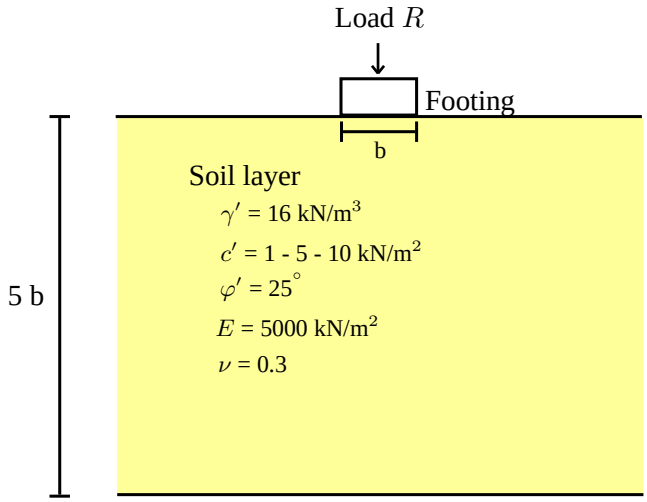

Figure A.9: Geometry of strip footing

In the calculations of the bearing capacity an associated Mohr-Coulomb material is assumed, since calculations with a non-associated Mohr-Coulomb material with diverse values of the friction angle and dilation angle often cause convergence problems. In this case the soil material is consiting of clay with different cohesion values. The material parameter of the clay is given in Table A.4.

Table A.4: Material parameters of the soil layer.

		Clay	
Material model	Model	Mohr-Coulomb	-
Type of material behaviour	Type	Drained	-
Parameters			
Soil unit weight above p.l.	γ'	16	kN/m^3
Cohesion	c'	varied 5 - 10 - 50	kN/m^2
Friction angle	φ'	25	°
Dilatancy angle	ψ'	25	°
Young's modulus	E'	5000	kN/m^2
Poisson's ratio	ν'	0.33	-
Interface stregth	R_{inter}	rough	-

A.2.2 Analytical solutions

The bearing capacity of the strip footing is calculated by Terzaghi's equation [9], which implies an associated perfect plastic Mohr-Coulomb material model:

$$p = \frac{R'}{A'} = \frac{1}{2}\,\gamma'\,b'\,N_\gamma\,s_\gamma\,i_\gamma + q'\,N_q\,s_q\,i_q\; + c'\;N_c\,s_c\,i_c \tag{A.4}$$

where,

R' is the effective vertical bearing capacity,
A' is the effective area of the footing,
b' is the effective width of the footing,
γ' is the effective density of the soil under the footing,

q' is the effective surface load of the soil next to the footing,
c' is the effective cohesion of the soil,
N_γ, N_q and N_c are bearing capacity factors,
s_γ, s_q and s_c are shape factors, and
i_γ, i_q and i_c are gradient factors,

The effective dimensions of the footing are equal to the geometric dimensions, since the load applied to the footing is uniformly distributed. It is assumed that the length of the footing is infinite in relation to the width, $b' \ll l'$. Thus, the area of the footing is given by:

$$A' = 1\,m^2/m \tag{A.5}$$

The dimensionless factors for the bearing capacity N_γ, N_q and N_c are all functions of the friction angle, φ. These factors have a considerable influence on the the bearing capacity. The exact values of N_q and N_c can be determined using Prandtl's equations:

$$N_q = e^{\pi \cdot tan(\varphi)} \cdot \frac{1 + sin(\varphi)}{1 - sin(\varphi)} \tag{A.6}$$

$$N_c = \frac{N_q - 1}{tan(\varphi)} \tag{A.7}$$

Different methods of determination have been proposed for the value N_γ. Most of these methods are based on numerical solutions of the load-deformation path of failure. Referring to the geotechnical textbook [9] the factor N_γ can be determined by the equation:

$$N_\gamma = \frac{1}{4} \cdot \Big((N_q - 1) \cdot cos(\varphi) \Big)^{\frac{3}{2}} \tag{A.8}$$

Referring to Eurocode [1] the factor N_γ can be determined by the equation:

$$N_\gamma = 2 \cdot (N_q - 1) \cdot tan(\varphi) \tag{A.9}$$

Recently the exact value of N_γ has been determined for both rough and smooth footings by Martin, see [16] and [17]. The different values of N_γ are stated in Table A.5.

The shape factors s_γ, s_q and s_c are calculated by the expressions [9]:

$$s_\gamma = 1 - 0.4 \cdot \frac{b'}{l'} \tag{A.10}$$

$$s_q \approx s_c \approx 1 - 0.2 \cdot \frac{b'}{l'} \tag{A.11}$$

The gradient factors i_q, i_c and i_γ are calculated by:

$$i_q = i_c = 1 - \frac{H}{V + A' \cdot c' * cot(\varphi)} \tag{A.12}$$

$$i_\gamma = i_q^2 \tag{A.13}$$

where,

H is the horixontal load,
V is the vertical load,
c' is the effective cohesion,
φ is the friction angle.

Since it is assumed that $b' \ll l'$ for a strip footing, the shape factors and gradients factors are all equal to 1.
The different values of the bearing capacity factors N_c, N_c and N_γ are stated in Table A.5, and the matching bearing capacity is calculated using equation Eq. A.4 with different values of the cohesion.

Table A.5: Bearing capacities calculated by Eq. A.4 referring to geotechnical textbook [9]

c'	5	10	50	[kN/m^2]
φ'	25	25	25	[°]
N_q	10.6621	10.6621	10.6621	[-]
N_c	20.7205	20.7205	20.7205	[-]
N_γ	6.47829	6.47829	6.47829	[-]
Q	155.43	259.03	1087.85	[kN/m^2]

Table A.6: Bearing capacities calculated by Eq. A.4 referring to Eurocode 7 [1]

c'	5	10	50	[kN/m^2]
φ'	25	25	25	[°]
N_q	10.6621	10.6621	10.6621	[-]
N_c	20.7205	20.7205	20.7205	[-]
N_γ	9.01102	9.01102	9.01102	[-]
p	175.69	279.29	1108.11	[kN/m^2]

Table A.7: Bearing capacities calculated by Eq. A.4 referring to Martins [17]

c'	5	10	50	[kN/m^2]
φ'	25	25	25	[°]
N_q	10.6621	10.6621	10.6621	[-]
N_c	20.7205	20.7205	20.7205	[-]
N_γ	6.49131	6.49131	6.49131	[-]
p	155.53	259.14	1087.96	[kN/m^2]

It is seen from Table A.5 - Table A.7 that the methods of determination for the value N_γ has an influence on the bearing capacity, particularly in the case the low cohesion soil. The influnce becomes more significant if the soil weight or the width of the footing is lager.

Comparing with the exact value of N_γ determined by Martins, it is seen that value is more correct when using equation Eq. A.9 from the geotechnical textbook than when Eq. A.9 from Eurocode is used.

The bearing capacities calculated with the exact value of N_γ determined by Martins is used to compare with the finite element analysis performed in the following section. It is assumed that the bearing capacities calculated analytically is conservative compared with the results from the finite element analysis.

A.2.3 Finite element solutions

In this section the bearing capacity of the strip footing is carried out in the software Plaxis. The settlement of the footing is in Plaxis simulated by a forced uniform displacement of $u = 1$ m applied to the nodes at top of the soil domain instead of modelling the footing itself. This approach lead to a very simple model of the soil domain, shown in Figure A.10.a. Due to symmetry only half of the soil domain is modelled in order to reduce the computational costs.

Both the 6-node and 15-node elements is used to generate the finite element meshes of the soil domaine. The vertical sides of the mesh are restrained in the horizontal direction, while the base of the mesh is restrained in the vertical and the horizontal direction. An example of the 15-node element mesh is seen in Figure A.10.b.

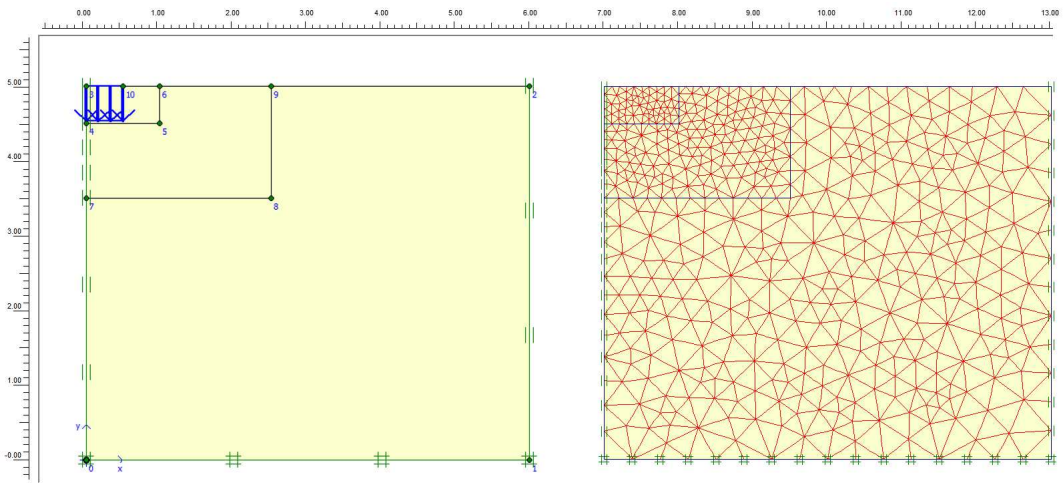

Figure A.10: (a) The considered soil domain with boundary conditions, (b) Example of a mesh with 7905 elements and 3671 d.o.f.

The bearing capacity of the footing is calculated for an associated Mohr-Coulomb condition.

Results

The bearing capacity for the footing is evident from the load-displacement curves computed in Plaxis. On the same curves the bearing capacity calculated analytically is displayed.

The load-displacement curves for the footing with a cohesion of 5, 10 and 50 kN/m^2 is shown in Figure A.11, Figure A.12 and Figure A.12 for meshes with 6-node and 15-node elements, respectively.

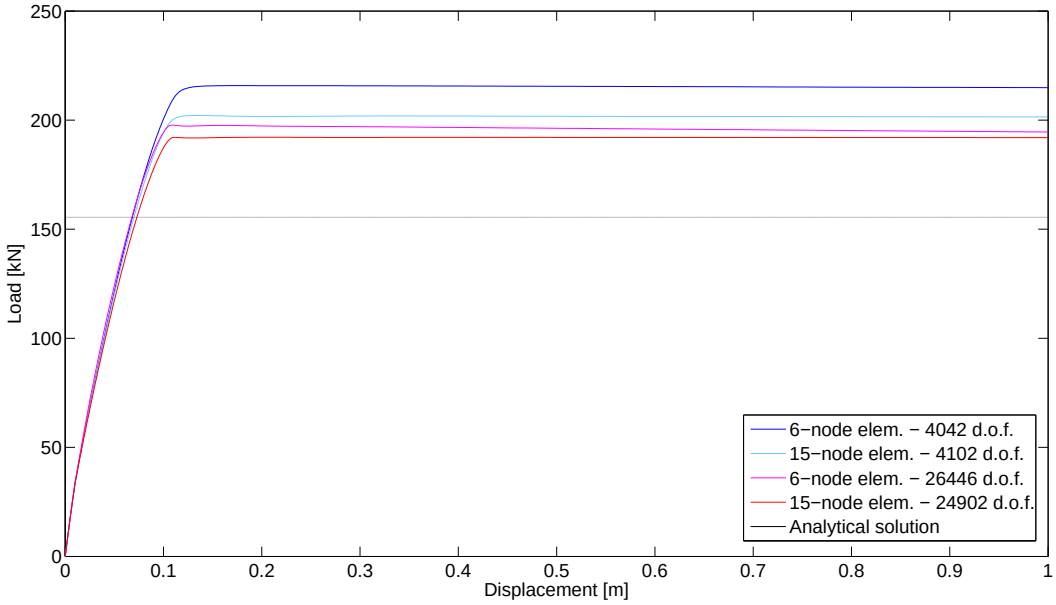

Figure A.11: The load-displacement curve from calculations with a cohesion of 5 kN/m^2.

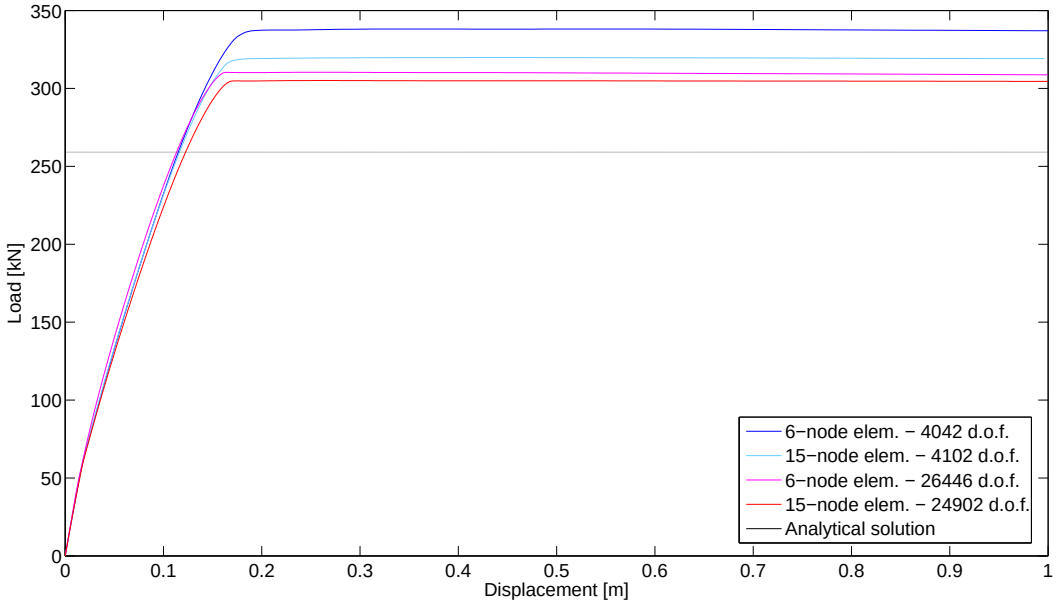

Figure A.12: The load-displacement curve from calculations with a cohesion of 10 kN/m^2.

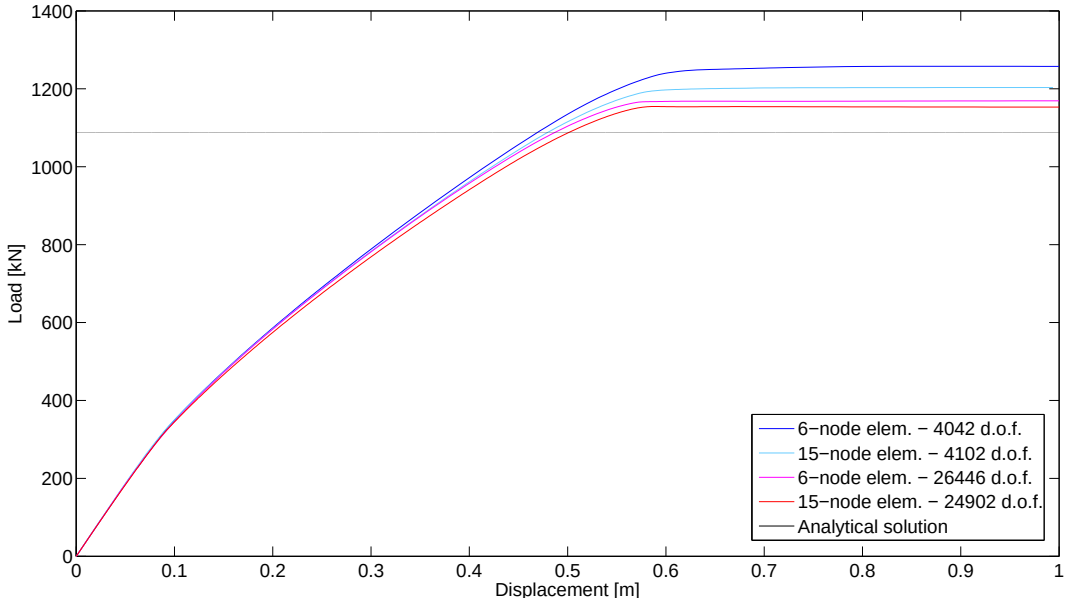

Figure A.13: The load-displacement curve from calculations with a cohesion of 50 kN/m^2.

It is evident by Figure A.11, Figure A.12 and Figure A.12 that the bearing capacity increases with the cohesion. Compared to the analytical solutions it is clear that the finite element solution in Plaxis overestimate the bearing capacity. The bearing capacity is more accurately estimated when using a mesh of 15-node elements instead of 6-node elements. Thus, a mesh of 15-node elements provides reasonable accuracy even for coarse meshes when considering that the analytical solutions is conservative.

In Figure A.14, Figure A.15 and Figure A.16 the convergence of the bearing capacity is displayed for 6- and 15-node elements, respectively.

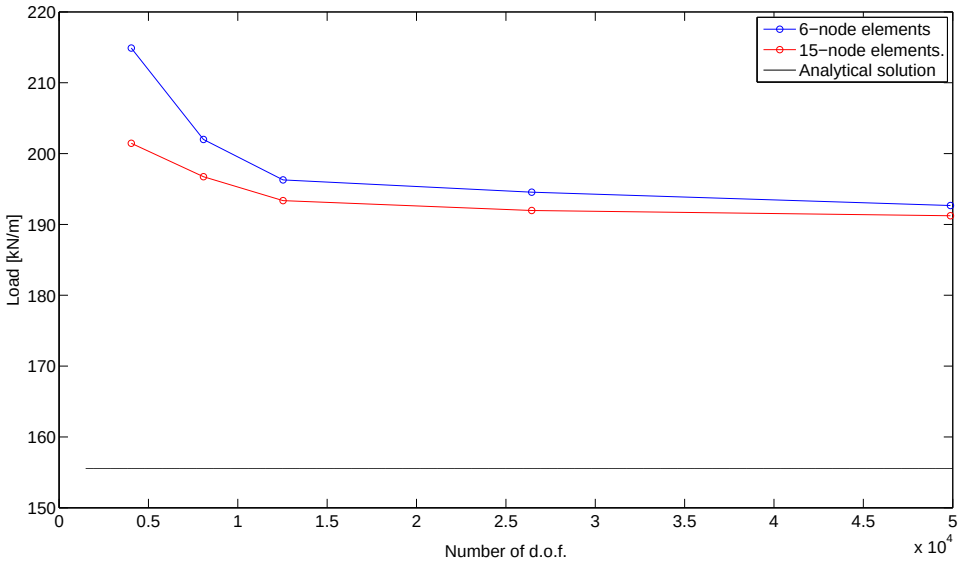

Figure A.14: The convergence of the bearing capacity for a cohesion of 5 kN/m^2.

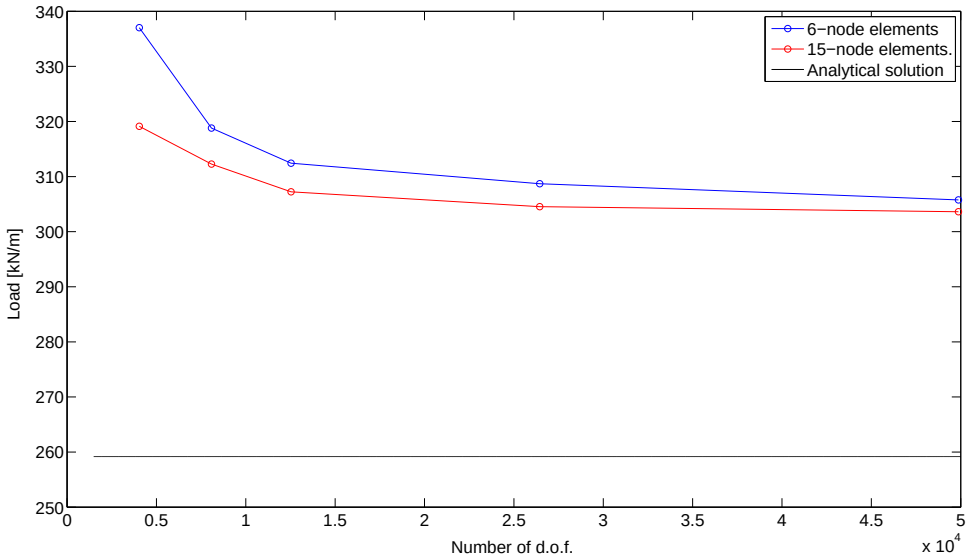

Figure A.15: The convergence of the bearing capacity for a cohesion of 10 kN/m^2.

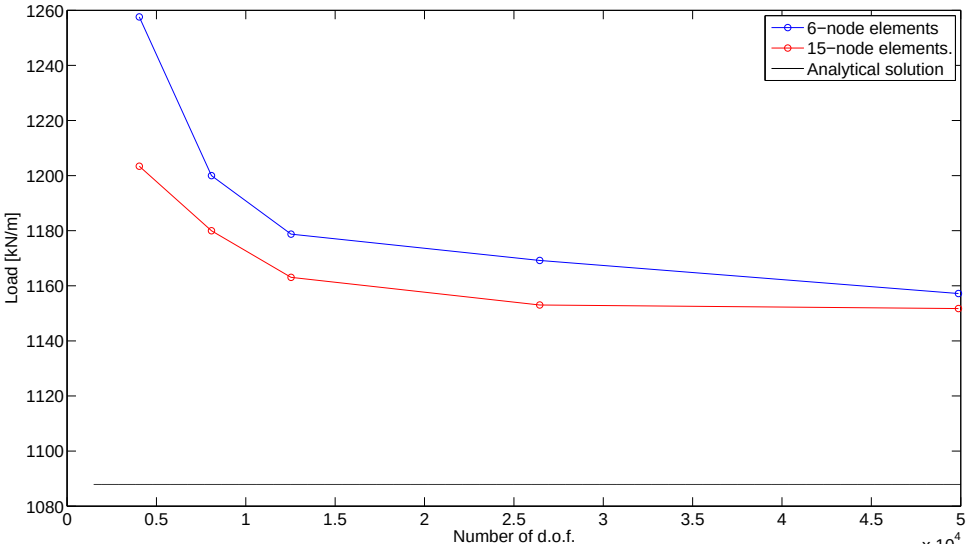

Figure A.16: The convergence of the bearing capacity for a cohesion of 50 kN/m^2.

Compared to the bearing capacity calculated analytically the solution obtained with a mesh of 6-node element has a slower convergence than the solutions with a mesh of 15-node elements. This validate the previous results in Section A.1.3.

B Computation of the stiffness matrix

To compute the element stiffnes matrix $[ElemK]$ the strain-displacement matrix $[B]$ is derived from the shape functions. $[B]$ is defined by:

$$[\mathrm{B}] = \begin{bmatrix} \frac{\partial N_i}{\partial x} & 0 & \frac{\partial N_{i+3}}{\partial x} & 0 & \frac{\partial N_{i+6}}{\partial x} & 0 & \frac{\partial N_{10}}{\partial x} & 0 \\ 0 & \frac{\partial N_i}{\partial y} & 0 & \frac{\partial N_{i+3}}{\partial y} & 0 & \frac{\partial N_{i+6}}{\partial y} & 0 & \frac{\partial N_{10}}{\partial y} \\ \frac{\partial N_i}{\partial y} & \frac{\partial N_i}{\partial x} & \frac{\partial N_{i+3}}{\partial y} & \frac{\partial N_{i+3}}{\partial x} & \frac{\partial N_{i+6}}{\partial y} & \frac{\partial N_{i+6}}{\partial x} & \frac{\partial N_{10}}{\partial y} & \frac{\partial N_{10}}{\partial x} \end{bmatrix}$$

where $i = 1, 2, 3$. The chain rule for differentiation gives:

$$\frac{\partial N_i}{\partial x} = \frac{\partial N_i}{\partial \lambda_1}\frac{\partial \lambda_1}{\partial x} + \frac{\partial N_i}{\partial \lambda_2}\frac{\partial \lambda_2}{\partial x} + \frac{\partial N_i}{\partial \lambda_3}\frac{\partial \lambda_3}{\partial x} \tag{B.2}$$

$$\frac{\partial N_i}{\partial y} = \frac{\partial N_i}{\partial \lambda_1}\frac{\partial \lambda_1}{\partial y} + \frac{\partial N_i}{\partial \lambda_2}\frac{\partial \lambda_2}{\partial y} + \frac{\partial N_i}{\partial \lambda_3}\frac{\partial \lambda_3}{\partial y} \tag{B.3}$$

The derivative of the area coordinates is given by the area of the element and the adjacent line to the corner node in question:

$$\frac{\partial \lambda_i}{\partial x} = \frac{1}{2A} l_{i,y}$$

$$\frac{\partial \lambda_i}{\partial y} = \frac{1}{2A} l_{i,x}$$

For the corner nodes, the shape function differentiated with respect to the area coordinates is:

$$\frac{\partial N_i}{\partial \lambda_i} = 6\,\lambda_i^2 + 2\,\lambda_j^2 + 2\,\lambda_k^2 + 3\,\lambda_j\,\lambda_k - 1$$

$$\frac{\partial N_i}{\partial \lambda_j} = 4\,\lambda_i\,\lambda_j + 3\,\lambda_i\,\lambda_k$$

$$\frac{\partial N_i}{\partial \lambda_k} = 4\,\lambda_i\,\lambda_k + 3\,\lambda_i\,\lambda_j$$

For the midside nodes, the derivatives of the translational shape function with respect to area coordinates are:

$$\frac{\partial N_{i+3}}{\partial \lambda_i} = -12\,\lambda_j\,\lambda_k + 4\,\lambda_j$$

$$\frac{\partial N_{i+3}}{\partial \lambda_j} = -12\ \lambda_i\ \lambda_k + 4\ \lambda_i$$

$$\frac{\partial N_{i+3}}{\partial \lambda_k} = -12\ \lambda_i\ \lambda_j$$

And the derivatives of the gradient shape function with respect to area coordinates are:

$$\frac{\partial N_{i+6}}{\partial \lambda_i} = l_k\ (4\ \lambda_i\ \lambda_j - 2\ \lambda_j^2)$$

$$\frac{\partial N_{i+6}}{\partial \lambda_j} = l_k\ (2\ \lambda_i^2 - 4\ \lambda_i\ \lambda_j)$$

$$\frac{\partial N_{i+6}}{\partial \lambda_k} = 0$$

Finally, the shape function for the center node is also differentiated with respect to area coordinates:

$$\frac{\partial N_{i+9}}{\partial \lambda_i} = 27\ \lambda_j\ \lambda_k$$

$$\frac{\partial N_{i+9}}{\partial \lambda_j} = 27\ \lambda_k\ \lambda_i$$

$$\frac{\partial N_{i+9}}{\partial \lambda_k} = 27\ \lambda_i\ \lambda_j$$

These expressions are all substituted into Eq. B, which then leads to the computation of the element stiffness matrix $[K]$:

$$[K] = \int [B]^T [D][B] dV \tag{B.4}$$

where $[D]$ is the constitutive matrix.

This element stiffness matrix is a 20-by-20 matrix corresponding to the 20 d.o.f. internal to the element. Before assembling the element stiffness matrices into the global system, the 8 d.o.f. that only works within the element should be condensed.

C Linear tests of the extended element

The linear tests presented in this appendix is conducted in order to validate the implementation of the extended element (EXT) and the full extended element (F-EXT) in the finite element code in Matlab. The tests performed include simple patch tests, Cook's membrane test and strain energy test. These tests makes use of most of the parameters which influences the element accuracy. Parameters which influences accuracy are loading, element geometry, test geometry, material properties etc.

Inaccuracies of the element can occur by the presence of spurious modes induced of inadequate connections of elements, rank faults e.g. in connection with d.o.f., locking effects, elementary defects like rigid body motion etc. [11]. The patch tests should ensure that these defects is not present.

C.1 Patch test

The first test performed is a simple patch test originally presented by Irons (1964). This test verifies whether the extended element can provide a constant state of strain/stress. Meeting this requirement is necessary to guarantee that an arbitrary mesh of these elements will converge towards exact results if the mesh is refined sufficiently [11].

The patch test is performed using a simple finite element model, that is an assemblage of elements, with one of the nodes internal to the model. In this case the assemblage of elements forms a square model with the side length 10, as shown in Figure C.1.

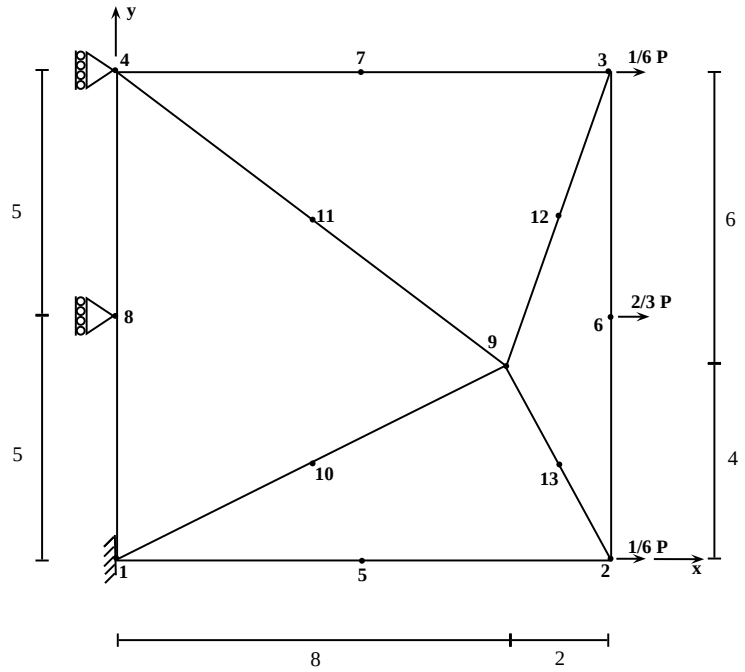

Figure C.1: Geometry, constraints and loads of the patch.

The rigth side of the model is loaded by a constant traction in the x-direction. For a model with side length 10 and a traction of 1 unit per length, the nodal loads are 1/6 at the corners and 2/3 at the midside, according to Section 2.3. The left side of the model is restrained in the x-direction and the lower left corner is also restrained in the y-direction. These restraints prevent rigid body motion and ensure that a correct solution to the constant strain/stress state may be obtained.

If the patch test is considered as a linear elastic problem with isotropic material properties, Young's modulus $E = 1$ and Poisson's ratio $\nu = 0$, the expected results of a plane stress solution are displacements:

$$u = 0.1\,x \quad ; \quad v = 0.0$$

strains

$$\varepsilon_x = \frac{\partial u}{\partial x} = 0.1 \quad ; \quad \varepsilon_y = \frac{\partial v}{\partial y} = 0.0$$

and stresses

$$\sigma_x = E \cdot \varepsilon_x = 0.1 \quad ; \quad \sigma_y = E \cdot \varepsilon_y = 0.0$$

The results of displacements and stresses computed in each node is given in Table C.1. Due to the proportionality between strains and stresses, only the stresses are computed. It is seen that the expected results are obtained.

Table C.1: Results of the patch test for the extended element, $E = 1$ and $\nu = 0$.

Node	u	v	σ_x	σ_y
1	0.000	0.000	0.100	0.000
2	1.000	0.000	0.100	0.000
3	1.000	0.000	0.100	0.000
4	0.000	0.000	0.100	0.000
5	0.500	0.000	0.100	0.000
6	1.000	0.000	0.100	0.000
7	0.500	0.000	0.100	0.000
8	0.000	0.000	0.100	0.000
9	0.800	0.000	0.100	0.000
10	0.400	0.000	0.100	0.000
11	0.400	0.000	0.100	0.000
12	0.900	0.000	0.100	0.000
13	0.900	0.000	0.100	0.000

Figure C.2 illustrates that correct displacements and stresses in x-direction are obtained everywhere in the patch field.

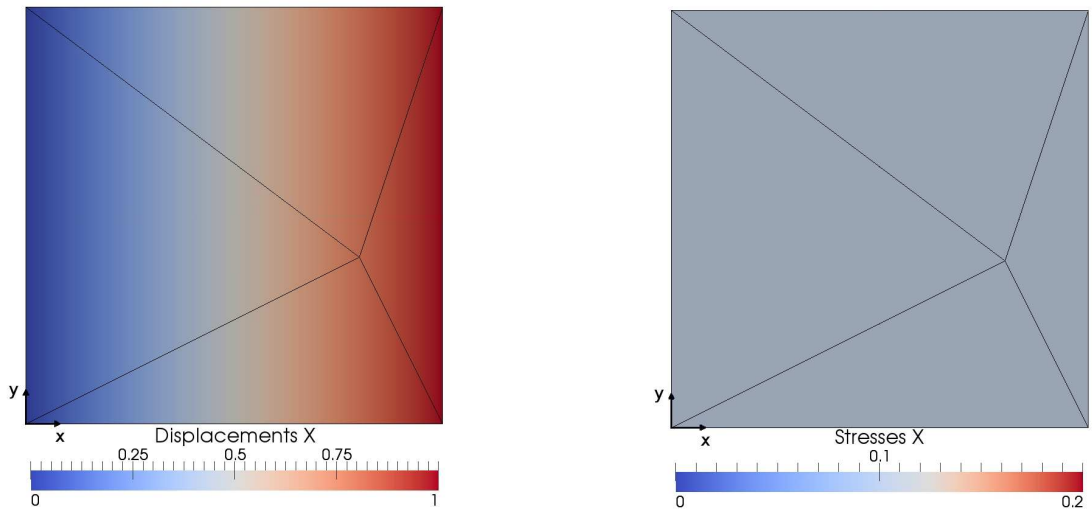

Figure C.2: Displacement u_x and stress σ_x.

Both the EXT element and F-EXT element is able to display a constant state of strains/stresses and thereby pass the patch test. It is possible for an element to pass the patch test even though it is unstable. Provided that the element is stable it is able to exhibit rigid body motion without strains/stresses, states of constant strains/stresses, and compatibility between elements [11]. These requirement is necessary to guarantee convergence. Accordingly, the patch test is also applied to verify stability.

C.2 Stability

A stability test can be performed by comparison of nodal displacements from the previous patch test with nodel displacement from a slightly higher load. If the displacements change drastically, the element is unstable.

A load 1 % higher than the load in the previous test is applied. The nodal displacements are found to be exactly 1 % higher, as shown in Table C.2. This is consistent with the load applied, and since the displacement does not change drastically, the extended element passes this stability test.

Table C.2: Results for the patch test with a slightly higher load.

Node	u_x	u_y	σ_x	σ_y
1	0.000	0.000	0.101	0.000
2	1.010	0.000	0.101	0.000
3	1.010	0.000	0.101	0.000
4	0.000	0.000	0.101	0.000
5	0.505	0.000	0.101	0.000
6	1.010	0.000	0.101	0.000
7	0.505	0.000	0.101	0.000
8	0.000	0.000	0.101	0.000
9	0.808	0.000	0.101	0.000
10	0.404	0.000	0.101	0.000
11	0.404	0.000	0.101	0.000
12	0.909	0.000	0.101	0.000
13	0.909	0.000	0.101	0.000

Another way to test for instability is by computing the eigenvalues of [K] for the patch. When the patch is supported sufficiently to prevent rigid body motion, the eigenvalues should all be positive. In Table C.3 the eigenvalues for the patch are given. They are all positive, which thereby indicates that the stability of the extended element is satisfying.

Table C.3: Eigenvalues for the patch test of the extended element.

Eigenvalues	
9.0558	0.9336
5.9359	0.7092
5.3291	0.5063
4.5893	0.4727
3.6369	0.3815
3.2281	0.3619
2.9175	0.2636
2.3766	0.1447
2.0176	0.1362
1.4774	0.1323
1.3086	0.0000
1.2084	0.0000
1.0796	0.0000

The previous tests do not show how well the extended element performs in other applications. The element may in other applications provide a poor accuracy in a coarse mesh or provide a slow convergence. Thus, additional tests of the elements is performed with the intention to compare the performance of the element to the performance of the LST element.

C.3 Cook's membrane test

The following test performed is the well-known problem concerning Cook's membrane with different meshes. This test verifies whether the extended element (EXT) can provide a better accuracy and convergence rate for a linear elastic problem, than the LST element [6].

The geometry of Cook's membrane is shown in Figure C.3 with two different meshes, and it appears that the problem include both shear and bending combined with the geometry distortion. The rigth side of the model is loaded by a constant traction of P=1 in the y-direction, and the left side of the model is restrained in the x- and y-direction. The modulus of elasticity is $E = 1$ and Poisson's ratio is $\nu = 0.333$.

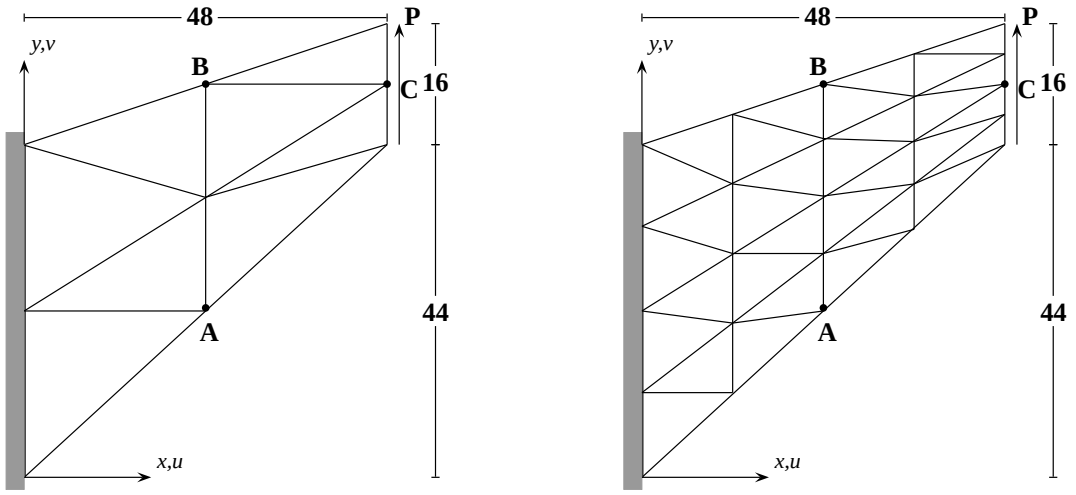

Mesh 2x2. Mesh 4x4.

Figure C.3: Cook's membrane with mesh 2x2 and mesh 4x4.

The vertical displacement at point C and the maximum and minimum principal stress at the points A and B, respectively, are compared for the elements mentioned in Section 2. There is no known theorictical solutions, but the results provided by Bergan & Felippa (1985) [18] and Felippa & Alexander (1992) [4] are used for comparison purposes.

The displacement results computed for different mesh sizes are listed in Table C.4 for the LST element, the EXT element and the F-EXT element. These results should be compared to the results provided by Felippa & Alexander (1992).

Table C.4: Displacement in point C for Cook's membrane.

Mesh Mesh	LST	EXT 12x12	FULL-EXT 20x20 comp	FULL-EXT 20x20 incomp
2X2	23.301	27.299	24.552	27.299
4X4	23.856	24.938	24.067	24.938
8X8	23.934	24.211	23.978	24.211
16X16	23.951	24.007	23.968	24.007
20X20	23.955	23.977	23.967	23.977
24X24	23.958	23.974	23.967	23.974
28X28	23.958	23.974	23.967	23.974
32X32	23.958	23.978	23.967	23.978
Best known	23.95	23.95	23.95	

Displacements converge faster than stresses, and therefore the computed stresses is listed in Table C.5. These results should be compared to the results provided by Bergan & Felippa (1985).

Table C.5: Maximum and minimum stresses in points A and B for Cook's membrane.

	LST		EXT 12x12 comp		FEXT 20x20 comp	
Mesh	$(\sigma_{max})_A$	$(\sigma_{min})_B$	$(\sigma_{max})_A$	$(\sigma_{min})_B$	$(\sigma_{max})_A$	$(\sigma_{min})_B$
2X2	0.2311	-0.1908	0.2151	-0.1194	0.2444	-0.1939
4X4	0.2364	-0.2041	0.2172	-0.1609	0.2388	-0.2030
8X8	0.2369	-0.2042	0.2255	-0.1842	0.2371	-0.2036
16X16	0.2369	-0.2036	0.2305	-0.1932	0.2369	-0.2035
20X20	0.2369	-0.2036	0.2317	-0.1930	0.2369	-0.2035
24X24	0.2369	-0.2036	0.2325	-0.1947	0.2369	-0.2035
28X28	0.2369	-0.2036	0.2331	-0.1959	0.2369	-0.2035
32X32	0.2369	-0.2036	0.2335	-0.1983	0.2369	-0.2035
Best known	0.2359	-0.2012	0.2359	-0.2012	0.2359	-0.2012

Table C.6: Maximum and minimum stresses in points A and B for Cook's membrane.

	FEXT 20x20 incomp	
Mesh	$(\sigma_{max})_A$	$(\sigma_{min})_B$
2X2	0.2151	-0.1194
4X4	0.2172	-0.1609
8X8	0.2255	-0.1842
16X16	0.2305	-0.1932
20X20	0.2317	-0.1930
24X24	0.2325	-0.1947
28X28	0.2331	-0.1959
32X32	0.2335	-0.1983
Best known	0.2359	-0.2012

However, it is considered unfair to compare the results only by mesh sizes, due to the fact that it is not the actual size of the mesh that indicates a difference in the computational costs. Instead, it is the number of d.o.f. that indicates the costs, and the elements should

therefore be compared with respect to d.o.f.

In Figure C.4 and Figure C.5 the convergence of displacements of the point C with respect to d.o.f. are illustrated. Figure C.5 is a close-up of Figure C.4.

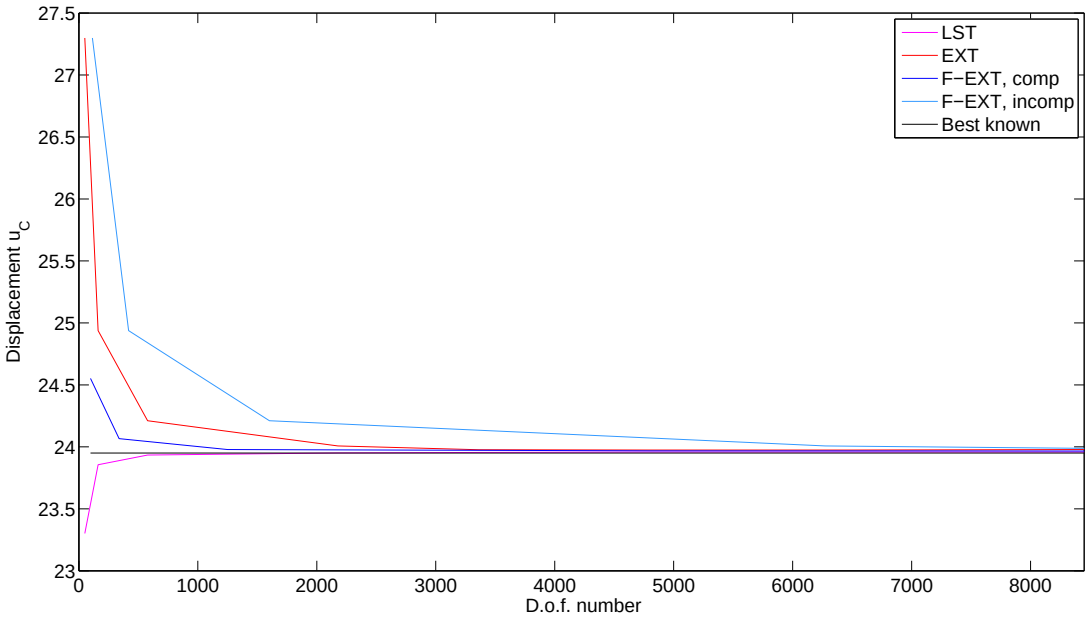

Figure C.4: Convergence of displacements u_C with respect to d.o.f.

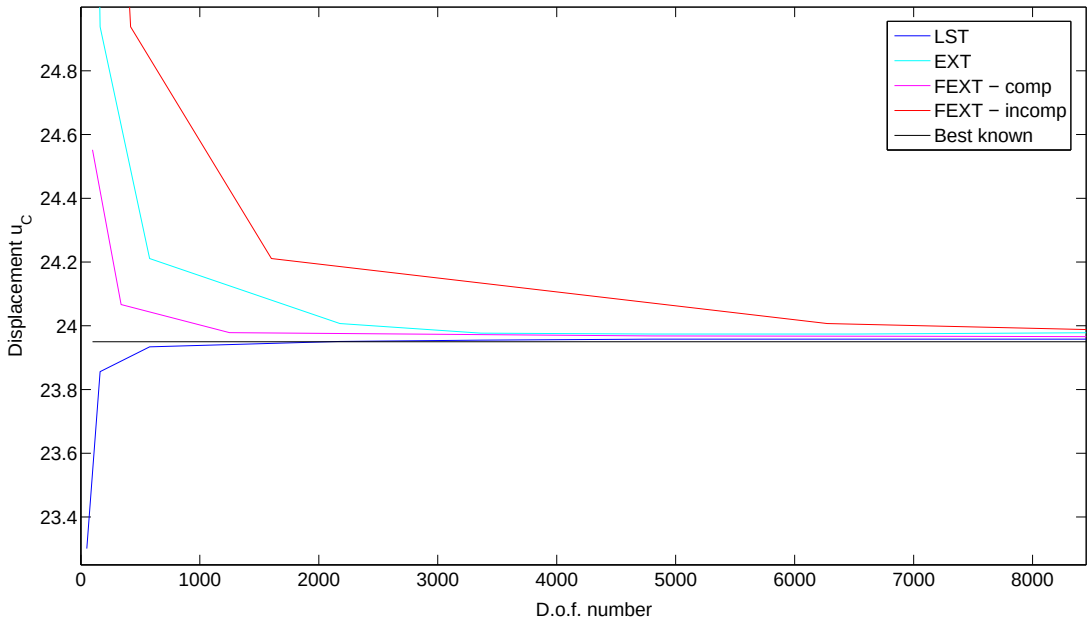

Figure C.5: Convergence of displacements u_C with respect to d.o.f., close-up.

When comparing the displacement results with the best known results, it is seen that the convergence of EXT element is poor compared to LST element. It is also evident that the displacements calculated by the EXT element is higher than the displacements calculated by the LST element. This indicates that the extended element is too flexible to provide accurate results in a linear analysis.

Likewise, it is seen that the convergence of the incompatible F-EXT element is poor compared to LST element. On the other hand it is seen that the compatible F-EXT element converges as fast as the LST element, and that the accuracy of the compatible F-EXT element is high even for coarse meshes. This is evident from the close-up on Figure C.5.

In Figure C.4 and Figure C.5 the convergence of maximum and minimum principal stresses in the points A and B are illustrated with respect to d.o.f.

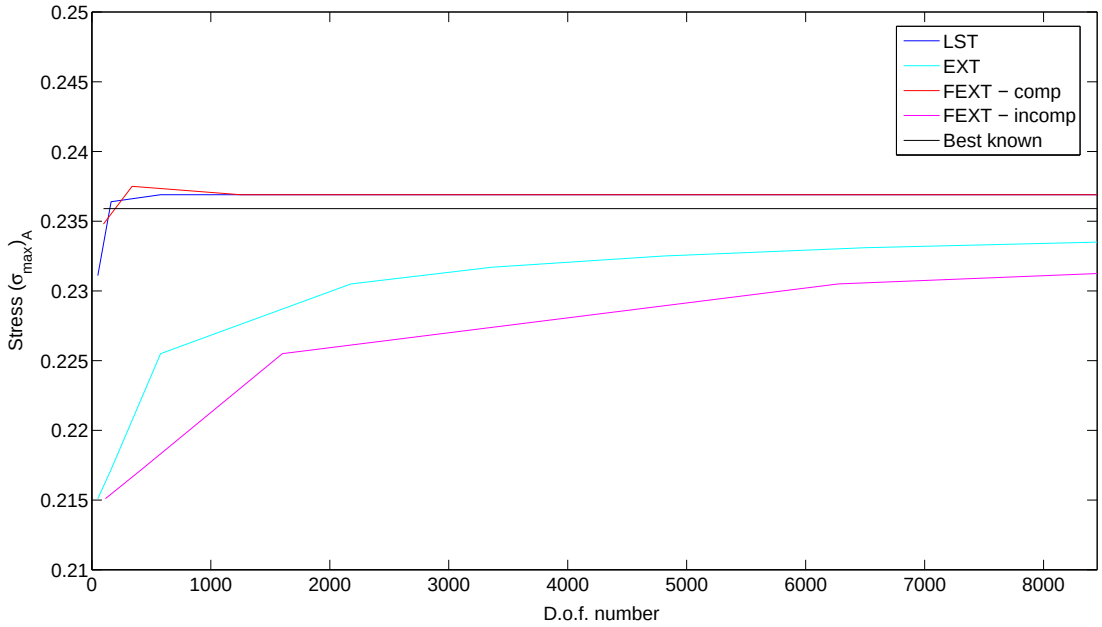

Figure C.6: Convergence of stress $(\sigma_{max})_A$ with respect to d.o.f.

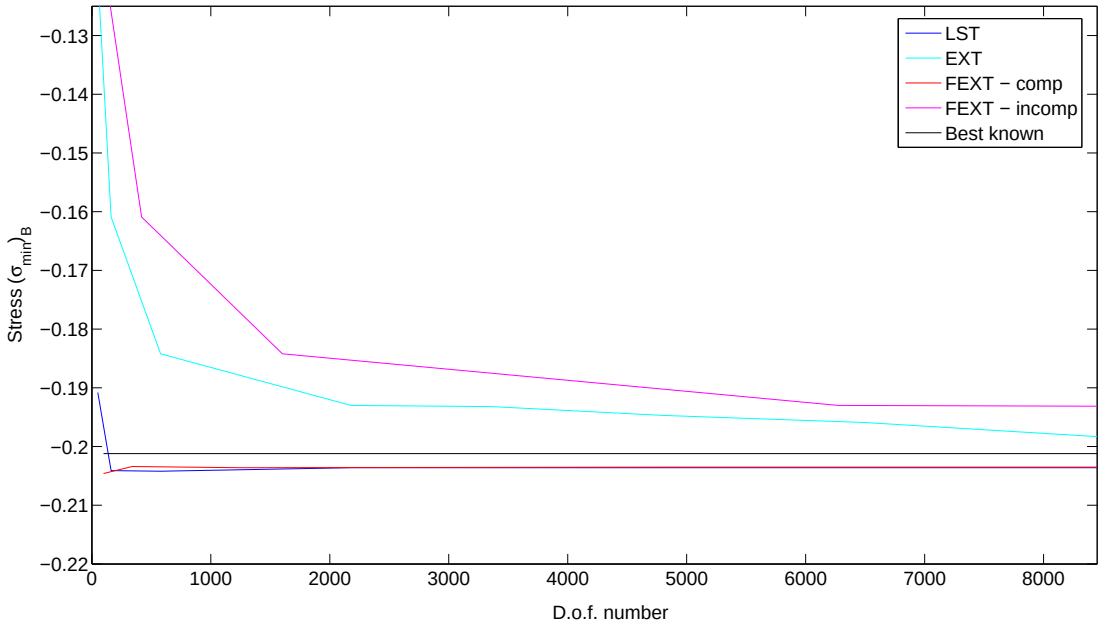

Figure C.7: Convergence of stress $(\sigma_{max})_B$ with respect to d.o.f.

Likewise, it is seen that the convergence of principal stresses computed for the EXT element and the incompatible F-EXT element is poor compared to LST. However, it is seen that the convergence of the principal stresses computed for compatible F-EXT is good compared to the LST.

C.4 Plat with a hole

The problem considered in the followings test is a plate with a circular hole, which is loaded by a force per unit area on its edge. The plate is shown in Figure C.8. The plate is assumed to be made of a linear elastic material, with the material parameters $E = 1$ and $v = 0.3$. Furthermore the plate is considered to be very thin, and thereby the tests can be solved for a plane stress state.

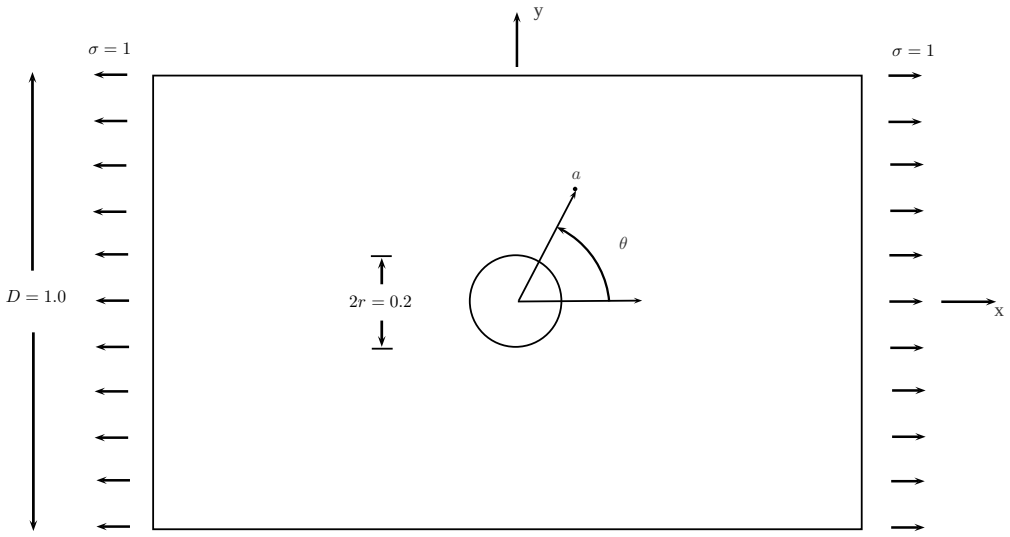

Figure C.8: Plate with a circular hole, loaded in tension.

The problem is solved numerical, and the results can be compared with the analytical solution given for a plate with an infinite length compared with the diameter for the hole, $2r$. The solution for the stress throughout the plate is given by:

$$\sigma_\theta = \frac{\sigma}{2}\left(1 + \frac{r^2}{a^2} - (1 + 3\frac{r^4}{2\,a^4})\,cos(2\,\theta)\right) \tag{C.1}$$

Large stresses occurs in a small, localized area around the hole, and the large stresses is referred to as stress concentrations. The maximum stress $\sigma_\theta = 3\sigma$ is localized at $a = r$ and $\theta = \pm 90°$, and the minimum stress $\sigma_\theta = -\sigma$ is localized at $a = r$ and $\theta = 0°$ and $180°$.

The problem is solved by using the different meshes, and three examples of the meshes are shown in Figure C.9. The meshes is generated so that the elements near the hole are finer than those further from the hole, in this way the stress concentration around the hole is better described. Due to the axis symmetry only a quarter of the plate is discretized into a mesh.

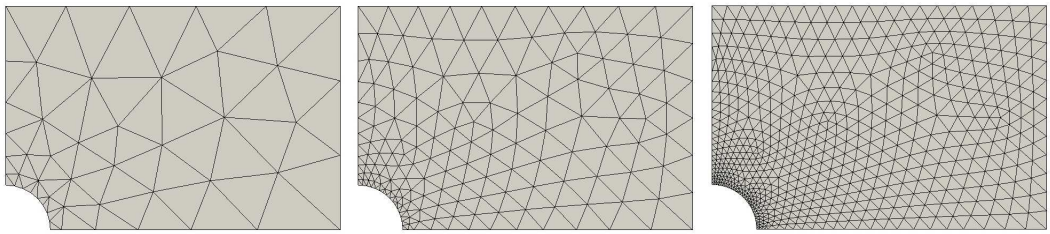

Figure C.9: Mesh 1 - 92 elements and 173 nodes, Mesh 2 - 328 elements and 633 nodes, Mesh 3 - 1152 elements and 4834 nodes

In Figure C.10 the convergence of the maximum stress $\{\sigma_x\}_{\theta=90^\circ}$ at the surface of the hole is displayed for LST element, EXT element, F-EXT compatible and incompatible elements. It appears that the convergence of the EXT and F-EXT elements is poor compared to the convergence of LST element. Furthermore problems with memory occurs in computation of the maximum stress with a very fine mesh of F-EXT incompatible elements.

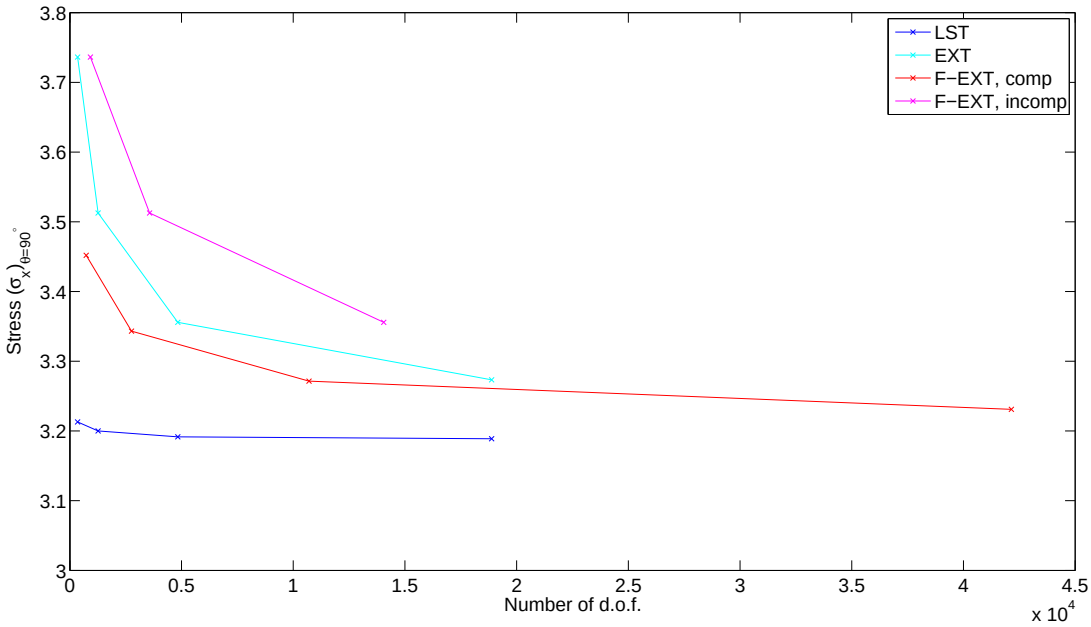

Figure C.10

Results of the problem solved with different meshes of LST elements, EXT elements, F-EXT compatible and incompatible elements are compared with the analytical solution of Eq. C.1. Therefore a plot of the tests data and the analytical solution of the normal stress along the vertical symmetry plane is displayed in Figure C.11, Figure C.12, Figure C.13.

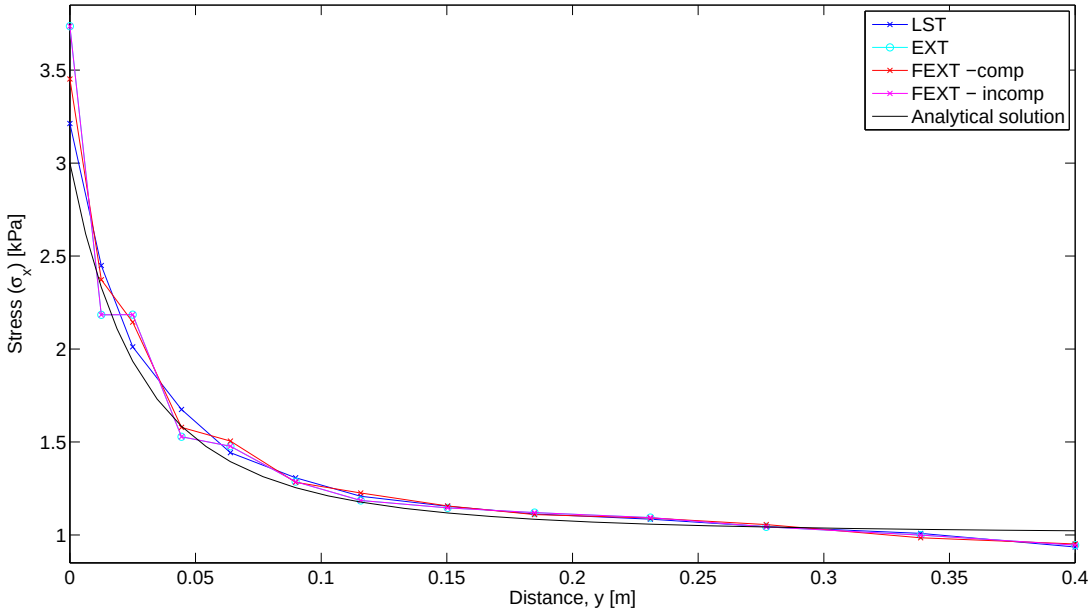

Figure C.11: Nomal stress σ_x along the vertical symmetry axis - mesh 1

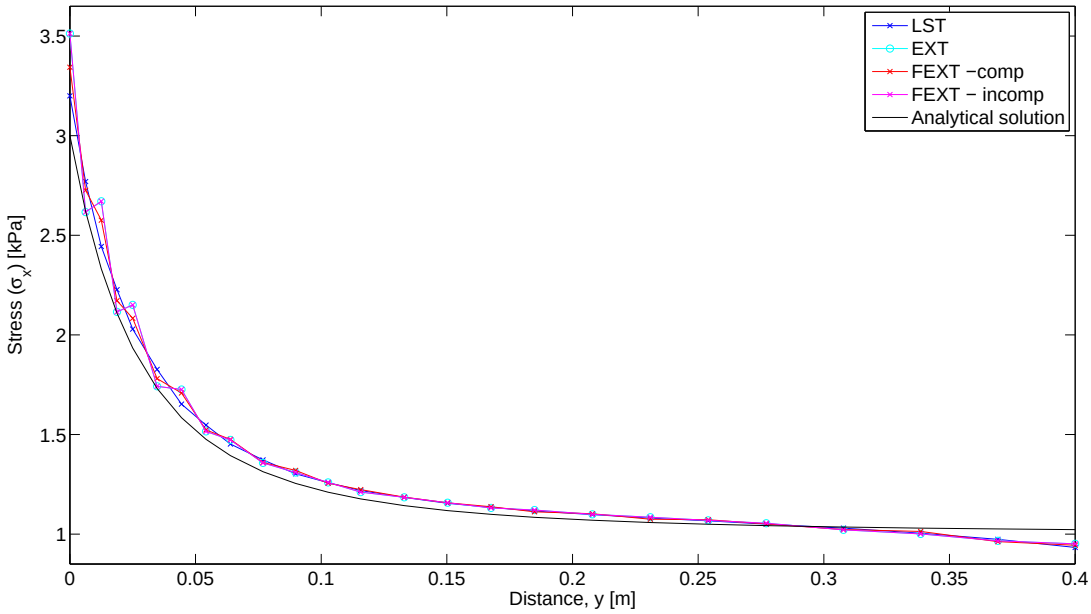

Figure C.12: Nomal stress σ_x along the vertical symmetry axis - mesh 2

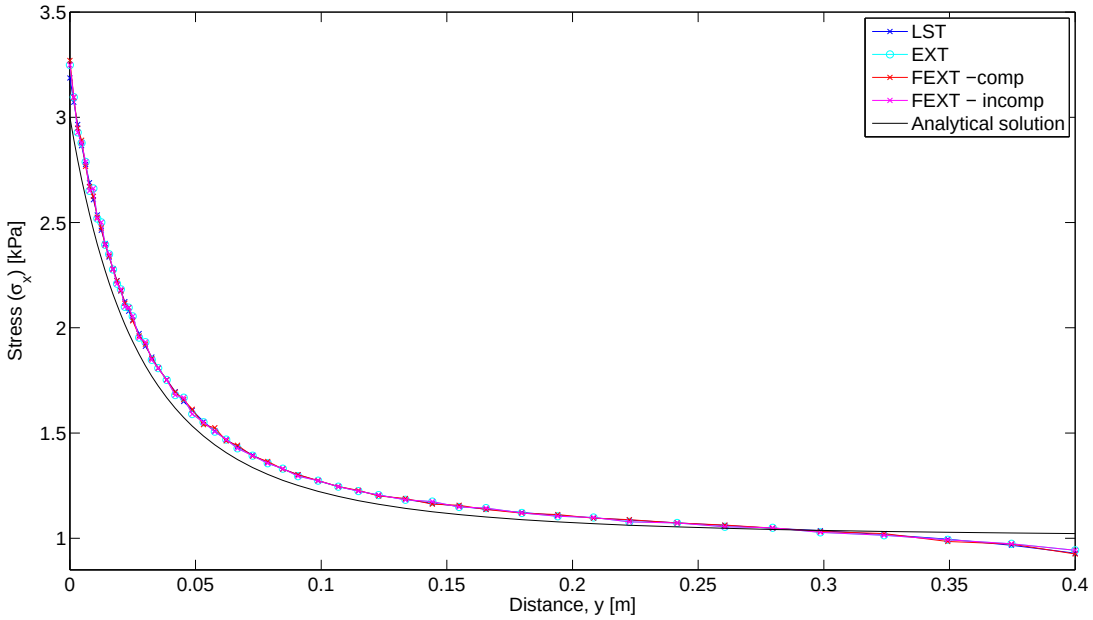

Figure C.13: Nomal stress σ_x along the vertical symmetry axis - mesh 3

When comparing the numerical test results with the analytical results, it is seen that the results are not completely accurate for the numerical tests. The tests results obtained with LST element is more accurate than the results obtained with EXT element, F-EXT compatible and incompatible element. It appear that the results obtained with the EXT element are equal to the results obtained with the F-EXT incompatible element, and therefore it is evident that the linear-elastic behavior of the EXT and the F-EXT incompatible element is the same.

Common for the EXT element, F-EXT compatible and incompatible element is that the influence of the gradients becomes significant for the stress results computed for a coarse mesh. The influence of the gradients is more significant for the the EXT and the F-EXT incompatible compared with the F-EXT compatible element. Only for a very fine mesh the influence of the gradients becomes insignificant.

The influence of the gradients becomes more significant in the area around the hole, where large stress concentrations occurs. This is evident from the close-up on Figure C.14, Figure C.15 and Figure C.16.

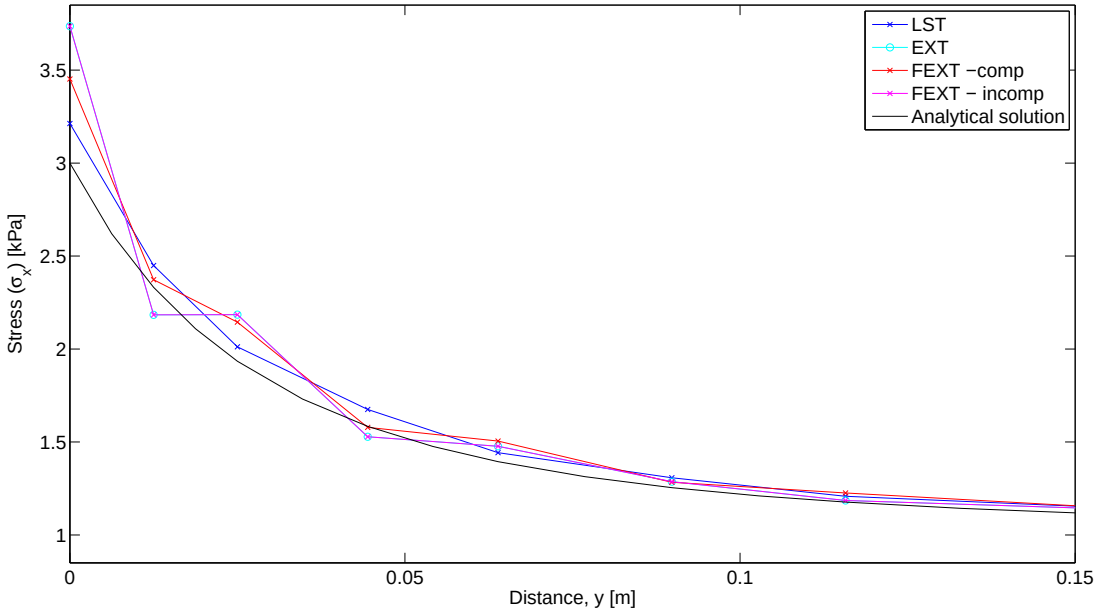

Figure C.14: Close-up of the stress along the vertical symmetry axis - mesh 1

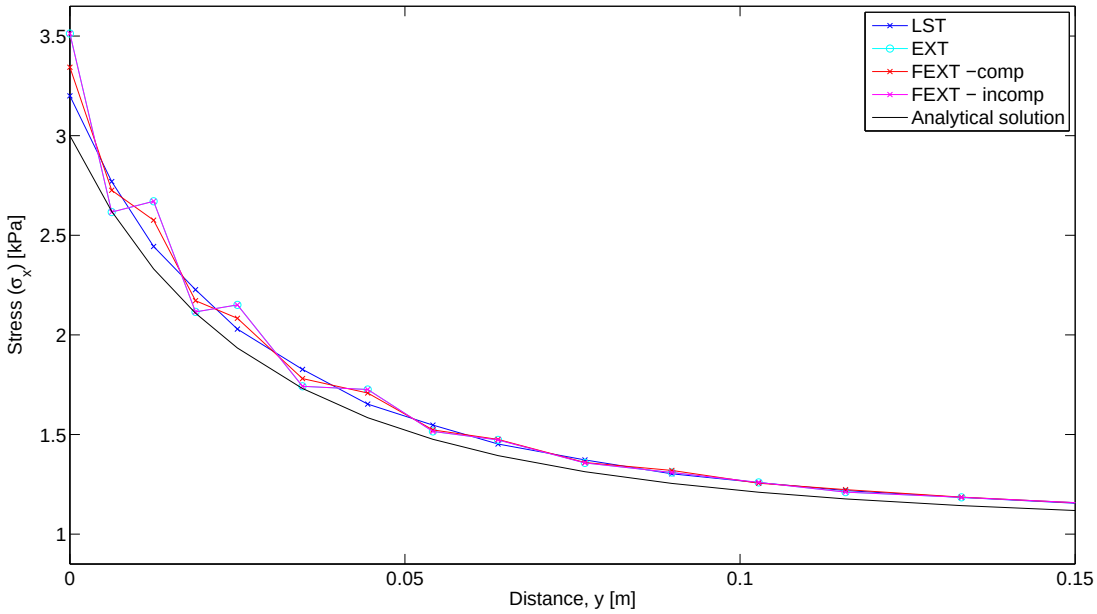

Figure C.15: Close-up of the stress along the vertical symmetry axis - mesh 2

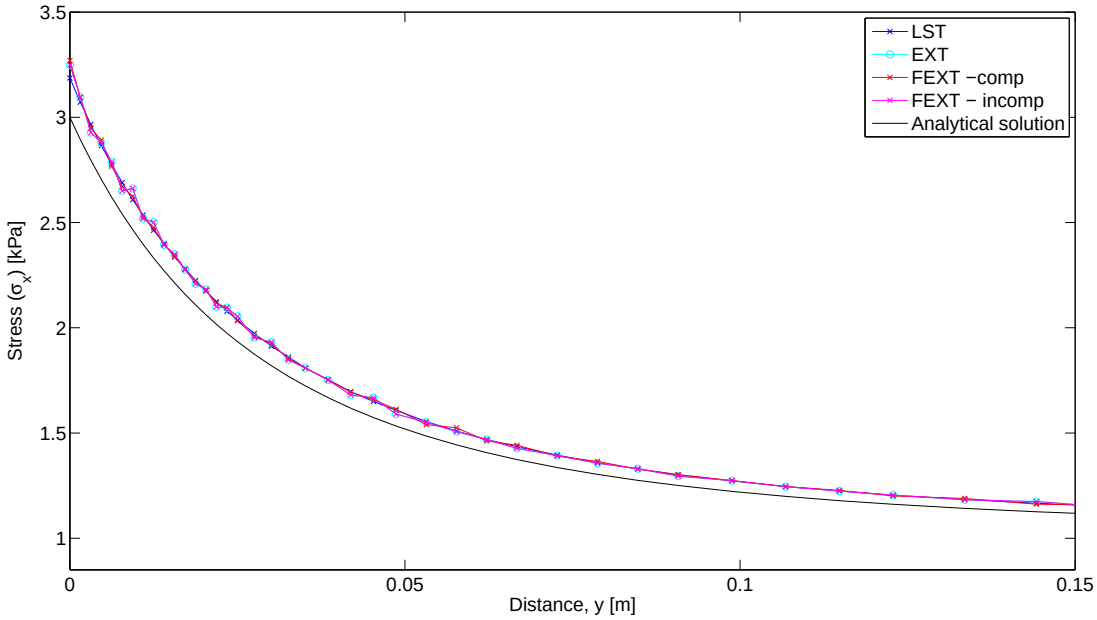

Figure C.16: Close-up of the stress along the vertical symmetry axis - mesh 3

C.5 Convergence of strain energy

In the previous tests, the displacement- and stress convergence rates has been described for specific nodes in a geometry. The convergence rate of one point may be very different from another point in the geometry. Accordingly, in the following academic example the convergence of the strain energy for the entire geometry is considered.

The geometry is shown in Figure C.17. For convenience, the length and width of the model are chosen to $L = 1$. Poisson's ratio is $\nu = 0.3$ and the modulus of elasticity is $E = 1$ [TJEK OP PÅ DET]. The mesh consists of 4 elements, as shown in Figure C.17a, and the mesh is to be refined 3 times. The first mesh refinement is illustrated in Figure C.17b. Displacements in each node is given by:

$$u = \sin(\frac{\pi\, x}{L}) \sin(\frac{\pi y}{L}) \qquad v = 0 \tag{C.2}$$

The exact solution is found by multiplying strains with stresses and integrating over the area of the geometry:

$$E_{exact} = \int_0^1 \int_0^1 \sigma_x \varepsilon_x + \sigma_y \varepsilon_y + \sigma_{xy} \gamma_{xy}\, dx\, dy = 2.7755 \tag{C.3}$$

To determine the strain energy of the numerical model, the internal load vectors for each element is calculated:

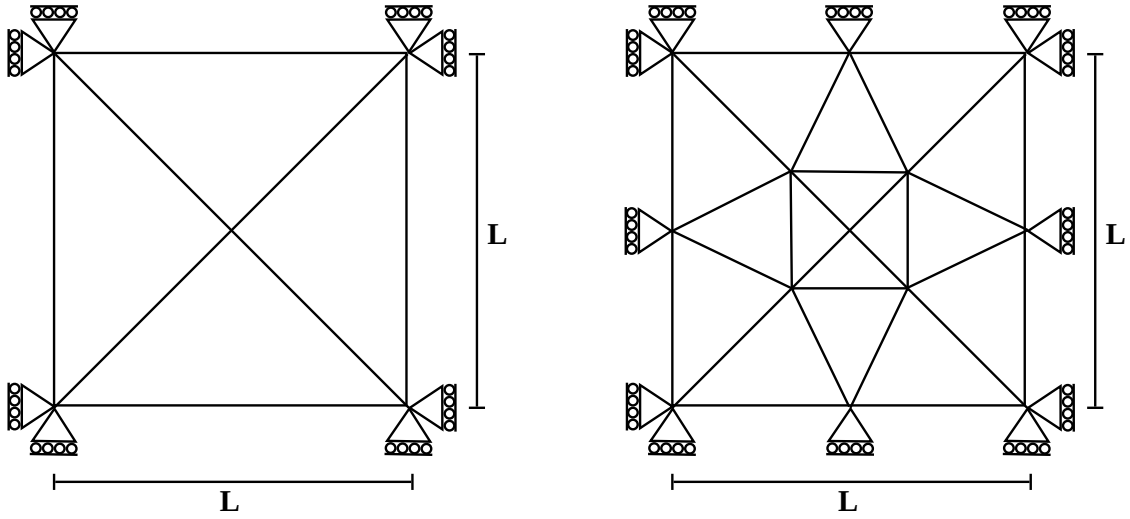

(a) Mesh 1x1. (b) Mesh 3x3.

Figure C.17: The geometry with different meshes used in the academic example.

$$\frac{\partial \sigma_x}{\partial x} + \frac{\partial \sigma_{xy}}{\partial y} + f_x = 0 \tag{C.4}$$

$$\frac{\partial \sigma_y}{\partial y} + \frac{\partial \sigma_{xy}}{\partial x} + f_y = 0 \tag{C.5}$$

The load vectors are applied to the model, and the displacements are calculated. The strain energy can then be found by the global displacement vector [SysU] and the global stiffness matrix [SysK]:

$$E_{numeric} = [\text{SysU}]' \, [\text{SysK}] \, [\text{SysU}] \tag{C.6}$$

The strain energy is computed for the LST element, the EXT element and the FEXT element. The results are shown in Table C.7.

Table C.7: Strain energy $E_{numeric}$ in the model.

Mesh	LST	EXT 12x12	FEXT 20x20
1X1	2.0010	4.9636	3.8932
3X3	2.6786	2.0386	2.2937
7X7	2.7675	2.6128	2.6170
15X15	2.7749	2.7397	2.7366
E_{exact}	2.7755	2.7755	2.7755

The convergence rates are illustrated in a log-log scale in Figure C.18. In the x-direction the relation between the length of the geometry and the characteristic element length is dipicted, expressed by $h = \frac{1}{\sqrt{N_{els}}}$. In the y-direction the difference between the exact and numerical strain energy is depicted.

The discretization error, and thereby the convergence rate, of strain energy is [11, Section 9.6]:

$$O(h^{2(p+1-m)}) \tag{C.7}$$

where

O is the order of the elements used,
h is the characteristic length of an element,
p is the degree of the highest complete polynomial, and
2m is the order of the highest derivative in the governing differential equation.

This means that the slope for the LST element should be $O(h^{(2(2+1-1))}) = O(h^4)$, and the slope for the EXT and FEXT elements should be $O(h^{(2(3+1-1))}) = O(h^6)$.

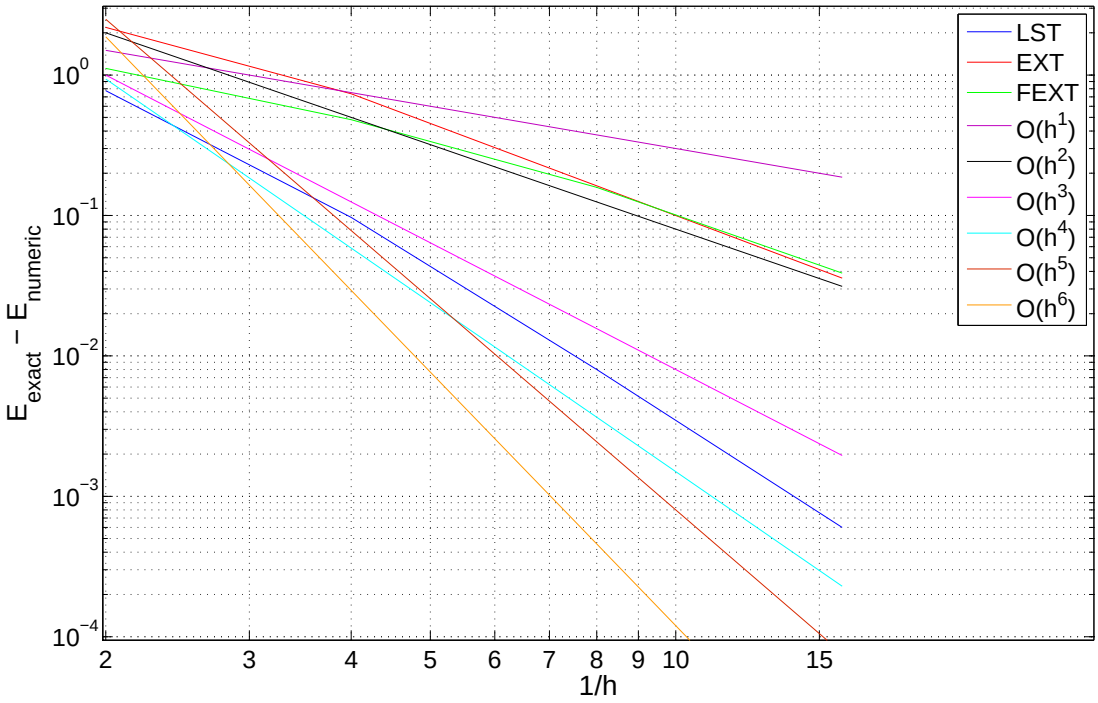

Figure C.18: Convergence of strain energy.

As seen in Figure C.18, the convergence rate of the LST element is as expected $O(h^4)$. However, the convergence rate of the EXT and FEXT element is $O(h^2)$ wich is remarkably lower than it should be. It is also much lower than the convergence rate of the LST element, and this corresponds well with the previous example.

C.6 Conclusion on linear tests

Previous tests of the extended element have been only partially successful. The patch tests verified that the extended element provides a stable solution, and is able to converge towards an exact soluion. However, passing the patch tests is not a guarantee that the element will perform well in other applications such as accuracy and convergence rate.

The tests concerning Cook's membrane showed that the convergence rate of both displacements and stresses of the extended element is poor compared to the LST element. The best known results from [18] and [4] was used for comparison of accuracy. However, it can be discussed whether the best known results are outdated, since these were proposed more than twenty years ago.

The tests concering strain energy showed likewise that the convergence of the extended element is poor compared to the standard element.

These tests indicates that the extended element is too flexible to provide accurate results in a linear analysis. As shown in Section 1.1, the conventional elements overestimated the factor of safety and thereby the bearing capacity of the soil. This suggests that the flexibility of the element can be an advantage in nonlinear geotechnical analysis, because the element does not underestimate the displacements in soil materials.

The conclusion is that the extended element is not well suited for linear analysis, however, this does not mean that the exended element is not well suited for nonlinear analysis. Therefore in the following the implementation of the EXT element in Matlab is extended to nonlinear analysis.

D Introducing a hardening parameter - Figures

In this appendix, different figures referred to in Section 6.3 is seen.

D.1 Mesh

The two mesh sizes not shown in Section 6.3 can be seen on Figure D.1 and Figure D.2.

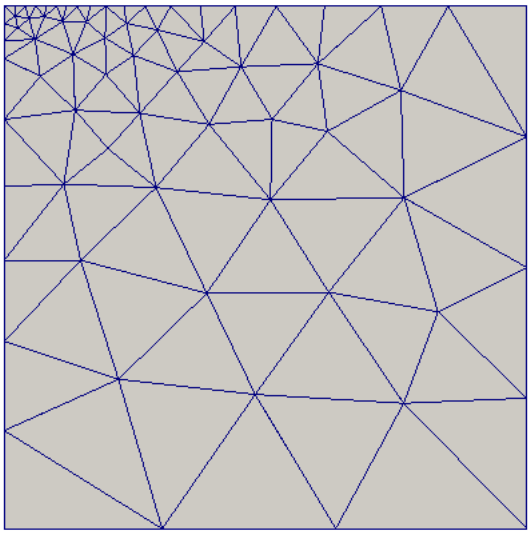

Figure D.1

Figure D.2

D.2 Bearing capacity

Here the bearing capacity for the strip footing is seen. Figure D.3 corresponds to the medium coarse mesh shown in Figure D.1, and Figure D.4 corresponds to the finest mesh

shown in Figure D.2.

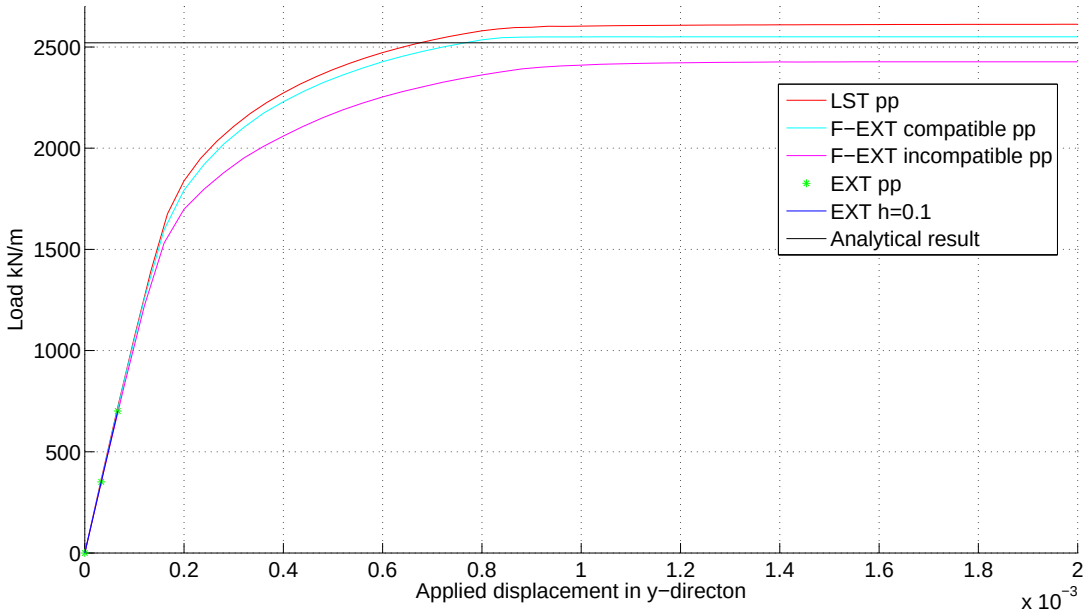

Figure D.3: Settlement of a strip footing with pp indicating perfect plasticity and h=0.1 indicating a hardening parameter.

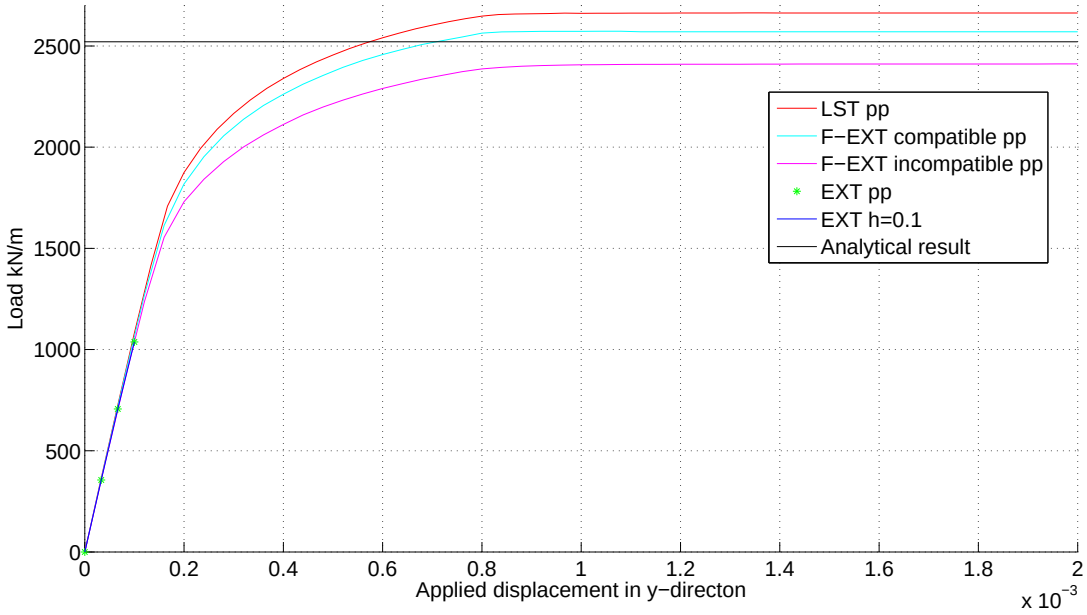

Figure D.4: Settlement of a strip footing with pp indicating perfect plasticity and h=0.1 indicating a hardening parameter.